FAKULTÄT FÜR VERFAHRENS-
UND SYSTEMTECHNIK

Application of the Lattice Boltzmann Method to Hemodynamic Simulations in Intracranial Aneurysms

Dissertation
for the award of the degree of

Doktoringenieur

(Dr.-Ing.)

by M.Sc. Feng Huang

born March, 14th 1989 in Anhui, China

accepted by the Faculty of Process and Systems Engineering
of the Otto-von-Guericke-University of Magdeburg

Reviewers:

Prof. Dr.-Ing. Gábor Janiga

Prof. Dr.-Ing. Dominique Thévenin

Prof. Dr.-Ing. Bernhard Preim

Prof. György Paál

Submitted on: 18.12.2023

Graduation Colloquium on: 02.05.2024

Declaration

I hereby declare that I prepared the submitted work without inadmissible assistance and without the use of any aids other than those indicated. Facts or ideas taken from other sources, either directly or indirectly have been marked as such.

In particular, I did not use the services of a commercial graduation consultation. Furthermore, I have not made payments to third parties either directly or indirectly for any work connected with the content of the submitted dissertation.

This work has so far not been submitted either in Germany or abroad in the same or similar form as a dissertation and has also not yet been published as a whole.

Magdeburg,
18.12.2023

Abstract

In the past two decades, the lattice Boltzmann method (LBM) has emerged as an efficient alternative to classical numerical techniques for simulating physiological flows, owing to the advancement of modern supercomputers. This progress has opened up new avenues for improving our understanding of the pathology and pathophysiology of various medical conditions within the human body. This thesis focuses on investigating various aspects of hemodynamics within intracranial aneurysms using our in-house numerical solver, called ALBORZ.

Firstly, we address the challenge of complex geometry in patient-specific aneurysms by developing a curved boundary condition. This innovation significantly enhances the accuracy of LBM simulations, allowing for the capture of intricate geometries with a lower computational domain resolution.

The second focal point of our research is the non-Newtonian flow model. We propose a robust modified central Hermite polynomial-based multiple relaxation time lattice Boltzmann model, which offers independent control over the relaxation of acoustic modes for non-Newtonian fluids. Our primary application is in modeling blood flow within intracranial aneurysms. This model employs a robust collision operator and enables implicit computation of non-linear stress, providing flexibility in terms of time step and grid size. Validation is performed through well-documented configurations, demonstrating second-order convergence. The results challenge the assumption of high shear rates within aneurysm sacs.

The final emphasis of this thesis is unsteady flow within patient-specific aneurysms, with a focus on flow fluctuations. Flow instability has recently gained recognition as a promising hemodynamic metric for assessing the rupture risk of intracranial aneurysms. Our study investigates flow fluctuations using both Newtonian and non-Newtonian fluid models in patient-specific intracranial aneurysms. High-resolution lattice Boltzmann simulations are employed to quantify flow instabilities through power spectral density, proper orthogonal decomposition, spectral entropy, and fluctuating kinetic energy of velocity fluctuations. Furthermore, we compare these hemodynamic parameters between ruptured and unruptured aneurysms. Our findings reveal that pulsatile inflow through the neck of ruptured aneurysms is subject to hydrodynamic instability, resulting in high-frequency fluctuations around the rupture location throughout the cardiac cycle. In other regions, flow instability is primarily observed during the deceleration phase, gradually diminishing as the flow returns to a laminar pulsatile state during diastole. Importantly, for unruptured aneurysms, the difference between Newtonian and non-Newtonian outcomes is minimal. However, in the context of ruptured cases, adopting the non-Newtonian model significantly increases the magnitude of fluctuations within the aneurysm sac.

This thesis contributes to the understanding of hemodynamics in intracranial aneurysms, providing insights into the role of non-Newtonian behavior and flow fluctuations in the rupture risk assessment of these critical medical conditions.

Keywords: Lattice Boltzmann method, Intracranial aneurysms, Computational

fluids dynamics, Non-Newtonian flows, Flow instability

Zusammenfassung

In den letzten zwei Jahrzehnten hat sich die Lattice-Boltzmann-Methode (LBM) als effiziente Alternative zu klassischen numerischen Techniken für die Simulation physiologischer Strömungen entwickelt, dies ist auf den Fortschritt moderner Supercomputer zurückzuführen. Dieser Fortschritt hat neue Möglichkeiten eröffnet, unser Verständnis für die Pathologie und Pathophysiologie verschiedener medizinischer Zustände im menschlichen Körper zu verbessern. Diese Dissertation konzentriert sich darauf, verschiedene Aspekte der Hämodynamik innerhalb intrakranieller Aneurysmen mithilfe unseres hausinternen numerischen Lösers ALBORZ zu untersuchen.

Zunächst gehen wir auf die Herausforderung der komplexen Geometrie in patientenspezifischen Aneurysmen ein, indem wir eine gekrümmte Randbedingung entwickeln. Diese Innovation verbessert signifikant die Genauigkeit von LBM-Simulationen und ermöglicht die Erfassung komplexer Geometrien mit einer geringeren Auflösung des Berechnungsbereichs.

Der zweite Schwerpunkt unserer Forschung liegt auf dem nicht-newtonschen Strömungsmodell. Wir schlagen ein robustes, auf zentralen Hermite-Polynomen basierendes LBM mit mehreren Relaxationszeiten vor, das eine unabhängige Steuerung der Relaxation akustischer Moden für nicht-newtonsche Fluide ermöglicht. Unsere Hauptanwendung liegt in der Modellierung des Blutflusses innerhalb intrakranieller Aneurysmen. Dieses Modell verwendet einen robusten Kollisionsoperator und ermöglicht die implizite Berechnung von nichtlinearem Stress, was Flexibilität in Bezug auf Zeitschritt und Gittergröße bietet. Die Validierung erfolgt durch gut dokumentierte Konfigurationen, die eine Konvergenz zweiter Ordnung zeigen. Die Ergebnisse stellen die Annahme hoher Schergeschwindigkeiten innerhalb von Aneurysma-Säcken in Frage.

Der letzte Schwerpunkt dieser Arbeit liegt auf der instationären Strömung innerhalb patientenspezifischer Aneurysmen mit Fokus auf Strömungsschwankungen. Strömungsinstabilität wird in letzter Zeit als vielversprechende hämodynamische Metrik für die Bewertung des Rupturrisikos intrakranieller Aneurysmen anerkannt. Unsere Studie untersucht Strömungsschwankungen unter Verwendung sowohl newtonscher als auch nicht-newtonscher Strömungsmodelle in patientenspezifischen intrakraniellen Aneurysmen. Hochauflösende Lattice-Boltzmann-Simulationen werden verwendet, um Strömungsinstabilitäten durch Leistungsdichtespektrum, orthogonale Zerlegung, spektrale Entropie und fluktuierende kinetische Energie von Geschwindigkeitsfluktuationen zu quantifizieren. Darüber hinaus vergleichen wir diese hämodynamischen Parameter zwischen rupturierten und nicht-rupturierten Aneurysmen. Unsere Ergebnisse zeigen, dass der pulsierende Zufluss durch den Hals von rupturierten Aneurysmen einer hydrodynamischen Instabilität unterliegt, die zu hochfrequenten Schwankungen um die Rupturstelle während des gesamten Herzzyklus führt. An anderen Stellen wird die Strömungsinstabilität hauptsächlich während der Verzögerungsphase beobachtet, die sich allmählich vermindert, und die Strömung kehrt während der Diastole zu ihrem ursprünglichen laminaren pulsierenden Zustand zurück. Insbesondere für nicht-rupturierte Aneurysmen ist der Unterschied zwischen newtonschen und nicht-newtonschen Ergebnissen minimal. In rupturierten Fällen führt jedoch die Anwendung des nicht-newtons-

chen Modells zu einer erheblichen Zunahme der Schwankungen innerhalb des Aneurysma-Sacks.

Diese Dissertation trägt zum Verständnis der Hämodynamik in intrakraniellen Aneurysmen bei und bietet Einblicke in die Rolle des nicht-newtonschen Verhaltens und der Strömungsschwankungen bei der Bewertung des Rupturrisikos dieser kritischen medizinischen Zustände.

Schlüsselwörter: Lattice-Boltzmann-Methode, Intrakranielle Aneurysmen, Numerische Strömungsdynamik, Nicht-newtonsche Strömungen, Strömungsinstabilität

Contents

List of Figures

Nomenclature

Abbreviations

BC	Boundary Condition
BGK	Bhatnagar-Gross-Krook
CFD	Computational Fluid Dynamics
CFL	Courant-Friedrichs-Lewy
CTA	Computed Tomographic Angiography
EDF	Equilibrium Distribution Function
IA	Intracranial Aneurysm
LBE	Lattice Boltzmann Equation
LBM	Lattice Boltzmann Method
LGA	Lattice Gas Automata
MRA	Magnetic Resonance Angiography
MRT	Multiple Relaxation Time
NSE	Navier-Stokes Equations
PDE	Partial Differential Equation
SRT	Single Relaxation Time

Fluid properties

μ	Fluid dynamic viscosity	$\mathrm{kg}/(\mathrm{m} \cdot \mathrm{s})$

ν	Fluid kinematic viscosity	m^2/s
Macroscopic variables		
ρ	Fluid density	kg/m^3
Mesoscopic variables		
$\boldsymbol{\tau}$	Flow field solver relaxation time	s
$\boldsymbol{\xi}$	Particle velocity vector	m/s
$\boldsymbol{c_\alpha}$	Discrete particle velocity vector	-
$\boldsymbol{f_\alpha}$	Particle discrete distribution function	-
$\boldsymbol{f_\alpha^{(eq)}}$	Particle discrete equilibrium distribution function	-
$\boldsymbol{M}$	Central Hermite moments transform matrix	-
$\boldsymbol{S}$	Relaxation coefficients matrix in MRT collision model	-
Miscellaneous parameters		
δ_t	Time-step size	s
δ_x	Grid size	m
Non-dimensional numbers		
Re	Reynolds number	

Chapter 1

Introduction

Contents

1.1 Motivations and Objectives

Cardiovascular disease remains a leading cause of mortality in developed countries [10]. Comprehending the behavior of blood within the vascular system, specifically its hemodynamics, is of paramount importance for gaining insights into the origin, advancement, diagnosis, and management of vascular disorders. This knowledge is instrumental in addressing conditions like aneurysms, arteriovenous malformations, and atherosclerosis.

The core concept of this thesis revolves around the increasing interest in modeling hemodynamics within intracranial aneurysms using various numerical tools. Traditional interventional treatments, including procedures like clipping, coiling, and the use of flow diverters, can be less justified due to their significant medical and financial costs, as well as the risk of aneurysm rupture and related complications during surgery. Instead, hemodynamic analysis plays a pivotal role in assessing the rupture risk of aneurysms. There is mounting evidence suggesting correlations between hemodynamic features and the likelihood of rupture. Consequently, it becomes imperative to conduct a thorough benefit-risk assessment for each patient before proceeding with any therapeutic interventions.

Furthermore, given the high computational efficiency, parallel nature, suitability for large-scale simulations, and ease of handling complex geometric structures, the lattice Boltzmann method (LBM) presents a compelling approach for investigating flow phenomena in patient-specific aneurysms. Hence, this thesis is primarily driven by the aspiration to investigate the possible presence of transitional flows within intracranial aneurysms. To accomplish this, it leverages our in-house numerical tool that incorporates a parallel fluid solver and high-performance computing, with the intent of enhancing the comprehension of hemodynamics in intracranial aneurysms. The ultimate objective of this research is to facilitate clinical practice by offering an efficient and user-friendly toolkit for real-time decision support.

1.2 Thesis outline

This thesis makes some contributions to the medical community by simulating the hemodynamics in intracranial aneurysms using the lattice Boltzmann method (LBM). All cases are carried out with our in-house LBM solver (ALBORZ). The thesis is organized in the following structure:

Chapter 2 (Lattice Boltzmann Method) serves as a short introduction to its theoretical method. It covers various aspects, starting with the historical background, tracing the evolution of LBM. It delves into the governing equations, specifically the discretized lattice Boltzmann equation and collision models, which form the core of the method. Additionally, this section explores the extension of LBM to non-Newtonian viscosity models, highlighting its versatility in simulating complex real blood shear-thinning behaviors. Furthermore, the section reviews the various boundary conditions employed in this study. One of the most important boundary conditions is the time-dependent boundary condition at inlet which is essential for capturing the dynamic nature of blood flow. The other one is to address

the intricate geometries of patient-specific aneurysms by presenting the curved boundary condition as an effective modeling approach.

Chapter 3 (Validation Studies) is dedicated to a series of benchmarking studies that validate the accuracy and reliability of the computational simulations employed in the thesis. These benchmarking exercises serve as essential pillars supporting the credibility of our numerical methods. Firstly, our simulation results are meticulously compared with in-vitro experimental results. Secondly, we tackle the FDA nozzle benchmark, which encompasses a wide range of flow regimes, from laminar to transitional and mildly turbulent flows. Successfully replicating this benchmark demonstrates the versatility and robustness of the numerical solver across different flow conditions. Finally, we focus on validating the non-Newtonian viscosity model employed in our simulations. This validation is achieved through comparisons with classical flow scenarios: Hagen-Poiseuille flow, and lid-driven cavity flow. These canonical flows provide an excellent foundation for assessing the model's ability to capture the shear-thinning behavior of non-Newtonian blood. Collectively, these benchmarking studies not only validate our numerical solver but also ensure that the numerical results obtained through this thesis are reliable and representative of real-world fluid dynamics.

Chapter 4 (Non-Newtonian Effect) delves into the significance of non-Newtonian effects in the context of intracranial aneurysms. The study encompasses three distinct aneurysm cases: one idealized and two patient-specific. Four different non-Newtonian viscosity models are involved. By including these variations, we ensure a thorough exploration of the topic.

Chapter 5 (Flow Instability) is dedicated to establishing the connection between aneurysm rupture and flow fluctuations within the sac. The impact of various factors, including resolution, aneurysm type, non-Newtonian models, and Reynolds number, on the likelihood of rupture will be thoroughly examined in this section.

Chapter 6 (Conclusions and Outlook) serves as the conclusion of this thesis, offering a comprehensive summary and discussion of the research topics and findings presented throughout. Additionally, it outlines potential future avenues of research, with a particular focus on simulating thrombosis within intracranial aneurysms.

1.3 Hemodynamics

1.3.1 Blood circulation

The exploration of blood flow within the human circulatory system, often referred to as the cardiovascular system, has become a focal point of interest in the fields of bioengineering and medicine. This heightened focus is primarily attributed to the fact that a significant proportion of human fatalities are directly linked to issues related to blood supply, encompassing blood vessels, arteries, tissues, and the various phases of the cardiac cycle. Conditions such as heart attacks, strokes, and ischemic chest pain, among others, can be traced back to diseases affecting the circulatory system. Understanding and analyzing blood flow dynamics in the cardiovascular system is pivotal in preventing and managing these life-threatening

conditions.

In the cardiovascular system, blood is a complex mixture of a variety of cells and proteins by which wastes and nutrients are transported. Typically, red blood cells make up approximately 40% of blood by volume, which increases the viscosity of blood and affects its behavior as small semisolid particles. Normally, blood is about four times more viscous than water but its viscosity is not constant at all flow rates. In the microcirculatory system, blood exhibits non-Newtonian behavior, which is more evident at very low shear rates in small branches and capillaries as red blood cells clump together into larger particles. However, blood behaves like a Newtonian fluid in larger arteries with a diameter greater than 1 mm and the viscosity can be considered constant there [11].

On the other hand, blood flow and pressure in the arterial system are unsteady due to the cyclic nature of the heart, which creates pulsatile conditions between the aorta and the veins. The heart pumps blood out during systole and rests during diastole, resulting in alternating cycles of blood ejection and filling. As a result, pressure and flow exhibit characteristic pulsatile shapes that vary in different parts of the arterial system. The pulsatile period of blood is close to 1 s under normal physical conditions.

These intricate characteristics of blood, including non-Newtonian behavior and pulsatile flow, significantly increase the complexities of studying hemodynamics within the cardiovascular system.

1.3.2 Intracranial aneurysms

A common life-threatening disease, coming with intracranial aneurysms (IAs), is constituted by local malformations of the cerebral vasculature and often arise at a branch site on a parent artery. It occurs with an estimated prevalence of approximately 3% in the western population [12]. According to the brain aneurysm foundation, a cerebral aneurysm ruptures every 18 minutes in the United States, and 30,000 people suffer from a rupture per year. It is known that aneurysms can grow and either develop into a stable state, or rupture if the hemodynamic forces exceed the vascular resistance. A Subarachnoid hemorrhage (SAH) appears as a region of increased density in the subarachnoid spaces of the basal and Sylvian cisterns [13], which is one of the most fatal consequences. Although studies [14, 15] reported that a SAH occurs with a probability of only around 0.013% in the world population, over 85% of these cases are caused by IA rupture and the fatality rates are very high, between 32% and 67% [16]. There are three main types of intracranial aneurysms: saccular, fusiform, and micotic type.

1. **Saccular type:** It comprises 90% of intracranial aneurysms and it develops as a thin-walled sac protruding from the cerebral arteries of the circle of Willis or its major branches. Figure 1.1 illustrates the scheme of the circle of Willis. Approximately 85% of saccular aneurysms are found protruding from the arteries of the circle of Willis. The anterior communicating artery (ACoA) is the most frequent site (30-35%), followed by the internal carotid artery (ICA, 30%) and the middle cerebral artery (MCA, 22%). Aneurysms of the posterior circulation take up approximately 8-10% and the basilar

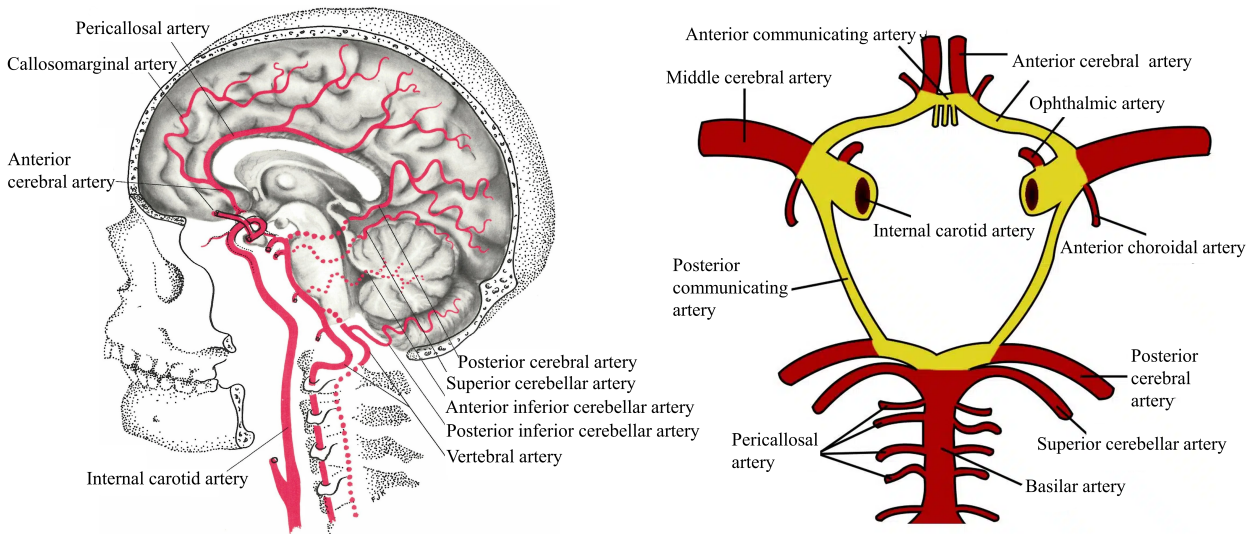

Figure 1.1: Schematics of blood supply to the brain (Left) [1]. The frontal view shows the primary arteries in the brain. The top view shows the structure of the Circle of Willis (Right, from `https://teachmeanatomy.info/neuroanatomy/vessels/arterial-supply/`).

tip is the most common location of origin. Saccular aneurysms can be classified into three types based on their size: small (<10 mm), large (10-25 mm), giant (> 25 mm). They can also be further classified based on neck width: small neck (<4 mm) and large neck (>4 mm). These anatomical features are important for deciding the therapeutic approach and intraoperative risk [17].

2. **Fusiform type:** It is an abnormal dilation of arteries caused by atherosclerosis and are typically found in elder patients. They can result in ischemia or mass effect, but rupture is uncommon. Dissecting aneurysms, on the other hand, are rare and have a poor natural prognosis in patients presenting with SAH due to a high rebleeding rate [18].

3. **Mycotic type:** It is extremely rare and develops from infections in the arterial wall, often originating from bacterial endocarditis. These aneurysms primarily affect the distal branches of cerebral arteries and appear as fusiform and eccentric dilations without the neck typically seen in saccular aneurysms [19].

Ninety percent of aneurysms become symptomatic due to rupture, leading to SAH, with the highest incidence occurring between the ages of 40 and 60. The CT angiography (CTA) is considered the gold standard for diagnosing SAH. The original CT pattern can provide valuable information about the source of the ruptured aneurysms in most cases. Focal blood layers are typically present near the ruptured aneurysm and can assist in determining which vessel to investigate using arteriography. Around 15-20% of patients with spontaneous SAH exhibit normal findings on intra-arterial digital subtraction angiography (IADSA), indicating an unidentified source of bleeding.

1.3.3 Medical imaging techniques

Imaging is indeed essential for the diagnosis, surveillance, treatment, and post-treatment follow-up of intracranial aneurysms. IAs are increasingly being detected due to the widespread application of advanced imaging techniques. On the other hand, accurate numerical simulations of intracranial aneurysms heavily rely on precise imaging data for constructing patient-specific models and boundary conditions. In this context, we will provide an overview of the common imaging techniques used to detect aneurysms:

- **Computed tomography angiography-CTA:** With the introduction of spiral and multi-slice CTA, examination times have been substantially reduced. As a result, three-dimensional CTA has been suggested as a supplementary technique to non-contrast CT for investigating SAH. To visualize the intracranial arteries adequately, the 3D-CTA examination should encompass the region from the first vertebral body to the vertex. This wide coverage is essential to capture the relevant anatomical structures and pathology associated with SAH.

  Achieving good quality CTA not only relies on appropriate acquisition parameters but also on post-processing techniques, which should be performed on a fast workstation capable of real-time 3D volume rendering. There are several methods available for analyzing the CTA volume [20]. First and foremost, it is essential to examine the source images to identify the aneurysms and partial thrombosis before proceeding with 3D processing. The average sensitivity of CTA for detecting IAs has been reported to be around 90%. However, the sensitivity decreases to 61% for aneurysms ≤ 3 mm while the detection rate increases to 96% for larger diameter aneurysms [21]. In some centers, CTA has almost entirely replaced IADSA in patients with SAH [22, 23].

- **Magnetic resonance angiography-MRA:** While Magnetic resonance angiography (MRA) has shown promising results in detecting aneurysms in acute SAH [24], its practicality is still often limited in severely affected patients. MRA has drawbacks such as long examination times, lower spatial resolution compared to digital subtraction angiography (DSA), high cost, susceptibility to motion artifacts, and difficulties in visualizing vessels with low-flow conditions. Intracranial MRA is preferred as a screening modality for specific high-risk groups rather than the general population. These high-risk groups include individuals with connective tissue disorders such as fibromuscular dysplasia, Ehlers-Danlos type IV and neurofibromatosis type 1. MRA is also recommended for families with two or more first-degree relatives who have experienced SAH [25]. However, MRA offers the advantage of high sensitivity to flow phenomena, enabling visualization of cerebral vessels without the need for contrast medium administration.

  Currently, three main MRA techniques are commonly employed: time-of-flight (TOF), phase-contrast (PC) and gadolinium-enhanced MRA. These techniques involve the acquisition of flow-sensitive images of intracranial vessels in either 2D or 3D, with background suppression, and the generation of angiographic projections to visualize the intracranial vasculature. 3D acquisitions are preferred for imaging the intracranial ar-

teries due to lower gradient amplifier demands, enabling shorter echo times and higher signal-to-noise ratios, which can contribute to improved spatial resolution. As phase-contrast MRA is characterized by longer acquisition times and lower spatial resolution, 3D TOF MRA has largely replaced phase-contrast MRA in screening examinations. Spatial resolution plays a crucial role in accurately visualizing smaller aneurysms and reducing the impact of turbulent flow in larger aneurysms. However, compared to CTA, MRA has the disadvantage of limited coverage of the intracranial vasculature. The development of MRA examination strategies is indeed challenging due to the need to balance image resolution, anatomical coverage and acquisition time, which involves trade-offs among these factors. Gadolinium-enhanced MRA has recently emerged as a potential method for assessing larger aneurysms that exhibit turbulent flow. Traditional techniques often underestimate the size of such aneurysms [26]. Contrast-phase MRA is particularly appealing as it offers the possibility of conducting MR examinations with both extensive coverage volume and high spatial resolution. However, the widespread adoption of contrast-enhanced MRA has been limited so far. This is primarily due to the challenge of differentiating contrast-enhanced proximal arteries from the enhanced venous structures near the cavernous segment of the internal carotid artery.

In summary, medical imaging, particularly through CTA and MRA, plays a pivotal role in the comprehensive management of intracranial aneurysms. CTA and MRA stand out as noninvasive and cost-effective imaging techniques. CTA, in particular, offers the advantage of lower radiation exposure compared to conventional diagnostic angiography, while MRA eliminates ionizing radiation altogether. Future research should aim to enhance imaging methodologies while considering healthcare efficiency and patient care quality.

Chapter 2

The lattice Boltzmann method

Contents

2.1 Overview

Fluid mechanics is a fascinating branch of physics that investigates the behavior of fluids and the forces exerted on them. In the realm of Computational Fluid Dynamics (CFD), there are typically three distinct approaches employed to simulate the transport equations of the fluids. These approaches are categorized based on the available time and length scales revlevant to the physical domain being studied.

1. **Continuum Approach (Top-Down):** This approach provides a macroscopic description of fluid behavior using partial or ordinary differential equations for the conservation of mass, momentum, and energy in the system. For instance, the well-known Navier-Stokes Equations (NSE) are often employed to describe the momentum conservation in fluid flows. These equations are further simplified to the Navier-Stokes-Poisson equation in incompressible cases. However, obtaining the analytical solutions to these differential equations is exceptionally challenging due to the intricate nature of real-world phenomena. Consequently, alternative numerical techniques such as finite element, finite difference, and finite volume methods are used to discretize the differential equations into a system of algebraic equations. These algebraic equations are then solved iteratively by employing the appropriate initial and boundary conditions.

2. **Microscopic Approach (Bottom-Up):** Compared to the macroscopic method, this approach considers fluids as a vast collection of atoms or molecules that interact through collisions and exhibit random motion. In this microscopic scale of study, the focus is on the behavior of individual particles rather than macroscopic variables. The forces between particles can be described using Newton's second law. The position of each particle is updated by solving ordinary differential equations. Statistical mechanics provides a powerful framework for connecting the microscopic and macroscopic properties of the fluid. For instance, macroscopic variable pressure is related to the frequency of collisions with the walls while the temperature is obtained from the kinetic energy of the particles. However, this method is primarily applicable to studying very small domains, typically on the sub-micrometer scale due to the enormous number of particles present in even a small fluid domain. Consequently, the analysis of large-scale systems becomes virtually impractical using this approach.

3. **Mesoscopic Approach (Hybrid):** In recent years, an alternative approach known as the LBM has emerged for simulating a wide variety of fluid flow, which bridges the gap between the continuum and microscopic approaches above mentioned by considering molecular dynamics. LBM works by solving distribution functions that represent the number density of molecules with certain discrete velocities. These distribution functions are updated, typically through an explicit quasi-linear collision-propagation process. Macroscopic variables like pressure, velocity, and velocity gradients are then computed as moments of these distribution functions. The fundamental idea behind the LBM is to construct simplified kinetic models that incorporate only the essential physics of microscopic or mesoscopic processes, ensuring that the macroscopic averaged properties adhere to the desired macroscopic equations. The LBM offers several

highly valued features such as simplicity, easy handling of complex geometries, and excellent parallelization efficiency. Due to these advantages, the LBM has experienced rapid development over the last few decades and has found extensive application in fluid dynamics simulations across various domains.

CFD is known to be a demanding field in terms of computational resources and is sensitive to the numerical scheme employed. Traditional numerical methods used in CFD are computationally heavy and rely on relatively fastidious discrete operations, especially when the geometry is complex. The LBM is an alternative numerical technique that gained increasing attention, particularly so over the last two decades. Its popularity is due to the simplicity of the involved numerical operations, their locality – ensuring excellent portability to parallel computing architectures – and the relative ease at which complex geometries can be treated [27]. These strengths combined with its ability to model mechano-biological phenomena [28, 29], make the LBM a method of choice for the bio-medical community [30, 31, 32, 33, 34, 35, 36, 37, 38].

2.2 Background

LBM originated from lattice gas automata (LGA), used to track the movement of discrete gas particles on a regular lattice in the late 1980's [39]. The collision process of those discrete particles follows specific rules. These particles meet at lattice nodes and are subsequently redistributed in a manner that guarantees the conservation of mass, momentum, and energy. In contrast, the streaming of these particles is a more straightforward and simpler process. The first LGA model, known as the HPP model, was introduced by Hardy et al. [40] and was based on a square lattice. However, this HPP model lacks sufficient symmetry and failed to yield the NSE in the macroscopic limit. To address this limitation, the FHP model was introduced [41], which incorporated hexagonal symmetry and allowed for the modeling of various two-dimensional geometries. Frisch et al. [39] later addressed the issue of three-dimensional modeling within the framework of LGA. Despite these advancements, both models had two major limitations. The first is that the Boolean nature of LGA introduced statistical noise and the other one is that Galilean invariance could not be recovered, due to its discrete nature of the lattice. Additionally, the pressure, which was determined by the equation of state, exhibited an explicit and unphysical dependence on velocity [42].

To overcome these limitations, the LBM introduced a significant change by replacing the Boolean variable of LGA with a real-valued distribution function [43, 44]. This distribution function represents the probability of finding a particle with a specific velocity at a given lattice site. By using a continuous distribution function, LBM could handle a wider range of fluid behaviors and address the limitations of LGA. On the other hand, a Maxwell-type distribution function was introduced, leading to noise suppression, Galilean invariance, and velocity-independent pressure. Furthermore, the collision operator was further simplified by using a constant relaxation parameter, resulting in the well-known single relaxation time (SRT) with the Batnagar-Gross-Krook (BGK) operator. Later, He and Luo [45] derived LBM directly from the Boltzmann equation, providing a theoretical foundation for the method.

2.3 The Boltzmann equation

A statistical description of a system can be obtained using a distribution function, denoted as $f(\boldsymbol{x}, \boldsymbol{\xi}, \boldsymbol{t})$. Here, $f(\boldsymbol{x}, \boldsymbol{\xi}, \boldsymbol{t}) d\boldsymbol{x} d\boldsymbol{\xi} dt$ represents the number of molecules positioned between $\boldsymbol{x}$ and $\boldsymbol{x} + d\boldsymbol{x}$, with velocities between $\boldsymbol{\xi}$ and $\boldsymbol{\xi} + d\boldsymbol{\xi}$. When an external force $\boldsymbol{F}$ acts on a gas molecule of unit mass, it changes the molecule's velocity from $\boldsymbol{\xi}$ to $\boldsymbol{\xi} + \boldsymbol{F dt}$ and its position from $\boldsymbol{x}$ to $\boldsymbol{x} + \boldsymbol{\xi dt}$. In the absence of collisions between the molecules, the number of molecules,$f(\boldsymbol{x}, \boldsymbol{\xi}, \boldsymbol{t})$, before the application of the external force, is equal to the number of molecules after the disturbance,$f(\boldsymbol{x} + \boldsymbol{\xi dt}, \boldsymbol{\xi} + \boldsymbol{F dt}, \boldsymbol{t} + \boldsymbol{dt})$. This implies that in the absence of collisions, the distribution function remains unchanged. Hence,

$$f\left(\boldsymbol{x} + \boldsymbol{\xi} dt, \boldsymbol{\xi} + \boldsymbol{F} dt, t + dt\right) d\boldsymbol{\xi} d\boldsymbol{x} - f\left(\boldsymbol{x}, \boldsymbol{\xi}, t\right) d\boldsymbol{\xi} d\boldsymbol{x} = 0 \tag{2.1}$$

On the other hand, when collisions occur between the molecules, the number of molecules within the infinitesimal volume $(d\boldsymbol{x})$ will be affected. The collisions lead to a redistribution of the molecules in both position and velocity space. This net difference, which represents the rate of change between the initial and final states of the distribution function, is referred to as the collision operator, denoted as $\boldsymbol{\Omega}$.

Therefore, the equation governing the evolution of the distribution function can be written as:

$$f\left(\boldsymbol{x} + \boldsymbol{\xi} dt, \boldsymbol{\xi} + \boldsymbol{F} dt, t + dt\right) d\boldsymbol{\xi} d\boldsymbol{x} - f\left(\boldsymbol{x}, \boldsymbol{\xi}, t\right) d\boldsymbol{\xi} d\boldsymbol{x} = \boldsymbol{\Omega}(f) d\boldsymbol{\xi} d\boldsymbol{x} dt \tag{2.2}$$

Dividing the above equation Eq. 2.2 by $d\boldsymbol{\xi} d\boldsymbol{x} dt$ in both sides and taking the limit as dt approaches 0, we obtain:

$$\lim_{dt \to 0} \frac{f\left(\boldsymbol{x} + \boldsymbol{\xi} dt, \boldsymbol{\xi} + \boldsymbol{F} dt, t + dt\right) - f\left(\boldsymbol{x}, \boldsymbol{\xi}, t\right)}{dt} = \frac{df\left(\boldsymbol{x}, \boldsymbol{\xi}, t\right)}{dt} = \boldsymbol{\Omega}(f) \tag{2.3}$$

We can expand the expression $f\left(\boldsymbol{x}, \boldsymbol{\xi}, t\right)$ into a total derivative form with respect to $\boldsymbol{\xi}, \boldsymbol{x}, t$, as follows:

$$\begin{aligned} \frac{df}{dt} &= \frac{\partial f}{\partial t} + \frac{\partial f}{\partial \boldsymbol{\xi}} \frac{d\boldsymbol{\xi}}{dt} + \frac{\partial f}{\partial \boldsymbol{x}} \frac{d\boldsymbol{x}}{dt} \\ &= \frac{\partial f}{\partial t} + \frac{\partial f}{\partial \boldsymbol{\xi}} \frac{\boldsymbol{F}}{m} + \frac{\partial f}{\partial \boldsymbol{x}} \boldsymbol{\xi} \end{aligned} \tag{2.4}$$

where m is the molecular mass.
Combining Eq. 2.3 and Eq. 2.4, the Boltzmann transport equation can be rewritten as,

$$\frac{\partial f}{\partial t} + \frac{\partial f}{\partial \boldsymbol{\xi}} \frac{\boldsymbol{F}}{m} + \frac{\partial f}{\partial \boldsymbol{x}} \boldsymbol{\xi} = \boldsymbol{\Omega}(f) \tag{2.5}$$

In the absence of an external force, the Boltzmann equation can be expressed as:

$$\frac{\partial f}{\partial t} + \boldsymbol{\xi} \cdot \nabla f = \boldsymbol{\Omega}(f) \tag{2.6}$$

It is essential to recognize that while the force-free Boltzmann equation can be categorized

as a hyperbolic partial differential equation, it differs significantly from classical hyperbolic PDEs in that it operates in D + D + 1 dimensions. Since the equation primarily governs the advection of the distribution function f by the particle velocity $\boldsymbol{\xi}$, the numerical schemes can be designed to handle the advection processes efficiently such as finite differences or finite volumes. Moreover, the simplicity of the source term, which only relies on the local value of f, contributes to the ease of implementation. It means that the computation of the source term does not require complicated calculations involving gradients or derivatives of f. This simplifies the numerical algorithm and makes it more computationally efficient.
The relationship between Eq. 2.6 and macroscopic quantities, such as fluid density ρ, fluid velocity $\boldsymbol{u}$ and internal energy e, can be expressed as follows

$$\rho(\boldsymbol{x}, t) = \int f d\boldsymbol{\xi} \tag{2.7a}$$

$$\rho(\boldsymbol{x}, t)\boldsymbol{u}(\boldsymbol{x}, t) = \int \boldsymbol{\xi} f d\boldsymbol{\xi} \tag{2.7b}$$

$$\rho(\boldsymbol{x}, t)e(\boldsymbol{x}, t) = \frac{1}{2}\int (\boldsymbol{\xi} - \boldsymbol{u})^2 f d\boldsymbol{\xi} \tag{2.7c}$$

Equations 2.7a, 2.7b, and 2.7c express conservation of mass, momentum, and energy, respectively.

2.3.1 The lattice Boltzmann equation

In fact, the Boltzmann equation presents a challenge in analytical solutions due to its complexity, as the distribution function $f_\alpha(\boldsymbol{x}, \boldsymbol{\xi}, t)$ depends on seven parameters: position (x, y, z), particle velocity (ξ_x, ξ_y, ξ_z) and time (t). However, an alternative approach can be pursued by solving the Boltzmann equation numerically, which can provide an indirect solution to the NSE. The numerical scheme for solving the Boltzmann equation is surprisingly simple. By discretizing the Boltzmann equation in time, physical space, and velocity space, we arrive at the lattice Boltzmann equation (LBE).

$$\boxed{f_\alpha\left(\boldsymbol{x} + \boldsymbol{c}_\alpha \delta_t, t + \delta_t\right) = f_\alpha\left(\boldsymbol{x}, t\right) + \delta_t \Omega_\alpha,} \tag{2.8}$$

where f_α denotes the probability of finding a particle with discrete velocity $\boldsymbol{c_\alpha}$ at a position $\boldsymbol{x}$ at time t, which is often referred to as the particle population, $\boldsymbol{c}_\alpha$ the corresponding particle velocities, δ_t the time-step size and Ω_α the discretized particle collision operator. The indices which run from $\alpha = 0 \ldots (N-1)$ denote the discrete velocity directions depending on the chosen stencil. More details on the stencils can be found in Appendix A.
The discrete Boltzmann equation has several advantages:

- Simplicity: The discrete Boltzmann equation breaks down the complex Boltzmann equation into a discrete form on a lattice, which simplifies the mathematical formulation, making it easier to understand.
- Handling Complex Boundaries: The LBM excels in handling complex boundaries and

geometries. The discretization of the Boltzmann equation is performed on a lattice, which can be easily adapted to incorporate complex boundaries and irregular geometries. The lattice structure naturally captures the interaction between fluid particles and boundaries, allowing for accurate simulation of flows in complex geometries such as medical flows with complex boundary conditions.

- Exact Advection: The advection term, which describes the transport of the distribution function f_α, is handled naturally and accurately through the streaming step in the lattice Boltzmann equation without the need for complicated iterative numerical schemes or additional approximation errors. This feature contributes to the accuracy and efficiency of the LBM.

Similar to the distribution function discussed above, the macroscopic variables such as density (ρ), momentum ($\rho\boldsymbol{u}$) at a given position $\boldsymbol{x}$ and time t can be obtained by weighted sums, known as moments, of the discrete velocity distribution function f_α.

$$\rho(\boldsymbol{x},t) = \sum f_\alpha \tag{2.9a}$$

$$\rho(\boldsymbol{x},t)\boldsymbol{u}(\boldsymbol{x},t) = \sum \boldsymbol{c_\alpha} f_\alpha \tag{2.9b}$$

2.3.2 Approximations to the collision term

2.3.2.1 Single relaxation time model

One of the pioneering approximations for modeling the collision term in the Boltzmann equation was introduced by Bhatnagar, Gross, and Krook in [46]. This approach utilizes a linear relaxation operator to approximate the effects of collisions, aiming at bringing the system closer to an equilibrium state. This BGK approximation is considered one of the oldest, simplest, and most efficient methods for simulating fluid flow using the LBM.

$$\Omega_\alpha = \frac{1}{\tau}\left(f_\alpha^{(eq)} - f_\alpha\right), \tag{2.10}$$

where τ is the relaxation time. $f_\alpha^{(eq)}$ is the equilibrium distribution function (EDF). The EDF used in LBM solvers is typically approximated as a truncated expansion (using a Taylor-McLaurin expansion in the limit of vanishing Mach numbers [45] or a Hermite expansion [47]) to resemble the Maxwell-Boltzmann distribution. It is important to note that the specific form of this approximation may depend on the dimensionality of the lattice, and in the case of a 2D lattice, the equilibrium distribution function closely matches the Maxwell-Boltzmann distribution. Therefore, it can be written as [48]:

$$f_\alpha^{(eq)} = w_\alpha \sum_{n=0}^{N} \frac{1}{n! c_s^{2n}} \boldsymbol{a}_n^{(eq)} : \boldsymbol{\mathcal{H}}_{\alpha,n}, \tag{2.11}$$

where w_α are weights associated to each discrete population, c_s is the non-dimensional sound speed at the reference temperature tied to the time-step and grid sizes, $\boldsymbol{\mathcal{H}}_{\alpha,n}$ the Hermite polynomial of order n and $\boldsymbol{a}_n^{(eq)}$ the Hermite coefficient of the corresponding order.

Shortcomings The form of the LBM most commonly used in medical applications, i.e. with the SRT collision operator and a second-order EDF, is subject to a number of well-documented shortcomings. It can be readily shown through a multi-scale perturbation analysis, that at the macroscopic scale, the viscous stress tensor recovered by the second-order EDF admits deviations from the target Newtonian stress scaling as $\mathcal{O}(\mathrm{Ma}^3)$ [49]. In the LBM literature this deviation is usually referred to as the Galilean invariance problem (rightly so as it ties the effective kinematic viscosity to local velocity) of the stress tensor. It can readily be shown that the Galilean invariance of the viscous stress tensor can be restored by extending the Hermite expansion of the EDF to higher orders, specifically for the off-diagonal components, reaching at least order three. For the bulk viscosity, however, given the bias between the first and third-order moments introduced by the limited number of discrete velocities, one must introduce an additional correction term. The bulk viscosity not being of much interest nor relevance in the near-incompressible regime, it will not be discussed further. Detailed numerical and theoretical proofs can be found in [50, 51, 52, 53, 54].

One of the major advantages of the LBM is the way boundary conditions can be implemented. The bounce-back rule is one of the most popular approaches to enforce wall, velocity and pressure boundary conditions. However, it has been shown that when used with the SRT operator it is subject to numerical artifacts such as the (non-dimensional) viscosity-dependence of the solid wall position [55]. This shortcoming can be readily proven through asymptotic analysis of the corresponding system of discrete equations or simple permeability studies of flow in porous media [49, 56]. The seminal work of I. Ginzburg and subsequent development of a collision operator with a wall position independent of the relaxation coefficient led to the two relaxation time (TRT) operator [57]. The so-called generalized collision operator first proposed in [44, 58] was later parametrized to fix its shortcomings [55]. It has been shown that in order to control the wall position independently from the viscosity, at least two different relaxation coefficients are needed (one for odd, one for even moments).

Last but not least, it is common knowledge that the classical SRT model is very sensitive to the Fourier number defined as $\mathrm{Fo} = \nu\delta_t/\delta_x^2$. It is practically unusable for $\mathrm{Fo} < 0.005$ as shown by [48, 53, 59]. Extension of the operation range of the LBM has been the topic of a wide number of articles over the past decades. Continuous effort has been dedicated to developing more advanced collision operators resulting in a plethora of models such as the multiple relaxation time (MRT) models based on either raw [60] or central moments [61], regularized models [62], entropic operators [63, 64, 65], each of which have been shown to lift this restriction to different extents.

Stability and accuracy While the BGK model represents the simplest form of a collision operator, it also faces challenges related to accuracy and stability under certain conditions. For large Reynolds number (Re) flow, stability issues can arise when the viscosity is signifi-

cantly reduced (τ close to 1/2) or the flow velocity is too large ($u \not\ll c_s$). By decreasing the grid size, the spatial resolution of the simulation is enhanced, allowing for mitigating stability problems. However, it is important to note that increasing grid resolution also leads to increased computational expenses. Therefore, a trade-off between stability and computational cost needs to be considered when deciding to decrease the grid size in such cases.

The accuracy of the numerical simulations using the BGK collision model depends on the choice of relaxation time τ. For instance, when employing the standard bounce-back algorithm for wall boundaries, the wall location is influenced by the value of τ. This becomes particularly problematic for simulations in complex aneurysm geometries. The reason is that the second-order Hermite series expansion is insufficient to ensure Galilean invariance, resulting in an error term $O(u^3)$ in the macroscopic dynamics.

To address these limitations, the improvement of accuracy and stability in the LBM can be achieved by revising the collision step. Two such collision operators have been proposed(MRT and TRT), which provide greater degrees of freedom in controlling the relaxation process while there is only one relaxation rate in BGK collision operator.

2.3.2.2 Multiple relaxation time model

Compared to the BGK collision operator, the MRT collision operator is a generalization of the BGK model and its formulation allows to relax the distribution function in a space of linearly independent base functions, typically moments of the distribution function. Since the classical BGK collision operator with one relaxation coefficient has stability issues for vanishing non-dimensional viscosities, the MRT model is proposed. The fundamental steps of the MRT collision operator are presented below:

- Transform populations to moment space.
- Relax the moments toward equilibrium.
- Transform moments back to population space.

Raw moment The raw MRT emerged and gained prominence in the early 2000s [60, 66]. The fundamental concept behind this approach is a mapping from the population in phase space to moment space via a transformation matrix. This distinctive approach allows for the independent manipulation of individual relaxation rates for linearly independent moments. The introduction of additional degrees of freedom in this method proves advantageous from both a physical and numerical standpoint [67]. In this framework, the BGK operator is expressed as:

$$\Omega_\alpha = \boldsymbol{\mathcal{M}}^{-1}\boldsymbol{S}\boldsymbol{\mathcal{M}}\left(\boldsymbol{f}_{\boldsymbol{\alpha}}^{(eq)} - \boldsymbol{f}_{\boldsymbol{\alpha}}\right), \tag{2.12}$$

where $\boldsymbol{\mathcal{M}}$ is the moments transform matrix, and $\boldsymbol{S}$ represents the relaxation coefficients matrix, which is primarily defined as a diagonal matrix with elements of $1/\tau_\alpha$, where τ_α controls the relaxation rate of the corresponding raw moment.

The moments m_α can be defined as follows:

$$m_\alpha = \sum_{\beta=0}^{q} \boldsymbol{\mathcal{M}_{\alpha,\beta} f_\beta} \tag{2.13}$$

The conversion between the distribution function and moment spaces is accomplished through the use of a transformation matrix, denoted as $\mathcal{M}$, and its inverse, denoted as $\mathcal{M}^{-1}$.

The general form can be expressed as follows, incorporating the position variables (x, y, z):

$$m_{x^i y^j z^k} = \sum_{\alpha=0}^{q} c^i_{\alpha,x} c^j_{\alpha,y} c^k_{\alpha,z} \boldsymbol{f_\alpha} \tag{2.14}$$

For the D2Q9 stencil, the following moments can be utilized:

$$\boldsymbol{m} = \begin{pmatrix} m_0 & m_x & m_y & m_{xy} & m_{x^2} - c_s^2 & m_{y^2} - c_s^2 & m_{x^2y} - c_s^2 m_y & m_{xy^2} - c_s^2 m_x & m_{x^2y^2} - c_s^2(m_{x^2} + m_{y^2}) + c_s^4 \end{pmatrix} \tag{2.15}$$

Considering terms up to the second order in the Hermite expansion, the corresponding equilibrium moments are given by:

$$\boldsymbol{m^{(eq)}} = \begin{pmatrix} \rho & \rho u_x & \rho u_y & \rho u_x u_y & \rho u_x^2 & \rho u_y^2 & 0 & 0 & 0 \end{pmatrix} \tag{2.16}$$

Central moment In the central moment method, the moments are taken in a reference frame that is moving with the macroscopic velocity. This transformation allows for better separation of the equilibrium and non-equilibrium parts of the distribution function, leading to improved accuracy and stability. It provides the additional degrees of freedom necessary to fix the wall position in the bounce-back algorithm. The enhanced spectral properties of the collision operator do not only remove some of the issues inherent to second-order EDF-based SRT operators but can effectively allow for cheaper simulations of a given configuration as they can allow for a reduction of the number of grid-points and discrete time-steps.

This approach follows a similar paradigm to raw MRT while a distinct set of moments is employed, namely the central moments represented as $\widetilde{m}_{x,y,z}$, and defined as follows [61, 68]:

$$\widetilde{\boldsymbol{m}}_{x^i y^j z^k} = \sum_{\alpha=0}^{q} (c_{\alpha,x} - u_x)^i (c_{\alpha,y} - u_y)^j (c_{\alpha,z} - u_z)^k \boldsymbol{f_\alpha} \tag{2.17}$$

The MRT collision operator in central Hermite moments (also known as cascaded) space with a full Hermite expansion of the EDF has been shown to have better numerical properties than other choices of moments space. The collision operator can be written as follows in the MRT approach.

$$\Omega_\alpha = \boldsymbol{\mathcal{M}^{-1}\mathcal{N}^{-1}\mathcal{S}\mathcal{N}\mathcal{M}} \left(\boldsymbol{f_\alpha^{(eq)}} - \boldsymbol{f_\alpha} \right) + \Xi_i \tag{2.18}$$

where $\mathcal{M}$ and $\mathcal{M}^{-1}$ are the moments transform tensor and its inverse, $\mathbf{S}$ is the diagonal tensor of relaxation rates. The matrix $\boldsymbol{N}$ is introduced that serves to transform raw moments into central moments:

$$\widetilde{\boldsymbol{m}} = \boldsymbol{\mathcal{N}}\boldsymbol{m} \tag{2.19}$$

The moments transform tensor is defined via a set of modified central Hermite polynomials $\widetilde{\mathcal{H}}_n(\boldsymbol{c}_\alpha)$, which for the D3Q27 stencil are:

$$\begin{aligned}\widetilde{\mathcal{H}}_n \in \{&\widetilde{\mathcal{H}}_0, \widetilde{\mathcal{H}}_x, \widetilde{\mathcal{H}}_y, \widetilde{\mathcal{H}}_z, \widetilde{\mathcal{H}}_{xy}, \widetilde{\mathcal{H}}_{xz}, \widetilde{\mathcal{H}}_{yz}, \widetilde{\mathcal{H}}_{xx} - \widetilde{\mathcal{H}}_{yy}, \widetilde{\mathcal{H}}_{xx} - \widetilde{\mathcal{H}}_{zz}, \widetilde{\mathcal{H}}_{xx} + \widetilde{\mathcal{H}}_{yy} + \widetilde{\mathcal{H}}_{zz},\\ &\widetilde{\mathcal{H}}_{xyz}, \widetilde{\mathcal{H}}_{xxy}, \widetilde{\mathcal{H}}_{xxz}, \widetilde{\mathcal{H}}_{xyy}, \widetilde{\mathcal{H}}_{yyz}, \widetilde{\mathcal{H}}_{xzz}, \widetilde{\mathcal{H}}_{yzz}, \widetilde{\mathcal{H}}_{xxyy}, \widetilde{\mathcal{H}}_{xxzz}, \widetilde{\mathcal{H}}_{yyzz},\\ &\widetilde{\mathcal{H}}_{xxyz}, \widetilde{\mathcal{H}}_{xyyz}, \widetilde{\mathcal{H}}_{xyzz}, \widetilde{\mathcal{H}}_{xyyzz}, \widetilde{\mathcal{H}}_{xxyzz}, \widetilde{\mathcal{H}}_{xyzz}, \widetilde{\mathcal{H}}_{xxyyzz}\}.\end{aligned} \tag{2.20}$$

For a more in-depth exploration of central Hermite polynomials, we recommend interested readers to [53]. Based on the above polynomials in D3Q27, equilibrium moments are the central Hermite coefficients $\widetilde{a}_n^{\mathrm{eq}}$, which for the equilibrium distribution function:

$$\begin{aligned}\widetilde{a}_n^{\mathrm{eq}} \in \{&\rho, 0, 0, 0, 0, 0, 0, 0, 0, 3(p - \rho c_s^2), 0, 0, 0, 0, 0, 0, 0,\\ &(p - \rho c_s^2)^2, (p - \rho c_s^2)^2, (p - \rho c_s^2)^2, 0, 0, 0, 0, 0, 0, (p - \rho c_s^2)^3\}.\end{aligned} \tag{2.21}$$

Setting $p = \rho c_s^2$, all equilibrium coefficients reduce to zero except at order zero. The relaxation frequency tensor S is defined as:

$$\begin{aligned}S = \mathrm{diag}(&1, 1, 1, 1, \omega_s, \omega_s, \omega_s, \omega_s, \omega_s, \omega_b, \omega_g,\\ &\omega_g, \omega_g, \omega_g, \omega_g, \omega_g, \omega_g, \omega_g, \omega_g, \omega_g, \omega_g, \omega_g, \omega_g, \omega_g, \omega_g, \omega_g),\end{aligned} \tag{2.22}$$

where the operator diag is defined as:

$$\mathrm{diag}(\boldsymbol{A}) = (\boldsymbol{A} \otimes \mathbf{1}) \circ \boldsymbol{I}, \tag{2.23}$$

for a given vector $\boldsymbol{A}$, with $\mathbf{1}$ a vector with elements 1, $\boldsymbol{I}$ the unitary tensor, and $\circ$ the Hadamard product, while ω_s, ω_b and ω_g are the shear, bulk, and ghost-modes relaxation frequency, respectively. The quantity ω_b is related to the bulk viscosity, η, as [69]:

$$\omega_b = \frac{\delta t}{(\frac{2+D}{D} - \frac{\partial \ln p}{\partial \ln \rho})\frac{\eta}{p} + \delta t/2}, \tag{2.24}$$

while the shear modes relax with:

$$\omega_s = \frac{\delta t}{\frac{\mu}{p} + \delta t/2}, \tag{2.25}$$

and $\omega_g = 1$. The correction term for the diagonal components of the third-order moments appearing in Eq. 2.18 changes in the context of the multiple relaxation time collision operator

into:

$$\Xi_i = \left(1 - \frac{\omega_b \omega_s}{\omega_b + \omega_s}\right) \frac{w_i}{2c_s^4} \left(\boldsymbol{\nabla} \mathcal{H}_2\right) : \Delta_3^{\mathrm{eq}}. \tag{2.26}$$

The MRT model allows for an independent bulk viscosity and Galilean-invariant dynamic and bulk viscosities. It is essential to emphasize that throughout this study, all LBM equations are presented in S.I. units, and no non-dimensionalization has been applied.

2.4 Extension to non-Newtonian viscosity models

2.4.1 The shear strain tensor

The non-Newtonian viscosity laws typically involve dependence on the shear rate $\dot{\gamma}$ defined as:

$$\dot{\gamma} = \sqrt{2D_{II}}, \tag{2.27}$$

where D_{II} is the second invariant of the rate-of-strain tensor. The rate-of-strain tensor is defined as the symmetric part of the tensor $\boldsymbol{\nabla u}$:

$$S = \frac{1}{2}\left(\boldsymbol{\nabla u} + \boldsymbol{\nabla u}^{\dagger}\right), \tag{2.28}$$

where $\dagger$ is the conjugate transpose operator. The strain rate can in turn be decomposed into a trace-less part modeling pure shear strain and a diagonal-only tensor taking into account compression/dilatation:

$$S = \underbrace{\frac{1}{2}\left(\boldsymbol{\nabla u} + \boldsymbol{\nabla u}^{\dagger} - \frac{2}{D}\boldsymbol{\nabla} \cdot \boldsymbol{u}\boldsymbol{I}\right)}_{\mathrm{trace}=0} + \underbrace{\frac{1}{D}\boldsymbol{\nabla} \cdot \boldsymbol{u}\boldsymbol{I}}_{\mathrm{trace}=\boldsymbol{\nabla}\cdot\boldsymbol{u}}. \tag{2.29}$$

where D designates the number of physical dimensions of the system. It is well-known that for incompressible flows the divergence of the velocity field goes to zero meaning only the traceless part of the rate-of-strain tensor is to be considered in those regimes. As such we only consider the traceless part of the rate-of-strain tensor to compute its second invariant:

$$D_{II} = \left(S - \frac{1}{D}\mathrm{trace}(S)\right) : \left(S - \frac{1}{D}\mathrm{trace}(S)\right), \tag{2.30}$$

which for a 2-D system would result in:

$$D_{II} = 2S_{xy}^2 + \frac{1}{2}(S_{xx} - S_{yy})^2, \tag{2.31}$$

while in 3-D:

$$D_{II} = 2\left(S_{xy}^2 + S_{xz}^2 + S_{yz}^2\right) + \frac{2}{3}\left(S_{xx}^2 + S_{yy}^2 + S_{zz}^2 - S_{xx}S_{yy} - S_{xx}S_{zz} - S_{yy}S_{zz}\right). \tag{2.32}$$

While one can directly evaluate these terms via finite-difference approximations to the gradient of the velocity field, the lattice Boltzmann method allows for a fully local evaluation. The next subsection will derive this local evaluation.

2.4.2 Local computation of rate-of-strain in lattice Boltzmann

Although already available in the literature [70], we will provide here a short derivation of the expression of the rate-of-strain tensor from lattice Boltzmann populations for the sake of a better readability. It is well-known that applying a multi-scale perturbation analysis one can recover macroscopic equations at different scales in the perturbation parameter, here ε, i.e. Euler and Navier-Stokes equations. At scale ε^2, after expansion of all terms in ε one recovers the following equation:

$$\partial_t^{(2)} f_\alpha^{\mathrm{eq}} + D_t^{(1)} \left(1 - \frac{\omega}{2}\right) f_\alpha^{(1)} = -\omega f_\alpha^{(2)}. \tag{2.33}$$

The first-order moment of this equation should recover Navier-Stokes-level contributions to the momentum balance equation. Knowing that the zeroth- and first-order moments of $f^{(1)}$ are null as a result of the solvability conditions:

$$\partial_t^{(2)} \rho \boldsymbol{u} + \boldsymbol{\nabla} \underbrace{\left(1 - \frac{\omega}{2}\right) \sum_\alpha \boldsymbol{c}_\alpha \otimes \boldsymbol{c}_\alpha f_\alpha^{(1)}}_{=2\mu S} = 0, \tag{2.34}$$

which leads to:

$$S = \frac{1}{2\mu} \left(1 - \frac{\omega}{2}\right) \sum_\alpha \boldsymbol{c}_\alpha \otimes \boldsymbol{c}_\alpha f_\alpha^{(1)}, \tag{2.35}$$

where μ and ω are the dynamic viscosity and relaxation frequency, respectively. Using the definition:

$$\omega = \frac{\delta_t}{\mu/p + \delta_t/2}, \tag{2.36}$$

where p is pressure, which for the isothermal lattice Boltzmann reduces to $p = \rho c_s^2$ with $c_s^2 = \frac{\delta_x^2}{3\delta_t^2}$, and δ_x the grid-size, and an approximation for $f^{(1)}$:

$$f_\alpha^{(1)} \approx f_\alpha - f_\alpha^{\mathrm{eq}}, \tag{2.37}$$

one gets the final expression:

$$S = \frac{\omega}{2p\delta_t} \sum_\alpha \boldsymbol{c}_\alpha \otimes \boldsymbol{c}_\alpha \left(f_\alpha - f_\alpha^{\mathrm{eq}}\right). \tag{2.38}$$

Going back to the model with the modified central Hermite polynomial collision operator and combining Eqs. 2.27, 2.30 and 2.38 in 2-D one gets:

$$\dot{\gamma} = \frac{\omega_s}{2p} \sqrt{4\widetilde{a}_{xy}^2 + \widetilde{a}_{xx-yy}^2}, \tag{2.39}$$

while in 3-D:

$$\dot{\gamma} = \frac{\omega_s}{2p}\sqrt{4\widetilde{a}_{xy}^2 + 4\widetilde{a}_{xz}^2 + 4\widetilde{a}_{yz}^2 + \frac{2}{3}(\widetilde{a}_{xx-yy} - 2\widetilde{a}_{xx-zz})^2 + \frac{2}{3}(\widetilde{a}_{xx-zz} - 2\widetilde{a}_{xx-yy})^2}. \tag{2.40}$$

which in turn leads to the following implicit equation:

$$\frac{\mu(\dot{\gamma})}{p} - \frac{\delta_t}{\omega_s} + \frac{\delta_t}{2} = 0, \tag{2.41}$$

where $\mu(\dot{\gamma})$ can be any one of the non-Newtonian viscosity laws. ω_s is the shear relaxation frequency. The viscosity can be either obtained via a simple explicit approximation as:

$$\omega_s(t) = \frac{\delta_t}{\frac{\mu(\dot{\gamma}(t-\delta_t))}{p(t)} + \frac{\delta_t}{2}}, \tag{2.42}$$

or by iteratively solving Eq. 2.41. In the present study, the second approach is adopted as it naturally leads to more accurate results.

2.5 Boundary conditions

The application of patient-specific boundary conditions has been demonstrated to improve the precision and reliability of cardiovascular simulation parameters, including wall shear stress and pressure gradients [71]. While boundary conditions are instrumental in determining the accuracy of fluid simulations and effectively representing patient hemodynamics [72], defining boundary conditions in LBM presents a significant challenge since traditional boundary conditions are specified for macroscopic variables like pressure or velocity in hydrodynamic problems, not for the main LB variables, which are the distribution functions f_α. At the boundary, the incoming distribution functions (pointing into the fluid domain) are unknown after the propagation step and must be determined. Consequently, establishing suitable relationships between the incoming and outgoing distribution functions is crucial to reproduce the desired macroscopic behavior at the domain's boundary.

S. Succi [27] distinguishes between elementary and complex boundary conditions. Elementary boundary conditions are applied when the boundary aligns with the coordinates of the grid, whereas complex boundaries may cut across mesh cells. The subsequent sections will detail the boundary conditions utilized in this study, encompassing inflow/outflow boundary conditions and no-slip boundary conditions.

2.5.1 Inflow and outflow boundary conditions

Inlet and outlet boundary conditions are significant both mathematically and physically as the type of condition helps determine the specific solution. Even though the volume fraction of the total fluid domain may be small, the numerical effects of the inlet and outlet conditions propagate throughout the entire geometry. Therefore, they play a key role in correctly

describing patient hemodynamics in numerical studies [72]. Despite the growing applications of LBM in blood flow analysis, a unified scheme for implementing inlet and outlet boundary conditions is lacking. This absence poses challenges in treating boundaries appropriately when simulating physiological flow in anatomically realistic geometries. Inaccurate implementations can result in issues such as unrealistic flow distributions, nonphysiological velocity and pressure profiles, and imprecise predictions of wall deformation [73, 74].

Inlet velocity and outlet pressure boundary conditions: Dirichlet boundary condition was developed by Zou and He to apply pressure or velocity at a straight boundary [75]. The fundamental concept of the Zou-He boundary condition involves solving for the unknown distributions by bouncing back the nonequilibrium component of the distribution function. The boundary condition is characterized by its local operations, making it easily implementable in parallel. In the case of D3Q19, there are five unknown distributions after the streaming step. The equation used to calculate these unknown distributions is given by:

$$f_{\bar{\alpha}} = f_{\alpha} - \frac{2\omega_{\alpha}\rho}{c_s^2}(\mathbf{c}_{\alpha} \cdot \mathbf{u}) - \frac{\rho}{3}(\mathbf{t}_{\alpha} \cdot \mathbf{u}) + \frac{1}{2}\sum_{\beta=0}^{18} f_{\beta}(\mathbf{t}_{\alpha} \cdot \mathbf{c}_{\beta})(1 - |\mathbf{c}_{\beta} \cdot \mathbf{n}|) \tag{2.43}$$

where f_{α} represents the distributions streaming into the boundary, $f_{\bar{\alpha}}$ denotes the bounce-back populations, $\mathbf{c}_{\alpha}$ are the direction vectors, $\mathbf{n}$ is the outward normal vector, and $\mathbf{t}_{\alpha}$ is computed as follows:

$$\mathbf{t}_{\alpha} = \mathbf{c}_{\alpha} - (\mathbf{c}_{\alpha} \cdot \mathbf{n})\mathbf{n}. \tag{2.44}$$

The continuity relation allows the specification of three out of the four macroscopic variables-density ρ and the three components of velocity $\mathbf{u}$. The last variable is computed from the distribution function. Specifically, we employ the complete velocity $\mathbf{u}$ for inlet conditions, whereas density ρ is specified at the outlet.

2.5.1.1 Dynamic boundary condition (Velocity)

Since patient-specific inflow profiles based on 4D MRI are not commonly available, specifying physiological velocity conditions at the inlet presents a nontrivial task, especially in complex vascular geometries. Various inlet velocity conditions, such as parabolic or Womersley profiles, are employed in hemodynamic simulations [76]. Determining the velocity as a function of the geometric center and radius of the inlet is straightforward when the inlet surface is approximately circular. However, for irregular inlet surfaces, our solver enables the computation of an accurate velocity profile for patient-specific aneurysms with complex inlets. To demonstrate the utility and validate the inlet velocity profile, we conducted a numerical test using Womersley flow.

Benchmarking of Womersley flow: Pulsatile behavior is a characteristic feature of the cardiovascular system, and it has a significant impanct on both the aneurysm wall and the flow field within blood vessels. Many numerical studies adopt a pulsatile velocity profile as the inlet boundary condition to replicate the pulsatile nature of blood flow.

The Womersley flow similar to Poiseuille flow serves as a well-established benchmark in fluid dynamics. It simulates the flow of an incompressible fluid within a cylindrical tube under a reference pressure. However, the distinguishing feature is that the pressure gradient in the channel direction varies with time, mirroring the flow characteristics found in large arteries. Researchers often employ this scenario to study pulsatile flow within medical flow simulation.

In this benchmark, a three-dimensional Womersley flow is driven by the periodic varying pressure gradient at the inlet. The pressure gradient follows the following equation:

$$\frac{\partial P}{\partial x} = -P^* e^{i\omega t} \tag{2.45}$$

where P^* is the maximal amplitude of the sinusoidally varying pressure signal and ω is the angular frequency.

The Reynolds number is defined below:

$$\mathrm{Re} = \frac{2\mathrm{U_c R}}{\nu} \tag{2.46}$$

where R is the radius of the axisymmetric pipe, ν is the kinematic viscosity of the fluid, U_c is the characteristic velocity defined as

$$U_c = \frac{P^*\alpha^2}{4\omega\rho} = \frac{P^* R^2}{4\rho\nu} \tag{2.47}$$

where α is the Womersley number, which is defined as

$$\alpha = R\sqrt{\frac{\omega}{\nu}} \tag{2.48}$$

The analytical solution for three-dimensional axisymmetric pipe pulsatile flow is given as [77]:

$$u(r,t) = \mathrm{Re}\left\{ \frac{\mathrm{P^*}}{\mathrm{i}\omega\rho_0} \left[1 - \frac{\mathrm{J}_0\left[\frac{1}{\sqrt{2}}(-\alpha + \mathrm{i}\alpha)\frac{\mathrm{r}}{\mathrm{R}}\right]}{\mathrm{J}_0\left[\frac{1}{\sqrt{2}}(-\alpha + \mathrm{i}\alpha)\right]} \right] \mathrm{e}^{\mathrm{i}\omega\mathrm{t}} \right\} \tag{2.49}$$

where J_0 is the zeroth-order Bessel function.

In this validation, the initial velocity is set to zero in the entire domain. Womersley number α and Reynolds number Re are 8 and 1200, respectively. The period T is 1200 s. The characteristic velocity is 1.025 m/s. The radius is 1 m. Data sampling starts from the $10T$ step.

The normalized velocity u_x profiles obtained with the LBM simulations are displayed at different time instants in Figure 2.1. It can be seen that this comparison shows excellent agreement between numerical results (circular symbols) and analytical solutions (lines).

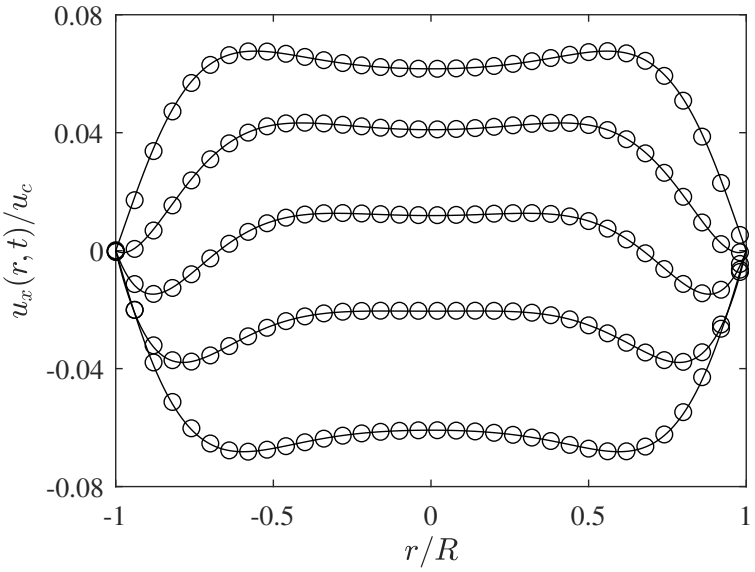

Figure 2.1: Velocity profiles along the diameter over a period. From top to bottom, time is $0.25T$, $0.38T$, $0.46T$, $0.55T$, $0.71T$. Comparison between numerical results (circular symbols) and analytical solutions (lines).

2.5.2 Flat walls

The LBM is conventionally founded on an orthogonal, equidistant lattice structure. A common approach involves the representation of the boundary using a "staircase" and applies the standard bounce-back wall boundary conditions [78]. The boundary conditions in LBM can be classified into heuristic schemes, hydrodynamic schemes, and interpolation/extrapolation schemes. In this context, we focus on the heuristic scheme. This scheme is devised based on the dynamics of fluid particles encountering a wall and it includes standard bounce-back, modified bounce-back, half-way bounce-back, and specular-reflection. The bounce-back scheme is the most commonly used rule for stationary non-slip walls. It assumes that a particle simply reverses its velocity after colliding with the wall. Mathematically, it means that the post-collision distribution function at a boundary node x_b is

$$f'_{\bar{\alpha}}(\mathbf{x_b}, t) = f'_{\alpha}(\mathbf{x_f}, t) \tag{2.50}$$

where $\mathbf{x_b}$ and $\mathbf{x_f}$ are a node located on the wall and the neighboring fluid node, respectively.

Based on the collision-streaming process, the bounce-back scheme can also be expressed in alternative formulations,

$$f'_{\bar{\alpha}}(\mathbf{x_f}, t + \delta_t) = f'_{\alpha}(\mathbf{x_f}, t) \tag{2.51}$$

2.5.3 Curved walls

The ability of the LBM to accurately model intricate geometries can be complex itself, mainly because of the utilization of a Cartesian grid and the intricate boundary handling along

curved surfaces. When approximating a curved boundary with a staircase-like representation, several issues can arise that can be categorized into two main problems.

Firstly, there is the challenge of representing complex geometries, since the Cartesian grid used in the LBM does not inherently align with curved boundaries. This misalignment can lead to inaccuracies when trying to represent intricate shapes. Secondly, implementing correct boundary conditions can be difficult. During the streaming operation, situations can arise where incorrect distribution functions originate from solid nodes located outside the fluid domain. These issues with boundary conditions can lead to erroneous results and further complicate the simulation.

Several approaches have been proposed to address the challenges of simulating complex geometries using the LBM. These methodologies aim at accurately handling the representation of curved boundaries and implement appropriate boundary conditions.

- **Extrapolation scheme with castellated approach**: In this approach, the boundary is approximated using lattice nodes that are closest to the curved surface [79]. This technique involves a castellated approach where adjacent nodes streaming to the castellated boundary nodes lie within the solid domain. Distribution functions at these solid nodes are then computed using a second-order extrapolation method.
- **Linear interpolation method**: This technique involves interpolating between a fictitious equilibrium distribution function and a carefully chosen near-boundary distribution function using a simple linear interpolation [80].
- **Combined bounce-back and interpolation scheme**: Lallemand and Luo [81] developed a technique that combines the bounce-back scheme with an interpolation scheme. The bounce-back scheme is used to handle stationary boundaries, while an additional term is introduced to simulate moving boundaries.

Each approach offers unique advantages and considerations depending on the specific simulation requirements and geometries involved. Given the complex nature of geometries considered in aneuryms, appropriate treatment of wall boundaries and their curvature is an important point. In the context of the present study, the curved-boundary bounce-back formulation proposed in [82] is used. An intuitive approach is employed following the one-dimensional scenario depicted in Figure 2.2. The position of the wall is determined by the ratio of CF/CD. When a particle departs from node C and undergoes reflection upon encountering wall (referred to as bounce back scenario), the particle will not reach a fluid node after moving one grid size. An exception to this occurs when the ratio q equals to 0, 1/2, or 1. Consequently, following the collision step, the distance CE remains indeterminate. To address this challenge, the following scheme was put forward:

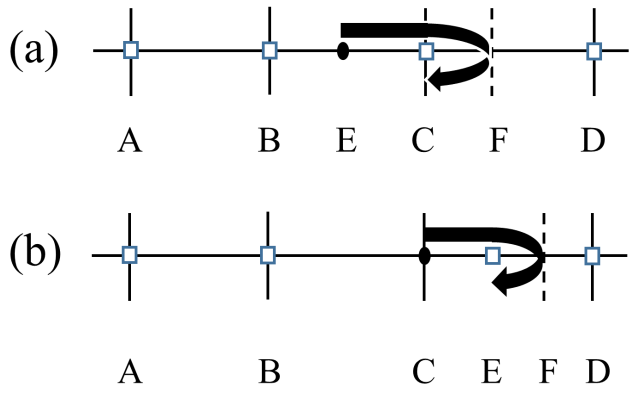

Figure 2.2: Illustration of the collision process. The dashed line indicates the wall. (a) q $<$ 1/2. (b) q $\geq$ 1/2.

At a given boundary node $\boldsymbol{x}_f$, the missing incoming populations are computed as:

$$f_\alpha(\boldsymbol{x}_f, t+\delta_t) = 2q f_{\bar{\alpha}}(\boldsymbol{x}_f + \boldsymbol{c}_{\bar{\alpha}}, t+\delta_t) + (1-2q)\, f_{\bar{\alpha}}(\boldsymbol{x}_f, t+\delta_t), \forall q < \frac{1}{2}, \tag{2.52a}$$

$$f_\alpha(\boldsymbol{x}_f, t+\delta_t) = \frac{1}{2q} f_{\bar{\alpha}}(\boldsymbol{x}_f + \boldsymbol{c}_{\bar{\alpha}}, t+\delta_t) + \frac{2q-1}{2q} f_{\bar{\alpha}}(\boldsymbol{x}_f, t+\delta_t), \forall q \geq \frac{1}{2}, \tag{2.52b}$$

where $\bar{\alpha}$ designates the direction opposite α and q:

$$q = \frac{||\boldsymbol{x}_f - \boldsymbol{x}_s||}{||\boldsymbol{c}_\alpha||}, \tag{2.53}$$

with $\boldsymbol{x}_s$ denoting the wall position in direction α.

The proposed scheme stands out from other schemes by exclusively utilizing interpolations instead of extrapolations, thereby enhancing its stability. Additionally, the continuity in the change of q in equations contributes to the scheme's smoothness. Notably, when $q = 1/2$, the interpolation formulas simplify to the bounce-back scheme. The proposed scheme is less intricate, as it focuses on the interaction of the fluid with the boundary, specifically coupling populations f_α, $f_{\bar{\alpha}}$ with opposite velocities.

Chapter 3

Validation and preliminary studies

Contents

3.1 An in-vitro validation study

Part of this section has been published as:
Seyed Ali Hosseini, Philipp Berg, **Feng Huang**, Christoph Roloff, Gábor Janiga, and Dominique Thévenin. Central moments multiple relaxation time LBM for hemodynamic simulations in intracranial aneurysms: an in-vitro validation study using PIV and PC-MRI. Computers in Biology and Medicine, 131:104251, 2021.

3.1.1 Introduction

Since a reliable and clinically applicable rupture risk assessment procedure remains challenging until now, increasing research effort is being put into developing one. Owing to their non-invasive nature resulting in risk-free (for the patient) assessment of rupture probability and the possibility to access highly resolved velocity fields (in both space and time) CFD studies are becoming increasingly popular [83, 84].

While valuable insights have been gained through such numerical studies [85, 86], a number of challenges and gaps remain to be bridged, before predictive and reliable models based on CFD for aneurysm dynamics can be developed [87, 88]. To put these challenges into perspective, Berg et al. [89] summarized the individual working steps involved in image-based blood flow simulations and provided corresponding recommendations to avoid simulation inaccuracies. As for any numerical simulation, the choice of the numerical solver, resolution and grid configuration are of the utmost importance to ensure convergence of the obtained solutions. The latter two also being consequences of the choice of the numerical method, the former is a determining factor concerning both convergence and efficiency of the solver.

The performances of the employed solvers can only be assessed through a systematic benchmarking/validation procedure against reliable experimental data. One of the most frequently used sources of experimental reference data is the Particle image velocimetry (PIV) relying on laser-based high-speed camera flow measurements [90, 91, 92, 93, 94]. PIV measurements allow for more accurate measurements and higher resolutions as compared to other data acquisition tools such as magnetic resonance imaging (MRI) [95] or cerebral angiography [96]. A number of studies have presented qualitative comparisons of velocity fields for patient-specific aneurysms as obtained from CFD and PIV measurements, and reported good qualitative agreement between the two [3, 97].

While most of the early publications relied on discrete solvers for the Navier-Stokes-Poisson (NSP) equations, e.g. using finite volume (FV) or finite element (FE) methods, emergent numerical methods such as smoothed particle hydrodynamics (SPH) [98, 99] and the LBM [100, 101, 102, 103, 104, 105, 106, 107] are increasingly applied to such flows. Contrary to classical NSP solvers they are not strictly incompressible, as they approximate the low Mach flow regime through appropriate isothermal flow manifolds, and as such rely on a system of purely hyperbolic equations, making the algorithm inherently local. The absence of the elliptic component of the NSP equations allows for dramatic computation cost reduction while the parabolic nature of the partial differential equation (PDE) describing pressure evo-

lution makes the formulation suitable for unsteady simulations – contrary to other weakly compressible formulations such as the artificial compressibility method (ACM). Furthermore, the compressible nature of the formulation (involving a thermodynamic pressure) along with kinetic heuristic boundary closures (such as the bounce-back rule) provide for an efficient and consistent implementation of wall boundaries [49, 108, 109]. The drastic decrease in computation time makes the method more viable compared to approaches based on the NSP equations. Based on these observations, a number of dedicated LBM-based solvers for blood flow simulations have been developed over the past decade, e.g. [101, 110, 111]. For example a research prototype was developed by the Siemens Healthineers AG (Erlangen, Germany), which is increasingly used to address clinical questions [112, 113, 114]. However, it must be noted that the LBM in its simplest form, i.e. with a SRT collision operator and a second-order discrete EDF has a rather limited stability domain. The SRT formulation also leads to a number of other well-documented numerical artifacts including, but not limited to, the (non-dimensional) viscosity-dependence of the solid wall position when used with bounce-back-type boundary treatments [55].

The aim of the present work is to assess the performances of a specific class of MRT operator based on Hermite central moments and a fully expanded EDF. This collision model is shown to alleviate some of the traditional shortcomings of the classical SRT-based solvers, while – through its much wider stability domain – allowing for stable low-resolution simulations. The performances of the central Hermite multiple relaxation time (CHMRT) model are assessed, via our in-house solver ALBORZ [56, 115], through a variety of test-cases spanning ideal and patient-specific geometries considering steady and pulsatile flows. The numerical results are compared with high-resolution in-vitro measurements for validation. They are also compared to results from a SRT solver with second-order EDF to further showcase the added value of the CHMRT collision operator. The issue of under-resolved simulations is also considered by systematically conducting simulations at different (lower) resolutions. It is shown that at low resolution (inaccessible to the SRT collision operator), the proposed scheme is still able to capture properly the flow dynamics.

3.1.2 Case description

To illustrate the points brought forward in the previous section and showcase the performances of the CHMRT collision operator for the applications of interest, three different test cases are considered: (a) ideal aneurysm under steady flow, (b) ideal aneurysm subject to pulsatile flow, and finally (c) patient-specific geometry. While the latter two are intended as detailed validations of the solver against experimental data, the first test case is presented to briefly illustrate the difference between the classical SRT operator and the proposed model.

3.1.2.1 Idealized aneurysm model under steady flow

The first configuration is a rather simple one consisting of an ideal spherical aneurysm of radius 20 mm and vessels of diameter 6 mm positioned with an angle of 90°. The distance between the inlet and the opposite point in the aneurysm sac is 60 mm while for the outlet it is 50 mm. The domain is subject to a constant inflow at the inlet and an open boundary

at the outflow. The case is modeled using both the CHMRT and second-order SRT collision operators at different resolutions. The obtained results are further validated against the commercial finite-volume code STAR-CCM+ 14.04 (Siemens Product Lifecycle Management Software Inc., Plato, TX, USA).

3.1.2.2 Idealized aneurysm model with pulsatile flow

For the purpose of validation, an idealized spherical sidewall aneurysm with a diameter of 20 mm was virtually created. The parent vessel featured a diameter of 4 mm and was bent under an angle of 120° (see Figure 3.1). The 3-D vessel geometry served as basis for the numerical simulation as well as for the phantom manufacturing prior to the in-vitro PIV measurements. Based on the 3-D CAD model, a transparent phantom model was manufactured

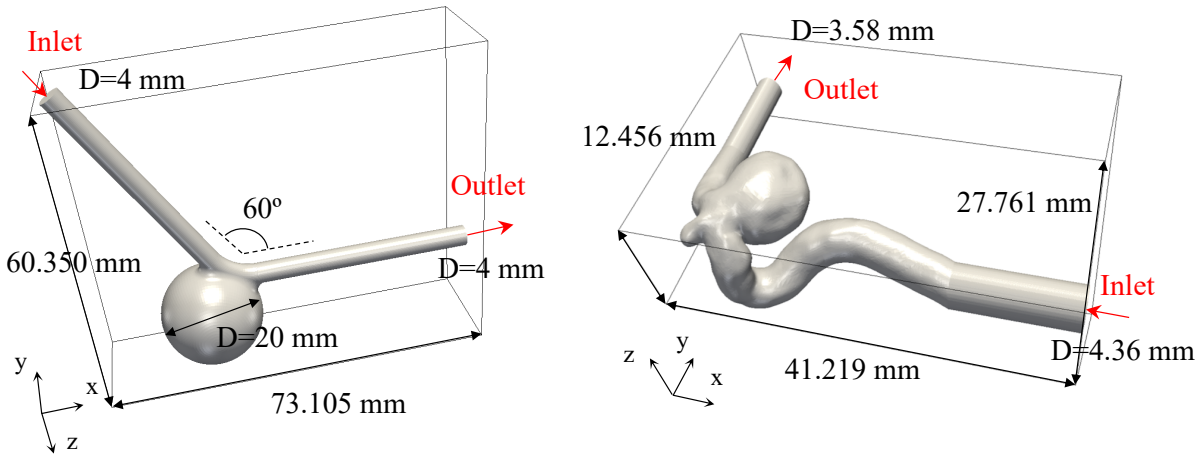

Figure 3.1: (left) Idealized aneurysm geometry as used both for the phantom manufacturing and subsequent PIV measurement and in LB simulation [2], and (right) Segmentation of the patient-specific intracranial aneurysm model used for the LBM simulations and the in-vitro validation [3].

using a lost-core technique that resulted in a silicone block incorporating the hollow vessel structure. The refractive index of the silicone was measured to be $n_{\text{silicone}} = 1.4113$ at 22°C (Abbemat 200, Anton Paar, Ostfildern, Germany). As blood analogue liquid (BAL), a mixture of distilled water, glycerin, sodium iodide, and sodium thiosulphate was used to match the refractive index of the silicone block ($n_{\text{BAL}} = 1.4109$) as well as relevant fluid dynamical properties of blood plasma, i.e. density $\rho_{\text{BAL}} = 1221$ kg/m^3. The kinematic viscosity of the fluid used for this configuration was $\nu_{\text{BAL}} = 3.2 \times 10^{-6}$ m^2/s. This corresponds to a dynamic viscosity of $\mu_{\text{blood}} = 4.03 \times 10^{-3}$ Pa.s (assuming a density of $\rho_{\text{blood}} = 1222$ kg/m^3).

During the PIV measurements, the phantom was placed inside a transparent acrylic box with two inclined walls and filled with index-matching fluid. A laser light sheet was directed to illuminate the sagittal plane of the aneurysm. As seeding for the PIV measurements, small

resin microspheres doped with Rhodamine B (diameter d=10.46 $\pm$ 0.18 μm, density ρ = 1510 kg/m^3) were used. The two stereoscopic PIV high-speed cameras (sCMOS, 2560 $\times$ 2160 pixel) observed the flow through the inclined windows from the side of the acrylic box to minimize optical aberrations such as astigmatism.

A micro-gear pump (HNP Mikrosysteme, Schwerin, Germany) delivered the periodic flow, which was monitored by an ultrasonic flowmeter (Sonotec, Halle, Germany). The average velocity at the inflow cross section is displayed in Figure 3.2 over one entire cycle (maximum Reynolds number $\mathrm{Re}_{\max} = 1025$ and Womersley number $\mathrm{Wo} = 2.54$). The original flow curve is based on 4-D flow measurements in a 7T phase contrast magnetic resonance imaging (PC-MRI) – Siemens Magnetom. Further details regarding the flow acquisition can be found in [116]. To ensure a fully developed laminar flow profile the inlet connector to the phantom consisted of a 500 mm straight tubing. The PIV double frame recordings were conducted at a frequency of 500 Hz (triggered by the pump control), where the interframe time was set to 200 μs. In total, 36 periodic cycles were recorded, resulting in 36,000 double frame pairs. Velocity processing was conducted via DaVis 8.4.0 (LaVision, Göttingen, Germany) using a multi-pass stereo cross-correlation with a final interrogation window size of 32 $\times$ 32 px and 50 % overlap, resulting in one velocity vector every 141 μm. The velocity fields were then phase-averaged. Additional details on the PIV data acquisition and processing procedure can be found in [2].

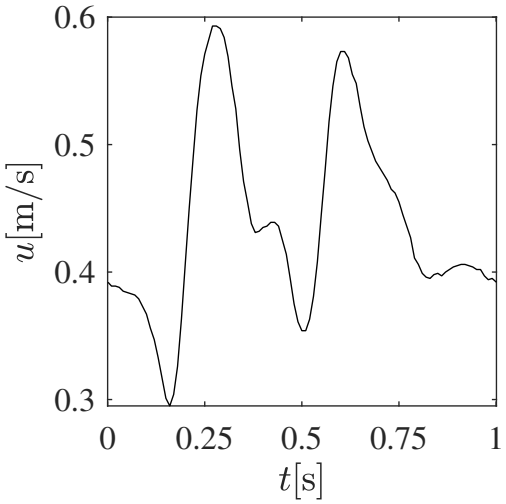

Figure 3.2: Average velocity profile at the inlet over one cardiac cycle for the idealized pulsatile aneurysm.

A pulsatile hemodynamic simulation was carried out using identical conditions compared to the experiment. Specifically, the same geometry and boundary conditions were applied, with a higher temporal and spatial resolution. The LBM simulation was performed using time-step and grid sizes of $\delta_t = 1.5 \times 10^{-5}$ s and $\delta_x = 1.25 \times 10^{-4}$ m, respectively. Two additional lower-resolution simulations were also conducted to provide qualitative/quantitative characterizations of convergence and under-resolution effects. Furthermore, the simulations

were run for multiple cycles and data sampling was carried out at the fourth cycle. The state of the flow, and the absence of any artifacts tied to initial conditions were assessed by monitoring the velocity changes at three points around the aneurysm sac. The obtained results (from the highest resolution simulation) are shown in Figure 3.3.

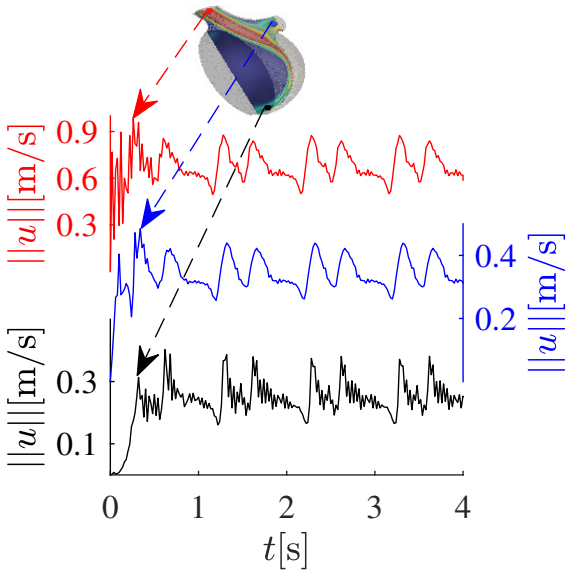

Figure 3.3: Velocity magnitude changes over four cycles at three different monitoring points around the aneurysm sac for the idealized pulsatile aneurysm.

3.1.2.3 Patient-specific aneurysm model with steady inflow

In order to increase the anatomical complexity and enable a qualitative and quantitative comparison in a more realistic scenario, a patient-specific aneurysm was further considered (see Figure 3.1, right). Here, an internal carotid artery aneurysm with a spherical shape was chosen, since this location represents one of the most frequent sites of occurrence. Further, a small aneurysm is located opposite the larger one leading to the formation of interesting flow structures.

To account for the most comprehensive situation from a hemodynamic perspective, peak systolic flow conditions were chosen for the validation. Specifically, a flow rate of 430 mL/min was defined resulting in a Reynolds number of $\mathrm{Re}_{\mathrm{peak}} = 563$ and a corresponding mean velocity in the proximal vessel of 0.512 m/s, respectively.

Equivalent to the experiments described in the previous section, stereoscopic PIV measurements were carried out to obtain in-vitro flow data. Specifically, the micro-gear pump (HNP Mikrosysteme, Schwerin, Germany) provided the desired flow rate of $Q = 430.4 \pm 1.5$ mL/min and 500 recordings were taken at 5 Hz. The velocity processing was conducted via DaVis 8.4.0 (LaVision, Göttingen, Germany), which included a multi-pass cross-correlation with a final interrogation window size of 32×32 px (corresponding to 208×208 μm) and 50 %

overlap. This resulted in a velocity vector every 104 μm. The final results were obtained by averaging all processed recordings.

In addition to the PIV acquisitions, phase-contrast PC-MRI measurements were carried out in a 7 Tesla whole-body system (Siemens Healthineers, Forchheim, Germany) with a voxel size of $570 \times 570 \times 570$ μm^3. The measurements were repeated six times and afterwards the data were averaged. Before evaluation, eddy currents and other background phase effects were corrected using a second dataset with identical scan parameters. For further details regarding the scan parameters and the data processing the interested reader is referred to [3, 117].

For the corresponding LBM simulation, similar to the idealized geometry, blood is assumed to be a Newtonian fluid with density $\rho = 1221$ kg/m^3 and kinematic viscosity $\nu = 3.2 \times 10^{-6}$ m^2/s, a valid choice since shear-thinning effect in the considered neurovasculature are negligible. The time-step and grid sizes were set to $\delta_t = 5 \times 10^{-6}$ s and $\delta_x = 1 \times 10^{-4}$ m, respectively. This choice of parameters led to a non-dimensional relaxation coefficient of $\frac{\tau}{\delta_t} = 0.506$ and a maximum non-dimensional velocity of $\frac{u_{\max}\delta_t}{\delta_x} \approx 0.064$. To further highlight the added value of the collision operator for under-resolved flows, an additional low-resolution simulation with $\delta_t = 1 \times 10^{-5}$ s and $\delta_x = 2 \times 10^{-4}$ m, leading to $\tau/\delta_t = 0.503$, was performed. It is worth noting that using the SRT collision operator at this resolution led to unstable simulations, as confirmed by linear stability maps found in the literature [48].

3.1.3 Results

In the following, qualitative and quantitative comparisons between the hemodynamic simulations based on the LB approach and the in-vitro phantom measurement are presented.

SRT vs CHMRT: Idealized aneurysm with steady flow-rate

As a first step, before going into detailed validation of the solver against experimental data, we present a brief comparative study of the solver (against a classical SRT solver) through a simple test case. The steady-state velocity profiles along the incoming and outgoing vessels, as obtained from the different simulations are shown in Figure 3.4. The simulations using the classical SRT model were conducted using three different resolutions, i.e. $\delta_x = 3.33 \times 10^{-4}$, 2.22×10^{-4} and 1.11×10^{-4} m (R1, R2, and R3 in Figure 3.4). For the CHMRT only one simulation at $\delta_x = 3.33 \times 10^{-4}$ was conducted. It can clearly be observed that at the lowest resolution, the CHMRT solver matches results from the SRT simulation with the highest resolution, and even surpasses it in some regions. The low-resolution SRT simulation exhibits clear underestimation of the maximum velocity at the center of the inflow vessel. The CHMRT simulation on the other hand, even through relying on a grid-size three times that of the highest resolution SRT, is the closest to the reference STAR-CCM+ simulation, showing the superior performances of the former. It is worth noting that the differences observed near the inlet are to be expected, due to the different ways boundary conditions are applied. The length of the inlet pipe, as observed in the velocity distribution plots, guarantees that at the inlet of the sac the velocity profiles are established for all simulations.

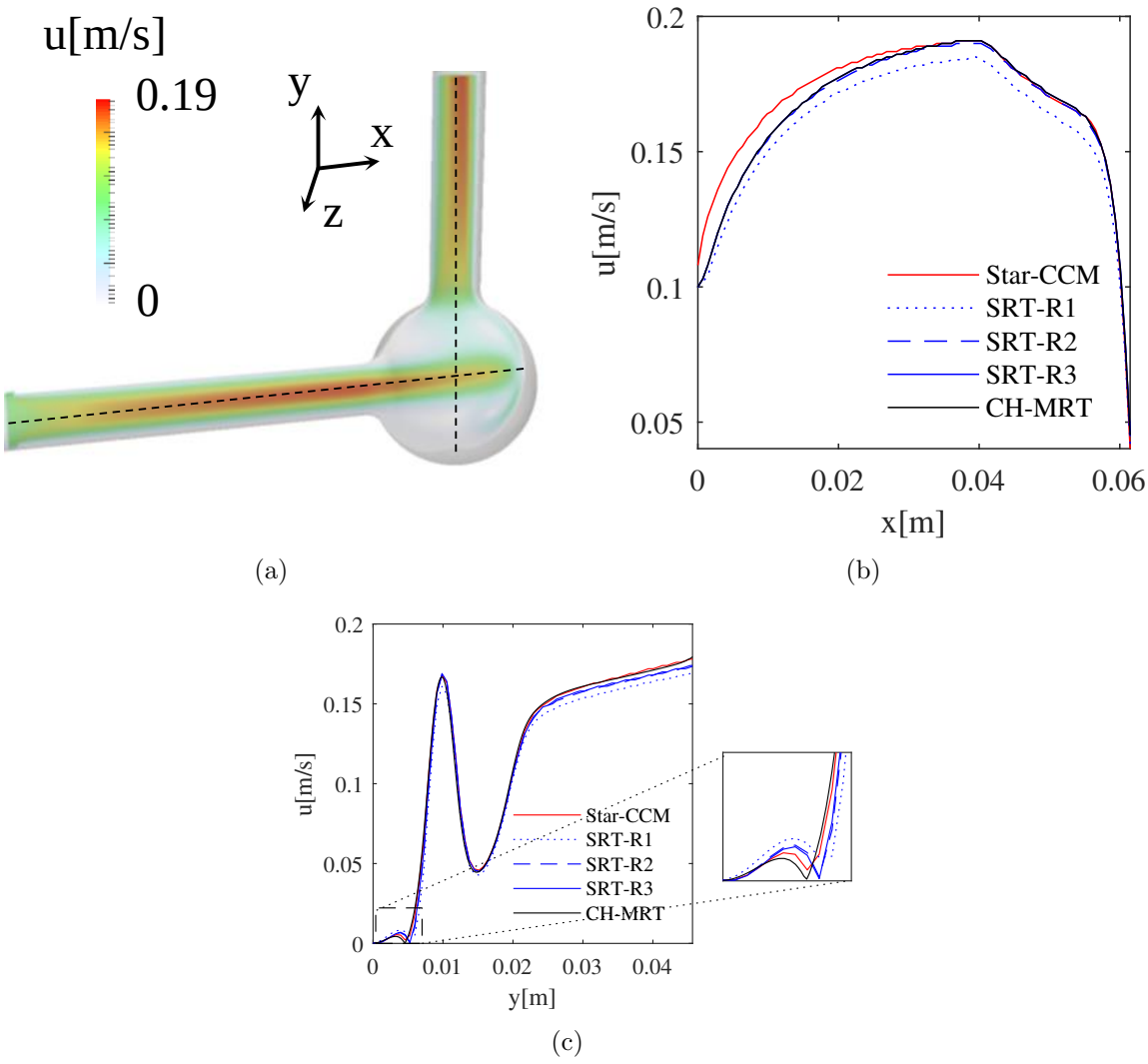

Figure 3.4: (a) Geometrical configuration of the steady flow in the idealized aneurysm, (b) velocity distribution in the $x-$direction, and (c) velocity distribution in the $y-$direction (along the dashed lines shown in the left subfigure).

Idealized aneurysm model with pulsatile inflow

The angle of the model for the second case was chosen in a way that the flow can enter into the sac through the distal part of the aneurysm ostium. After impinging on the aneurysm wall, the flow aligns along the perfect spherical shape. This forms a large vortex within the aneurysm with a stagnation zone approximately at the center of the sac.

The comparison between the experimental (PIV) and the numerical (LBM) flow acquisition demonstrates an excellent agreement within the considered plane (perpendicular to the z-axis passing through the center of the aneurysm sac). Results for 11 different times spanning a cycle are shown in Figure 3.5. Almost identical flow structures are captured and slight

deviations are only visible in the outflow region of the aneurysm close to the peak-systolic time point (0.4 s). Additionally, minor differences can be observed most notably in the form of, less pronounced, unsteady structures not observed in the experimental data. The absence of these structures can partially be explained by the data acquisition modes in experiments and simulations. While the time-dependent flow field from the PIV are phase-averaged over a number of cycles, those from the simulations represent instantaneous shots from the fourth cycle after initialization. In addition to this qualitative observation, a

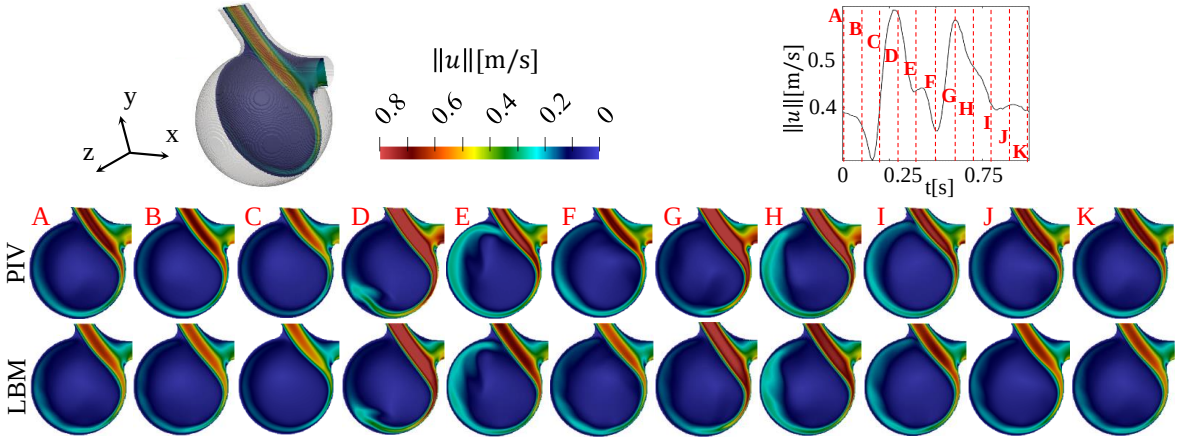

Figure 3.5: Qualitative comparison of the transient flow field between PIV experiments (top row) and LB simulation (bottom row) at eleven different time points covering an entire cardiac cycle (from 0 s to 1 s with $\Delta t = 0.1$ s). The considered plane is shown on the upper left figure. The positions of the snapshots in time (relative to the cardiac cycle) are shown with red dashed lines on the upper right plot.

quantitative comparison is presented in Figure 3.6. Here, the velocity components (u_x and u_y) are compared along two orthogonal lines on the plane perpendicular to the z-axis for three different resolutions, confirming the initial findings: Both experiment and simulation lead to almost identical profiles throughout the cardiac cycle and the numerical approach nearly always occurs within the presented error bars of the measurement. It is worth noting that two additional simulations were performed by setting δ_x to 2×10^{-4} m and 3×10^{-4} m; the corresponding time-steps were set to respectively 1.5×10^{-5} s and 2.2×10^{-5} s. At the lowest resolution, as compared to the highest resolution simulation, the computational cost is reduced by a factor of 25, while velocity profiles are still in very good agreement (and mostly within the error bars) with the experimental data.

Overall, based on both qualitative and quantitative comparisons with PIV data, it is shown that the solver is able to correctly capture the flow structure and match experimental observations. The good agreement is still well maintained even for relatively under-resolved simulations.

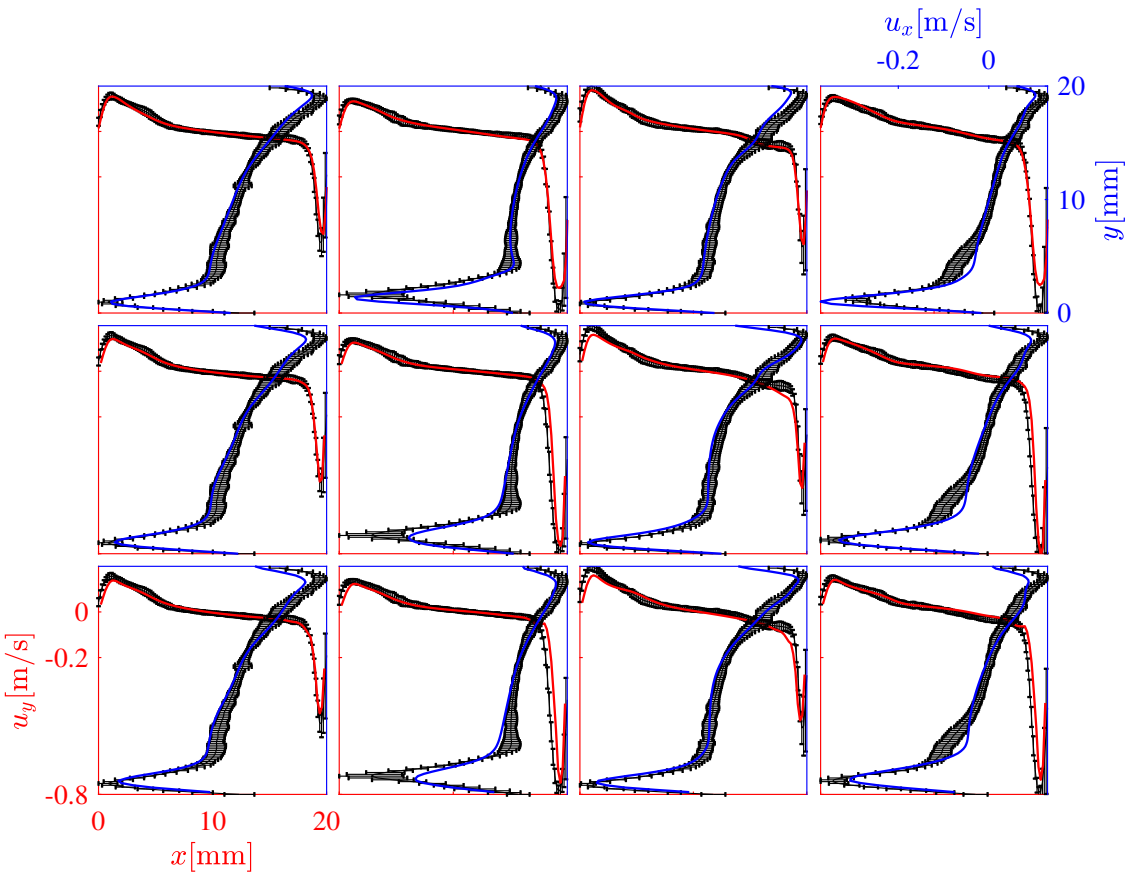

Figure 3.6: Velocity profiles along the (in red) x- and (in blue) y-directions at the center of the aneurysm sac on the central z-plane at four different times: (from left to right) 0.16, 0.27, 0.51 and 0.61 s from the start of the fourth cycle, and (top to bottom) decreasing resolutions in the lattice Boltzmann simulations. Velocity profiles obtained from the LBM simulation are shown with red and blue plain lines while black plain lines with error bars (corresponding to the 99.7% confidence interval) represent data obtained from PIV measurements.

Patient-specific aneurysm model

The last part of the validation was carried out in a patient-specific aneurysm model enabling a clearly more realistic flow scenario. The obtained velocity fields (both numerical and experimental) on three perpendicular planes cutting through the main aneurysm sac are shown in Figure 3.7. It must be noted that both PIV and PC-MRI measurements were conducted here (as opposed to the previous configuration where only PIV measurements were made).

Similar to the idealized test-case, a vortex forms within the sac aligning along the luminal surface and forming a stagnation zone at the center. Due to the helical vessel anatomy proximal to the aneurysm as well as the different ostium size, this vortex appears less stable. Regarding the qualitative comparison of the three independent methods of flow acquisition one can notice that the overall flow structure is captured by all approaches. The entering flow

jet of the simulation appears to be slightly narrower and contains accordingly higher velocity values compared to the experimental techniques. A look at the convergence indicator in the simulations and the flow field evolution over time showed that this configuration results in an unsteady flow although the inlet velocity is not pulsatile. This numerical observation was also confirmed by studying PIV instantaneous velocity fields. As such the data averaging procedure in time, i.e. sampling frequency and time interval, can have non-negligible effect on out-coming velocity fields from both experiments and numerical simulations. The third column in Figure 3.7, representing the instantaneous fields from the LBM simulation are included to point out the unsteady nature of the flow. It must be noted that due to the computational costs and large sizes of associated files, an interval of 0.25 s and sampling frequency of 400 Hz were used to get the average velocity fields for the simulation while as noted earlier, for the PIV the data acquisition was operated at a frequency of 5 Hz and spanned 100 s. For the PC-MRI results on the other hand, the final velocity fields are the average of six snapshots taken at a repetition/echo time of 6.9/3.586 ms. These differences in the averaging process stemming from limitations of each one of these approaches can explain, to a great extent, the discrepancies observed in Figure 3.7. In practice, the low data sampling frequency in PIV and PC-MRI measurements operates as a low-pass filter while the limited sampling interval of the simulation is equivalent to a high-pass filter. This in turn can explain the thicker and smoother shear layers observed in the former two. The subsequent

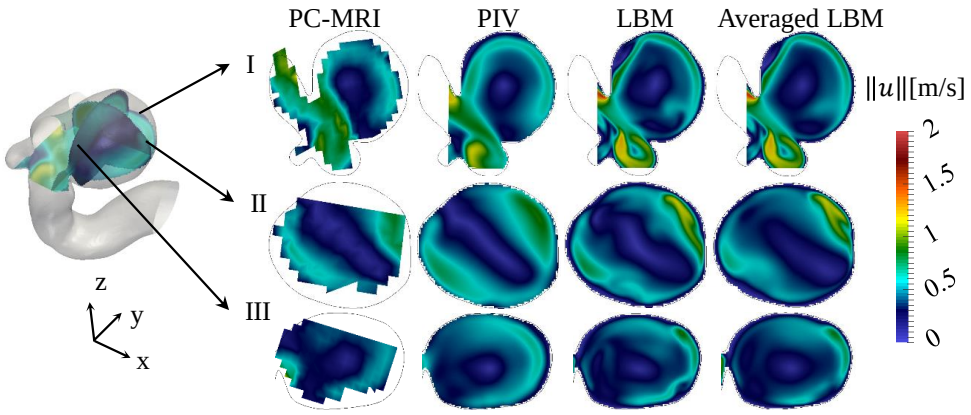

Figure 3.7: From left to right: Qualitative comparison of the velocity fields acquired using PC-MRI (1st column), stereoscopic PIV (2nd column), instantaneous (3rd column) and time-averaged LBM (last column) simulation in the aneurysm sac on three different planes, i.e. from top to bottom: planes I, II and III.

quantification presented in Figure 3.8 provides a better insight in occurring differences and further confirms the previously discussed effect regarding the discrepancies coming from data acquisition. Here, velocity magnitudes are shown along three orthogonal lines through the aneurysm. Overall, the courses of all approaches are in a good agreement and the values show no strong deviations from each other. It must be noted that error bars in Figure 3.8 only represent the 99.7% confidence interval. The simulation results fall within the 99.7% confidence interval at all points.

Matching coordinates and positions of the corresponding velocity fields, together with possible distortions in space resulting from the different experimental procedures, constitute also a major challenge for this comparison; it certainly explains to some extent the observed discrepancy. This effect is particularly visible on the line along the y-axis in Figure 3.8. While the velocity profiles from the simulation tend towards zero near the aneurysm sac walls, PIV results do not show such a clear behavior. Interestingly, the agreement between all methods is excellent for plane III (see Figure 3.8, right), while larger discrepancies are noticeable in the other two (e.g., smoother courses of the measurement compared to the simulation). Overall, while a good qualitative agreement between the three different approaches can be

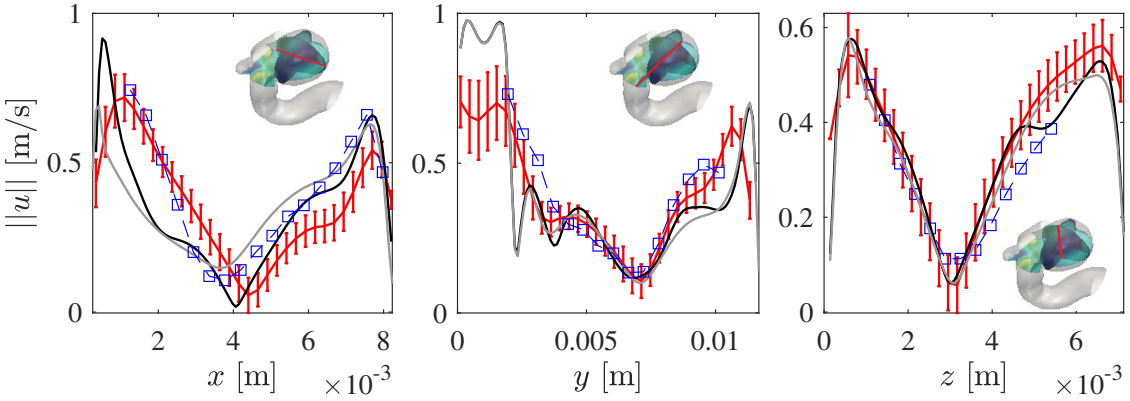

Figure 3.8: Comparison of velocity magnitude profiles along three lines in the aneurysm sac as obtained from PIV (red plain lines with error bars corresponding to one standard deviation), PC-MRI (blue dashed lines with square symbols), instantaneous LB velocity field (black plain lines) and time-averaged (over 0.25 s) LB velocity field (grey plain lines).

observed, non-negligible discrepancies persist. In-depth analysis of the results showed that the unsteady nature of the configuration, along with the different data acquisition modes (i.e. frequency and time-span of velocity field averaging process) affect the final velocity fields. This effect was illustrated by comparing instantaneous and averaged velocity fields in the simulation. The distortions and manufacturing artifacts in the final aneurysm geometry can also contribute to these discrepancies. Further reasons are discussed in Section 3.1.4.

Under-resolved simulation of the patient-specific configuration

Finally, to showcase the ability of the collision operator to deal with under-resolved cases, and provide a more in-depth analysis, the patient-specific configuration was also modeled using a coarse grid. The time-averaged velocity fields obtained using the high- and the low-resolution LBM simulation are shown in Figure 3.9. The orthogonal planes reveal that the predicted flow structures, while admitting discrepancies, agree very well. The quantitative comparison of both simulations leads to a domain-averaged similarity of 0.8294, 0.8765 and 0.8359 for planes I, II and III, respectively. This similarity index on each plane is computed

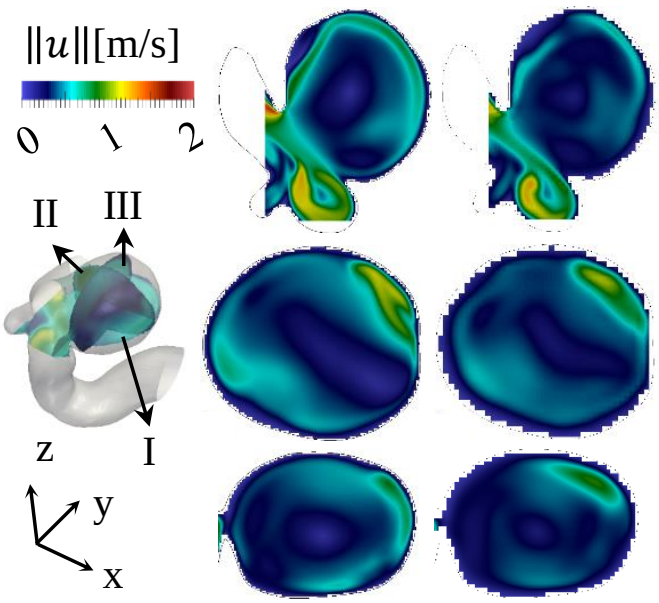

Figure 3.9: Qualitative comparison of the velocity fields in the aneurysm sac on three different planes, i.e. from top to bottom: planes I, II and III, as obtained from the high-resolution (left) and low-resolution (right) simulation.

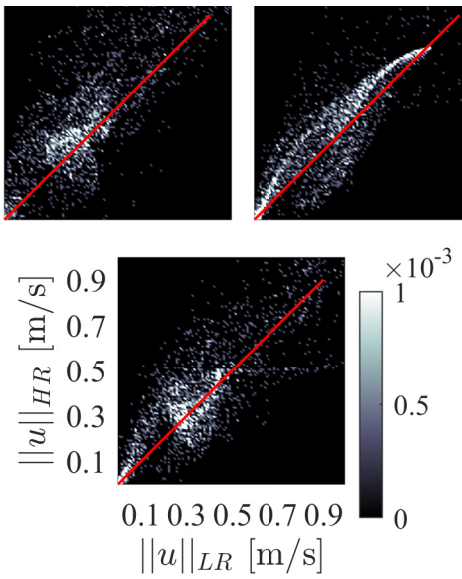

Figure 3.10: Quantitative comparison of the velocity magnitude distribution in the high- and low-resolution simulations on planes I (top left), II (top right) and III (bottom). The color bar represents the normalized (via the total number of sampled points) number of grid-points with the corresponding velocities in the low-resolution (x-axis) and high-resolution (y-axis) simulation.

as the average similarity index over all discrete points on the plane [2]:

$$\mathrm{SI} = \left(1 + \frac{\boldsymbol{u}_{\mathrm{HR}} \cdot \boldsymbol{u}_{\mathrm{LR}}}{||\boldsymbol{u}_{\mathrm{HR}}||||\boldsymbol{u}_{\mathrm{LR}}||}\right) \cdot \left(1 - |\frac{||\boldsymbol{u}_{\mathrm{HR}}||}{||\boldsymbol{u}_{\mathrm{HR}}||_{\max}} - \frac{||\boldsymbol{u}_{\mathrm{LR}}||}{||\boldsymbol{u}_{\mathrm{LR}}||_{\max}}|\right), \tag{3.1}$$

where $\boldsymbol{u}_{\mathrm{HR}}$ and $\boldsymbol{u}_{\mathrm{LR}}$ are the velocity vectors from the high- and low-resolution simulations, respectively. The deviations are further illustrated in Figure 3.10, where the low-resolution velocity magnitudes are plotted against the high-resolution ones on the three considered planes. The normalized frequency of the similarity index on all three planes is shown in Figure 3.11. Despite these minor differences with respect to the velocity distribution, it is

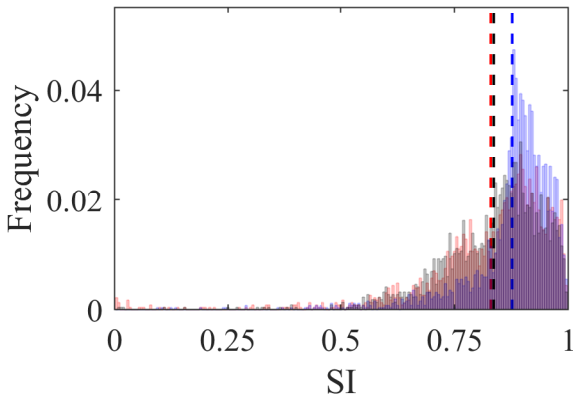

Figure 3.11: Histograms displaying the normalized frequency of the SI on planes I (blue), II (red) and III (black). The corresponding overall SIs are shown using dashed lines of the same color.

important to mention that the low-resolution simulation reduced the number of grid-points by a factor of eight, and – given the acoustic scaling – the number of time-steps needed for convergence by a factor of two. This in turn reduced the computation time by a factor of 14 on the same machine and using the same number of processing units.

3.1.4 Discussion

With an improved linkage of medical and engineering disciplines as well as increasing computational resources new potentials in interdisciplinary research are revealed. Specifically, the challenging question of rupture risk assessment for intracranial aneurysm remains unanswered until now; however, more and more insights into patient-specific hemodynamics become accessible [118]. On the other hand, insufficient data processing, the absence of reliable boundary conditions and mostly long simulation times lead to a reduced translation into clinical practice [119].

To highlight the potential of image-based blood flow simulations and demonstrate their reliability with respect to flow prediction, a multimodal validation study was carried out. This included different configurations, flow scenarios, measurement methodologies and simulation settings, respectively.

The first part of the validation relied on flow assessments under well-controlled conditions. A brief comparative study showed that the CHMRT collision operator with a full extension of the EDF performed much better than the classical SRT model. To further validate the solver an idealized model of an intracranial aneurysm was created leading to the development of an organized flow field. The qualitative and quantitative comparison of both independent techniques (LBM versus PIV) showed good agreement. Due to the unsteady inflow, minor fluctuations occurred throughout the cardiac cycle, especially near peak systole. Still, both simulation and measurement were in very good agreement during the whole period.

In the second part of this study, complexity was increased by considering a patient-specific anatomy. Although unsteady phenomena occurred at peak-systolic inflow conditions, flow predictions by simulation and measurement were comparable. Beside the validation using PIV, PC-MRI acquisitions were carried out. Here, minor differences especially in high-velocity regions close to the aneurysmal lumen were present, which could be a result of vessel wall compliance [120]. However, taking into account all underlying differences with respect to temporal and spatial resolution as well as the uncertainties associated to the measurement procedures, the validation of the LBM simulation was successfully conducted.

Apart from the validation purpose, additional simulations with low spatial resolutions were performed. The comparison of low- and high-resolution LBM computations showed that similar velocity fields were calculated, although only 1/14 of the simulation time was required. Hence, depending on the clinical research question and the desired accuracy of the hemodynamic description the low-resolution approach, made possible by the CHMRT collision operator, can be a promising development direction, especially given that the computational overhead associated to the change of collision operator is very minor [121].

Beside the presented findings, it is important to mention that this study has several limitations: First, the number of cases considered is relatively small for an extensive validation study. Only two idealized and one patient-specific geometries were selected. However, it is important to point out that intracranial aneurysms show a high variability regarding size (small versus giant), location (lateral versus terminal), morphology (spherical versus complex). Consequently, this can lead to increased challenges for the underlying numerical schemes. Nevertheless, multiple numerical and experimental processing steps are involved. Second, precise qualitative and quantitative comparisons are only feasible, when identical conditions are warranted. However, due to the manufacturing of the phantom models for the in-vitro investigations or the subsequent registrations processes, minor misalignment between the ideal CAD geometries and the silicone models can occur.

Third, blood was considered as an incompressible Newtonian fluid in the simulations. There is an ongoing debate about the necessity of a more detailed consideration of this suspension [122, 123, 124]. Many studies claim that blood rheology has a secondary impact compared to primary factors such as segmentation or boundary conditions [125, 89]. This point will be checked later on in this document. Finally, although PC-MRI is a technique to obtain flow data in-vivo, within this study in-vitro measurements in a silicone phantom were carried out. Therefore, the MR sequence might lead to slightly different results when applied to a real aneurysm.

3.1.5 Conclusions

This validation study comprising multimodal measurement techniques and various experimental scenarios demonstrates a number of points. Chief among them is the advantage of using multimodal approaches for a detailed validation of results in this area. It was readily shown that experimental measurements using both PIV and PC-MRI were prone to non-negligible sources of uncertainty and needed to be considered with care. Furthermore it was proven that the presented LBM solver relying on a CHMRT collision operator is able to generate reliable and valid simulation results. These findings are in line with observations made in the LBM literature on the effect of such models in eliminating a number of numerical artefacts associated to the classical SRT collision operator with second-order EDF while maintaining a low computational cost low – around 0.4 Mega lattice updates per second (MLUPS) per processor. As shown in [53] the added cost of the modified collision operator is negligible. Furthermore, the wider stability domain and enhanced spectral properties of the collision model (as compared to the SRT) allowed for simulations relying on lower resolutions (not stable with the SRT) yielding comparable numerical predictions with an extensive reduction of computational load (grid-points and time-steps). Given the difficulties of applying explicit sub-grid model-based large eddy simulations (LES) to pulsatile flows in complex geometries, tools and numerical formulations allowing for model-free under-resolved simulations – tantamount to implicit LES – can be an interesting path towards a rapid evaluation of flow parameters in complex biomedical settings.

3.2 CFD challenge in a giant aneurysm

3.2.1 Introduction

Numerous individual studies have undertaken the validation of image-based CFD predictions by comparing them against meticulous in vitro measurements [126, 127] or available in vivo data [128, 129]. Despite the wealth of these individual validations, there has been a relative scarcity of studies in the biofluids literature that systematically evaluate the sensitivity of CFD predictions to different solvers or research groups. Notable exceptions include initiatives like the Virtual Intracranial Stent Challenges [130] and the FDA nozzle benchmark [131]. These efforts, such as the CFD challenge proposed to document the variability among different CFD groups, contribute significantly to the understanding of the robustness and reliability of diverse CFD approaches. The case presented in Ref. [5], involving a giant aneurysm, was specifically chosen for such evaluations. Note that, being organized by a US group, non-USI units have been specified for this benchmark.

3.2.2 Numerical setting

The configuration and the inlet flow waveform are illustrated in Figure 3.12. The flow waveform exhibits a period of 0.99 s. The blood was modeled with Newtonian behavior, characterized by a constant viscosity and density of 0.04 Poise and 1.0 g/cm^3, respectively. The nominal inlet diameter D was set at 5.58 mm, corresponding to a peak flow rate of

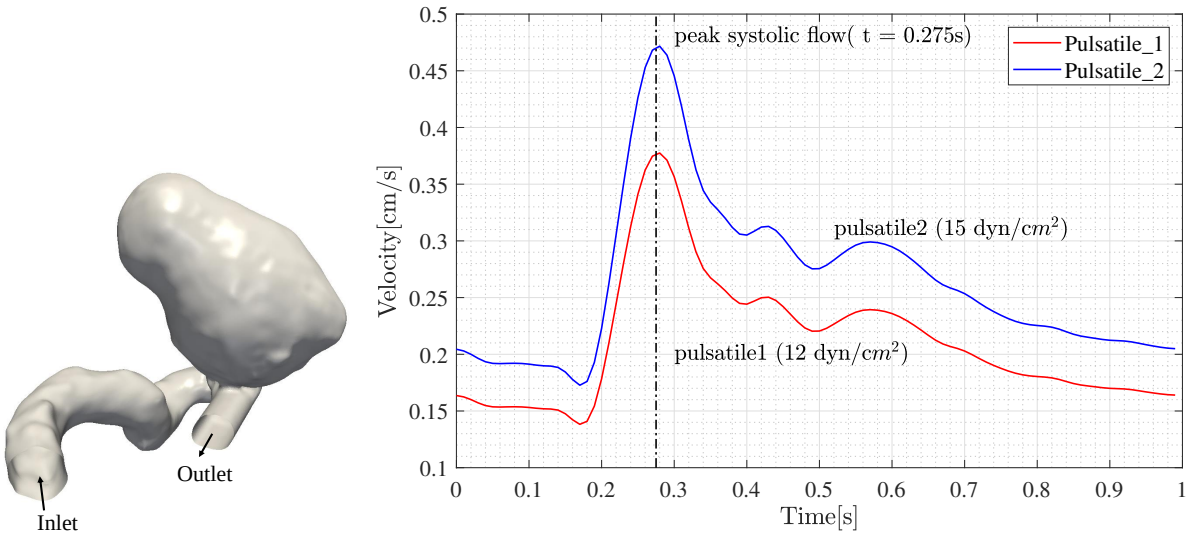

(a) (b)

Figure 3.12: (a) Phase I CFD model geometry. (b) Phase I pulsatile inlet flow waveforms.

11.42 mL/s. Pulsatile velocity and constant pressure were applied as the boundary conditions for the inlet and outlet, respectively. A non-slip boundary condition was implemented at the walls. The simulations were conducted over three cycles, and the results were sampled from the last cycle.

3.2.3 Results

3.2.3.1 Mesh independence analysis

This study examined three different resolutions ($334 \times 123 \times 18$, $400 \times 146 \times 220$, $498 \times 181 \times 274$). The velocity profiles, as depicted in Figure 3.13, show satisfactory agreement with the reference results (from code Nektar). Notably, the lowest resolution result deviates at the position of 4 mm, while the two higher resolutions exhibit considerable overlap. Considering additionally computational cost, the medium resolution ($400 \times 146 \times 220$) was selected for conducting the further numerical simulations.

3.2.3.2 Effect of the inlet length

To mitigate the potential impact of the inlet condition, the inlet was extended to 0.03(5D), 0.08(14D), or 0.13 m(23D) along the normal vector of the inlet surface. As illustrated in Figure 3.14, the length of the inlet significantly influences the numerical outcomes. The velocity from the shortest extension deviates considerably from the Nektar solution, while the other two exhibit nearly identical results. Considering additionally computational efficiency, the medium extension was adopted for further simulations.

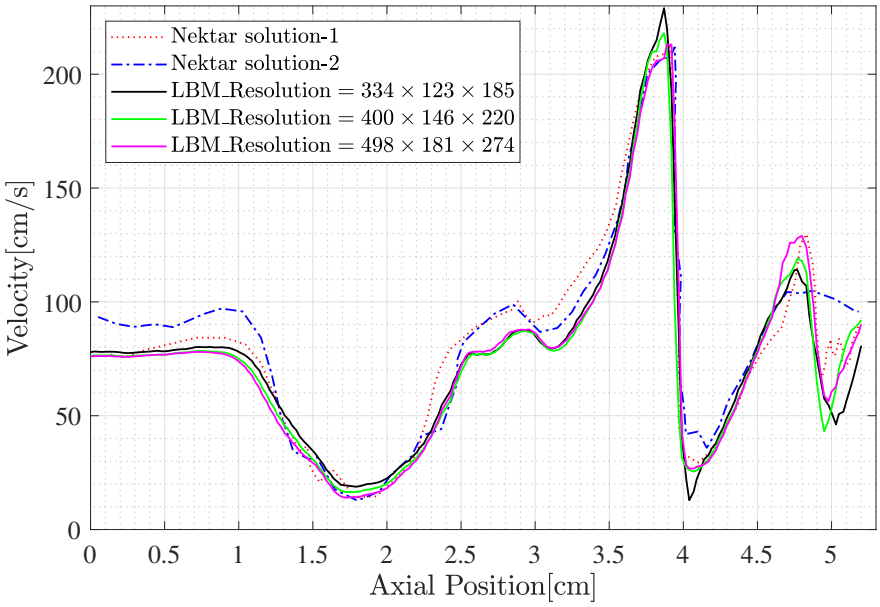

Figure 3.13: Phase I centerline velocities for "pulsatile2" flow at three resolutions. The dotted lines represent the two Nektar solutions [4].

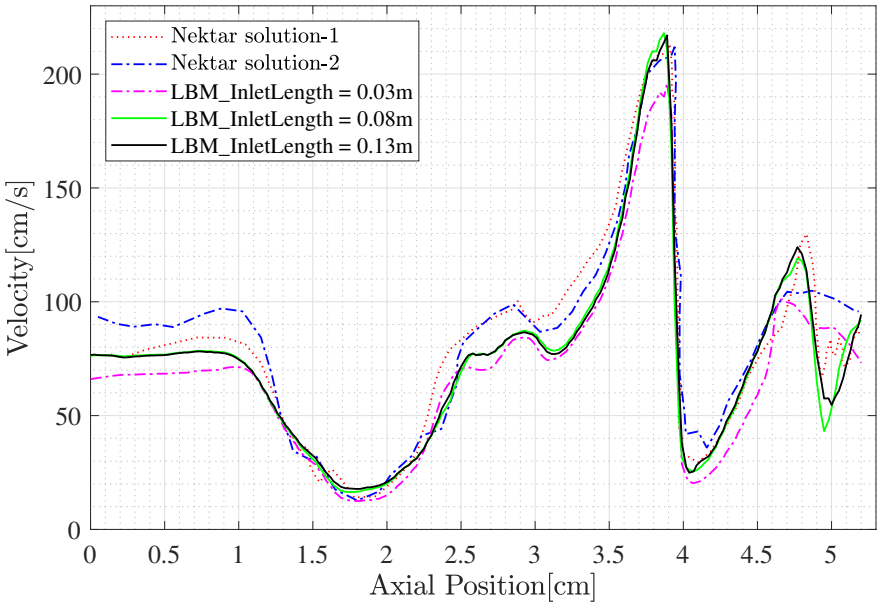

Figure 3.14: Phase I centerline velocities for "pulsatile2" flow. The red and blue lines represent the two Nektar solutions [4]. The magenta, green, and black lines show the LBM results for different inlet lengths 0.03 m, 0.08 m, 0.13 m.

3.2.3.3 Velocity comparision

Figure 3.15 depicts the peak systolic velocities for the "pulsatile2" case. Among the groups participating in the original benchmark, a strong variability is observed regarding the flow

patterns in the aneurysm sac. Among the solutions (A, Q, R, U, W, X), strong flow instabilities are apparent, while all remaining solutions exhibit smoother isosurfaces. The solutions (L, N, Z) are very comparable to those obtained by LBM in the present study.

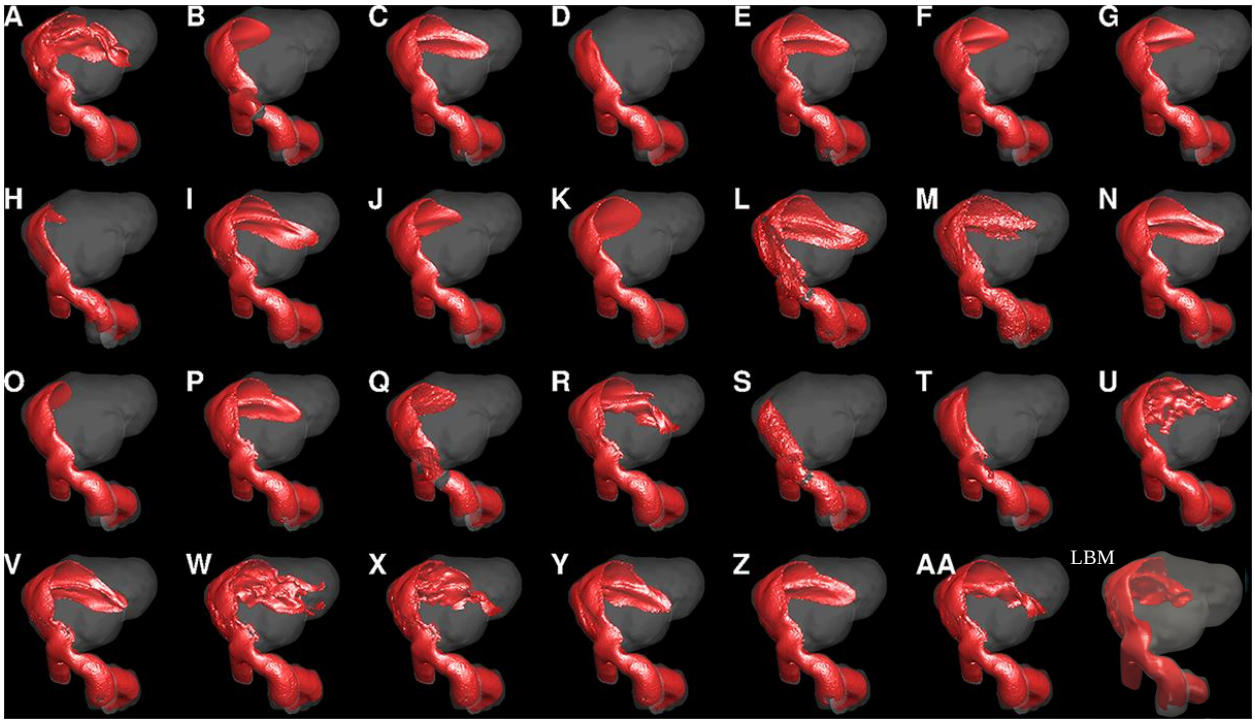

Figure 3.15: Isosurfaces of velocity magnitude at 0.5 m/s for Phase I, "pulsatile2" case at peak systole (PK2). The result from this study (LBM) is shown in the bottom right corner. All remaining results are from reference [5].

Additionally, Figure 3.16 shows the centerline velocities for the "pulsatile2" case at peak systole (PK) and for cycle-averaged flow (AV). Our numerical results are in good agreement with the Nektar (reference) solutions. Noticeable differences in average velocity are only found near the outlet, showing a possible impact of boundary conditions.

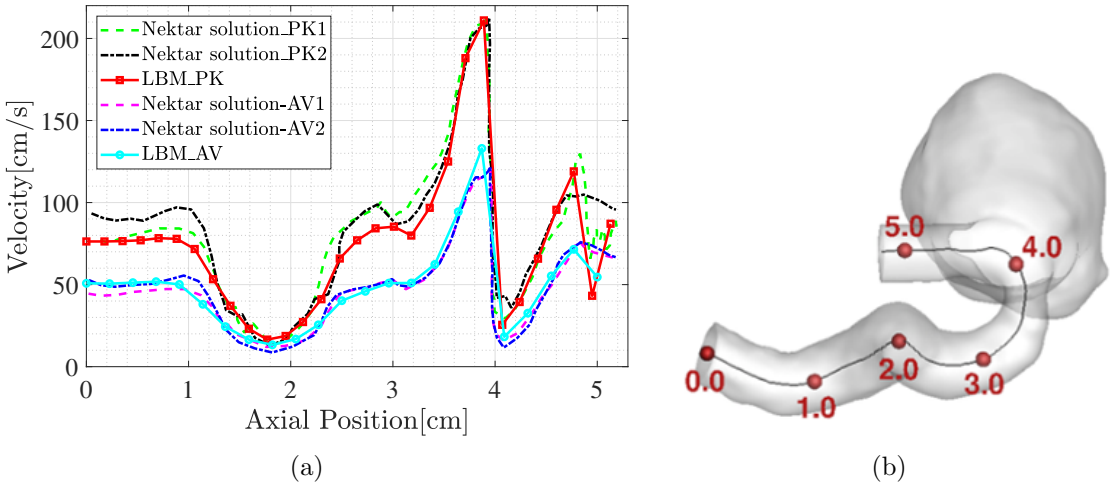

(a) (b)

Figure 3.16: (a) Velocity distribution along the centerline for "pulsatile2" case at peak systole (PK) or for cycle-averaged velocity magnitudes (AV). (b) represents the centerline with corresponding positions [5].

3.3 FDA nozzle benchmark

Part of this section has been published as:
Feng Huang, Romain Noël, Philipp Berg, and Seyed Ali Hosseini. Simulation of the FDA nozzle benchmark: A lattice Boltzmann study. Computer Methods and Programs in Biomedicine, 221:106863, 2022.

3.3.1 Introduction

For the classical LBM, computational costs are still often prohibitive at high Reynolds numbers, for instance in aortic aneurysms. That is mainly due to the fact that the standard LBM using a collision operator with a single parameter (SRT) EDF suffers from shortcomings such as limited stability and lack of Galilean invariance [48, 50, 132].

Thus, many modifications have been proposed to extend the accuracy and stability of the LBM, most notably, through more advanced collision operators, e.g. the entropic formulation [64, 133], the MRT [134], centered or cascaded [61], the Cumulant method [135], or the regularized LBM [136]. Furthermore, the inconsistency in the shear components can be readily overcome by using higher order expansions in the EDF [132]. The development of more consistent and robust schemes has also opened the door to so-called under-resolved direct numerical simulations [48, 137]. A number of studies have shown that such simulations can match LES with explicit sub-grid scale closures in terms of accuracy in many configurations, as demonstrated most recently in [138] for homogeneous isotropic turbulence. In the present work, we will further explore that avenue in the context of biological flows, through a well-established benchmark.

The need for reliable, reproducible benchmarks confronted with experiments is urging in

bio-medical applications where many variables may affect the results: temperature, in-vivo vs. ex-vivo vs. in-vitro, biological species, etc. The US Food and Drug Administration (FDA), conscious of this reality, suggested a series of challenging benchmarks. The idealized medical nozzle device benchmark has been used by several laboratories to conduct PIV measurements. Those measurements provided reference standards to test the accuracy, stability and efficacy for numerical solvers or alternative experimental measurement techniques [139]. Experimental data sets have been provided by independent laboratories at different Reynolds numbers Re = 500, 2000, 3500, 5000, and 6500, computed using the diameter of the throat (see later Figure 3.17). These values of Reynolds numbers are typically encountered in medical devices involving flow recirculations, contractions, or expansions. This range of Re covers very different flow regimes going from laminar (for Re = 500 and 2000) to transitional (for Re = 3500 and 5000) to low-level turbulence (for Re = 6500). The corresponding PIV experiments have been carried out completely independently by three different groups. It must be kept in mind that large inter-laboratory discrepancies have been observed, in particular regarding the jet breakdown location for transitional and turbulent flows. Conversely, a very good agreement was observed for fully laminar flows [131].

Many numerical studies of this benchmark nozzle have been performed over the years, employing various numerical schemes ranging from Finite Element Method (FEM) [140, 141] to Finite Volume Method (FVM) [142, 143], as well as a few using LBM [31, 144]. Table 3.1 summarizes the published numerical studies of the FDA benchmark nozzle with the associated Reynolds numbers, numerical methods and turbulence models employed. While many studies performed Direct Numerical Simulation (DNS) for the lower Reynolds numbers, most simulations in the turbulent regime were conducted using turbulence models like Unsteady Reynolds-Averaged Navier-Stokes (URANS) [145, 146] or LES [147, 143, 148].

Table 3.1: Summary of numerical studies associated to the FDA benchmark nozzle.

Study at Re	500	2000	3500	5000	6500	Numerical method	Sub-grid model
Sanchez Abad et al. [149]	✓	✓	✓	✓		Spectral elements (Nek5000)	None
Fehn et al. [150]	✓	✓	✓	✓	✓	High-order	None
Bergersen et al. [140]	✓		✓		✓	FEM (Oasis)	None
Pewowaruk et al. [145]	✓		✓		✓	FVM (Converge v2.4)	None
Stewart et al. [131]	✓	✓	✓	✓	✓	various	various
Zmijanovic et al. [142]			✓			FVM (YALES2BIO)	σ-model
Manchester et al. [147]		✓				FVM (OpenFOAM)	Wale
Bhushan et al. [146]	✓		✓		✓	FVM (ANSYS Fluent)	URANS
Janiga [143]					✓	FVM (ANSYS Fluent)	Smagorinsky
Chabannes et al. [141]	✓	✓	✓			FEM (Feel++)	None
White et al. [144]	✓					regularized LBM (Palabos)	None
Jain [31]		✓	✓			MRT-LBM (Musubi)	None
Present work	✓		✓		✓	central Hermite MRT-LBM	None

Few studies simulated the FDA nozzle benchmark using LBM; none of those has covered all experimental conditions, more specifically the higher Reynolds numbers. White and Chong [144] performed LBM simulations at low Reynolds numbers (50 – 500) and studied

the suitability of different lattice types. More recently, Jain [31] studied the FDA nozzle at Re = 2000 and 3500 with a simple LBM scheme (raw moments MRT collision operator with second order EDF and D3Q19 lattice) focusing on fully-resolved simulations. Results were shown for the average axial velocity, pressure profiles, and shear stress in different planes. In the present study, we consider a wider range of Reynolds number, covering all flow regimes. The computations are done with an advanced LBM model relying on a central Hermite collision operator with a full expansion of the discrete equilibrium, implemented in the in-house LBM solver ALBORZ [53, 56, 115, 151]. The accuracy of this numerical model is assessed in under-resolved direct numerical simulations at different resolutions, akin to filtered simulations. A comprehensive comparison to experimental data covering all relevant fields is presented.

3.3.2 Numerical simulations

Cases description A cross-sectional view of the idealized medical device, subject of the FDA nozzle benchmark is shown in Figure 3.17. The geometry is composed of an axisymmet-

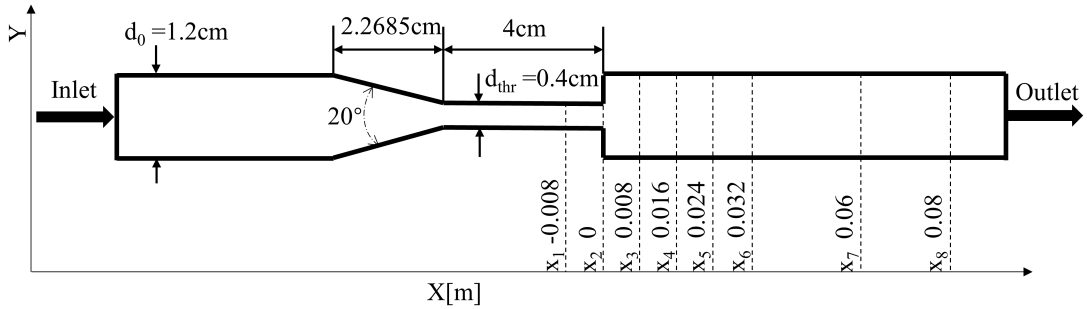

Figure 3.17: Schematic representation of the FDA nozzle with all dimensions.

ric nozzle with a convergent section on the flow inlet extremity, a constant throat section in the middle and a sudden expansion section toward the end. To eliminate a possible numerical effect of inlet and outlet boundary conditions, the nozzle has been extended by 0.052 m and 0.02 m at both ends, respectively. The final length of the nozzle is 0.24 m. To validate the numerical results, data are collected from both the horizontal center-line and eight distinct planes located at different coordinates along the horizontal x-axis. Figure 3.17 shows the locations of these planes. The simulations are run over a total period of time covering 300 t_c, where t_c is the flow-through period defined as,

$$t_c = \frac{L_c}{u_c}, \tag{3.2}$$

where the characteristic speed u_c and length L_c are set to the velocity in the throat u_{thr} and to the length of the throat section, respectively. Only data from the second half, i.e. $150 - 300$ t_c is used for the time-averaging process to get average flow fields. The PIV data

used for validation and the 3-D model geometry are available from the FDA official website[1].

Flow conditions Following experimental settings and benchmark requirements, the fluid was considered to be Newtonian, with a density of $1056\,\mathrm{kg/m^3}$ and a dynamic viscosity of $3.5\ \mathrm{mPa \cdot s}$. The Reynolds number is computed as:

$$\mathrm{Re} = \mathrm{Re}_{\mathrm{thr}} = \frac{\rho \overline{u}_{\mathrm{thr}} d_{\mathrm{thr}}}{\mu}, \tag{3.3}$$

where d_{thr} is the throat diameter and $\overline{u}_{\mathrm{thr}}$ is defined as:

$$\overline{u}_{\mathrm{thr}} = \left(\frac{d_0}{d_{\mathrm{thr}}}\right)^2 \overline{u}_0. \tag{3.4}$$

The average inlet velocity $\overline{u}_0$ is obtained by dividing the volume flow rate by the inlet surface area $S_0 = \pi d_0^2/4$. To cover all flow regimes, the present study considers $\mathrm{Re} = 500$, 3500, and 6500. Based on critical pipe Reynolds numbers, the first would fall in the laminar regime, the second in the transitional, and the third in the low-level turbulent regime, respectively.

Simulation details The inlet boundary condition for the velocity is prescribed in the form of a laminar parabolic profile:

$$u(r) = 2\overline{u}_0 \left(1 - 4\frac{r^2}{d_0^2}\right). \tag{3.5}$$

Constant pressure boundary conditions are implemented at the outlet while no-slip boundary conditions are employed along the walls. The no-slip conditions are enforced with the curved treatment of the bounce-back method [82] while the outflow constant pressure is applied using the non-equilibrium extrapolation approach [152].

The computational domain is tridimensional ($D = 3$) and has a volume of $0.012 \times 0.012 \times 0.24\,\mathrm{m^3}$. Simulations were conducted with different grid resolutions, δr, listed in Table 3.2. Four different resolutions will be considered in the study. The respective time-step sizes, δt, are defined by fixing the maximum predicted convective Courant–Friedrichs–Lewy (CFL) number in the domain:

$$\mathrm{CFL} = \frac{2\overline{u}_{\mathrm{thr}}}{\delta r/\delta t}, \tag{3.6}$$

in turn leading to:

$$\delta t = \frac{\rho d_{\mathrm{thr}} \delta r \mathrm{CFL}}{2\mu \mathrm{Re}_{\mathrm{thr}}}. \tag{3.7}$$

For the analysis of the turbulent statistics, the velocity is decomposed into a mean and a fluctuating part as:

$$\boldsymbol{u}(\boldsymbol{x}, t) = \overline{\boldsymbol{u}}(\boldsymbol{x}) + \boldsymbol{u'}(\boldsymbol{x}, t), \tag{3.8}$$

[1] `https://ncihub.org/wiki/FDA_CFD`

Table 3.2: Spatial and temporal resolutions of simulations.

	Re	δr [$\times 10^{-4}$m]	δt [$\times 10^{-6}$s]
R1	500	2.3	49.03
R2	500	1.725	36.75
R3	500	1.15	24.5
R1	3500	2.3	9.86
R2	3500	1.725	7.38
R3	3500	1.15	4.93
R1	6500	2.3	5.31
R2	6500	1.725	3.98
R3	6500	1.15	2.65
R4	6500	0.776	1.7

where the mean part $\overline{\boldsymbol{u}}$ is defined by:

$$\overline{\boldsymbol{u}}(\boldsymbol{x}) = \frac{1}{\Delta t}\int_{t_0}^{t_0+\Delta t} \boldsymbol{u}(\boldsymbol{x},t)dt, \tag{3.9}$$

t_0 indicates the start of averaging and Δt the period over which it is done. Averaging the convective momentum flux term in the NSE using this decomposition, one gets:

$$\overline{(u_\alpha + u'_\alpha)(u_\beta + u'_\beta)} = \overline{u_\alpha u_\beta} + \overline{u'_\alpha u'_\beta}, \tag{3.10}$$

The last term of this equation appears in the Reynolds stress tensor, defined as:

$$\Pi'_{\alpha\beta} = \rho\overline{u'_\alpha u'_\beta}, \tag{3.11}$$

where $\boldsymbol{u'}(\boldsymbol{x},t)$ and ρ indicate velocity fluctuations and fluid density, respectively. The Reynolds stress tensor is symmetrical and consists of three normal stress and six shear stress components. The normal stress can be calculated as $\rho\overline{u'_\alpha u'_\alpha}$ where the term $\overline{u'_\alpha u'_\alpha}$ indicates the time-averaged product of normal velocity fluctuations. Finally, the viscous shear stress σ is calculated, in this study, as below:

$$\sigma_{\alpha\beta} = \frac{1}{2}\rho\nu\left(\partial_\beta u_\alpha + \partial_\alpha u_\beta\right). \tag{3.12}$$

3.3.3 Results

Numerical results are compared to experimental data from three independent laboratories, presented in the form of five different data-sets [139], i.e. three different measurements from the first laboratory, and one each for the second and third laboratories. Throughout this section the three independent sets of measurements from the first laboratory are shown with

diamonds, circular, and square markers. Data from the second and third laboratories are represented by asterisks and upward-pointing triangular markers, respectively.

3.3.3.1 Laminar flow, Re = 500

At Re = 500 (inlet Reynolds number of 167), the flow regime is expected and has been observed to be fully laminar from both PIV and numerical results, meaning that no jet break-down is observed after the sudden expansion (see Figure 3.18(a)).

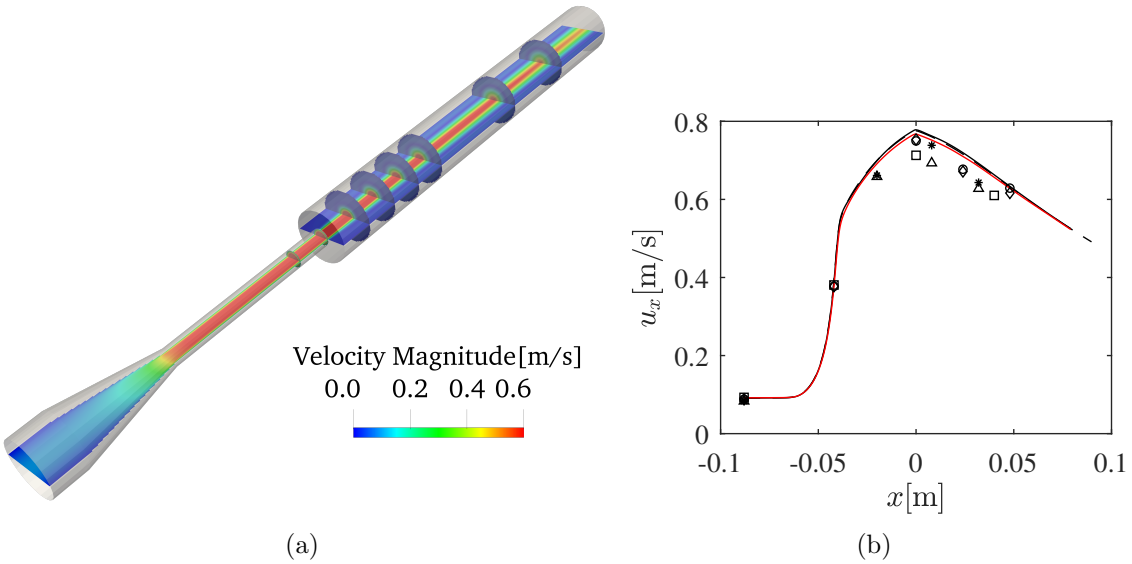

(a) (b)

Figure 3.18: Results for Re = 500. (a) Snapshot of the steady velocity field as obtained from R2 simulations at time $t = 2.4$ s. (b) Comparison of mean axial velocity between LBM results and PIV experiments along the center-line of the nozzle. The results from R1, R2, and R3 are indicated by solid black, dashed black and solid red lines respectively.

Axial velocity The results as obtained from R1, R2 and R3 resolutions are compared to experimental data in Figures 3.18(b) and 3.19. First, we look into the time-averaged axial velocity (note that, in this laminar configuration, time-averaged fields are equivalent to the steady fields) along the center-line. All three numerical profiles closely match each other – lying often on top of each other –, indicating that the chosen grid-sizes allow to correctly resolve the flow features.

It can be noted from the axial velocity plot that the flow is constant upstream of the contraction section ($x < -0.063$ m) and accelerates when flowing into the contraction region, reaching a peak value of 0.76 m/s at the entrance of the expansion section, plane X_2 (corresponding to $x = 0$). The flow starts decelerating with an approximately linear rate in the sudden expansion section ($x > 0$) due to the increase in cross-section area. In both Figures 3.18(b) and 3.19, large discrepancies are observed between the different measure-

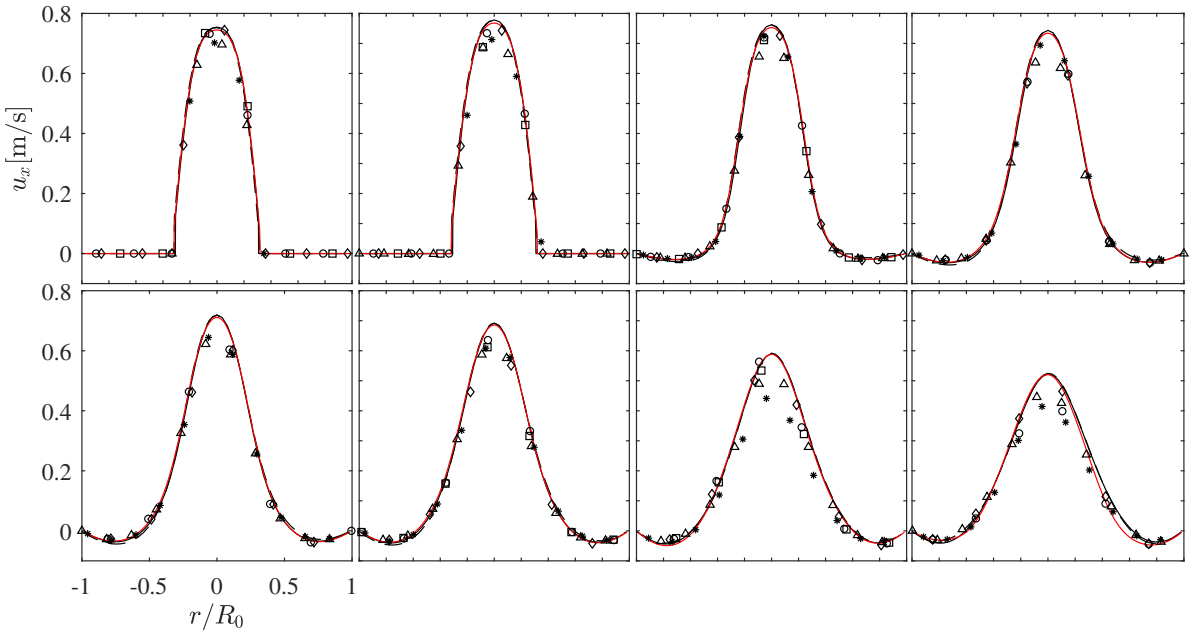

Figure 3.19: Results for Re = 500. Axial velocity profiles compared with PIV experiments at selected cross-sections. The radial distance is normalized by the radius of the nozzle, R_0. The results from R1, R2, and R3 are indicated by solid black, dashed black and solid red lines respectively. Cross-section planes X_1 to X_8 are represented from top left to bottom right.

ments. Stewart et al. [131] reported that the experimental data-sets are strongly affected by normalization errors, which could partly explain the observed variations.

Radial profiles of axial velocity on sampling planes The profiles of the predicted axial velocity are illustrated at eight cross-sections in Figure 3.19. A good quantitative agreement is observed between PIV data and numerical results throughout the nozzle.

However, the peak values of the axial velocity appear to be slightly overestimated after the sudden expansion section. Hariharan et al. [139] reported fluctuations in flow rate during the experiments, which can lead to this difference. Given that discrepancies between experimental and numerical results are at the same level as measurement uncertainties, it can still be concluded that numerical simulations agree well with the experiments for this case.

Viscous shear stress The magnitude of the mean viscous shear stress component σ_{xy} along the same cross-sections is illustrated in Figure 3.20. Overall, numerical viscous shear stresses are in good agreement with the values reported from the PIV measurements. Peak stresses between the central jet and the recirculation zones show a decreasing trend in downstream direction after entering the sudden expansion. The viscous shear stresses are consistently zero along the center-line.

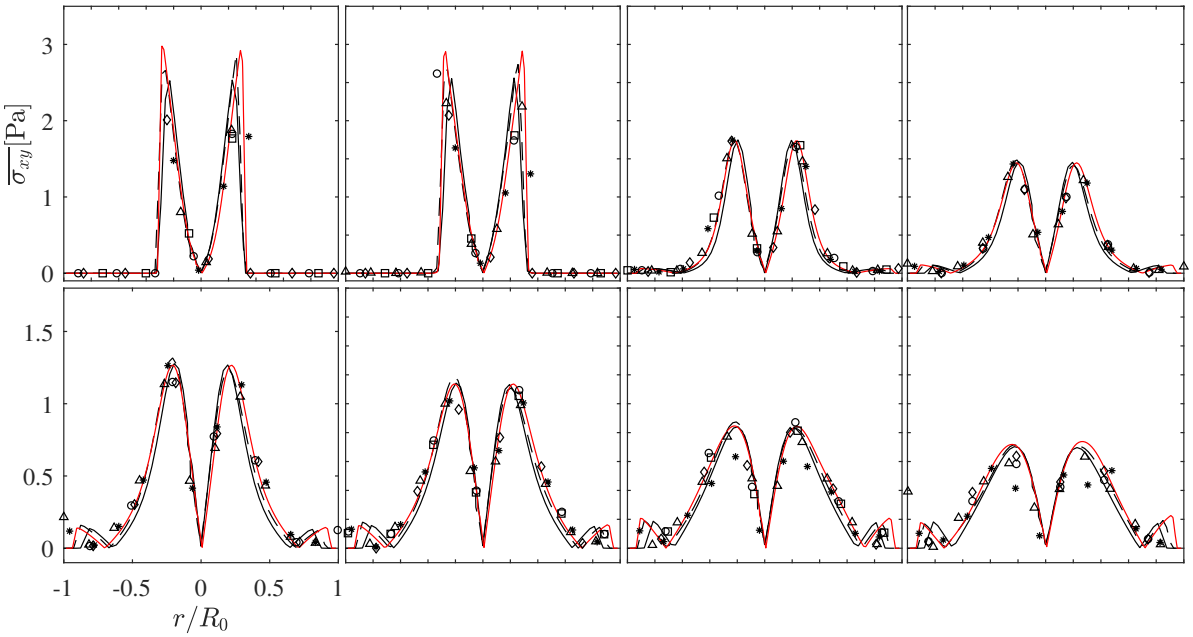

Figure 3.20: Results for Re = 500. Viscous shear stress compared with PIV experiments at selected cross-sections along the center-line. The results from R1, R2, and R3 are indicated by solid black, dashed black and solid red lines respectively. Cross-section planes X_1 to X_8 are represented from top left to bottom right. Note the different vertical scales between the two rows.

3.3.3.2 Transitional flow, Re = 3500

At Re = 3500 (inlet Reynolds number of 1169), the flow regime has been observed to be transitional with a jet breakdown downstream of the sudden expansion region observed both in the PIV experiments and numerical simulations (see Figure 3.21(a)).

Axial velocity Looking at Figure 3.21(b), the axial velocity reaches a peak of 4 m/s on the finest grid (R3) at $x = 0.02$ m, but then decreases afterwards rapidly to 0.5 m/s at $x = 0.06$ m, which indicates jet break-down. The velocity distributions obtained from all three simulations match perfectly up to the smooth contraction zone. In the throat, small discrepancies (of the order of 3% relative differences) are observed in the predicted maximum velocities. Overall, the time-averaged axial velocities along the center-line predicted by LBM simulations match the PIV data very well, particularly so for resolution R3. The differences observed between R1, R2 and R3 are in the same range as the variations found in the measurements.

Radial profiles of axial velocity on sampling planes Figure 3.22 shows axial velocity profiles along the chosen cross-section planes. In contrast to the parabolic profiles found at Re = 500, the axial velocity profiles are now plug-like in the throat section, as expected. Starting at X_4, negative axial velocities appear close to the walls indicating a large, recirculating

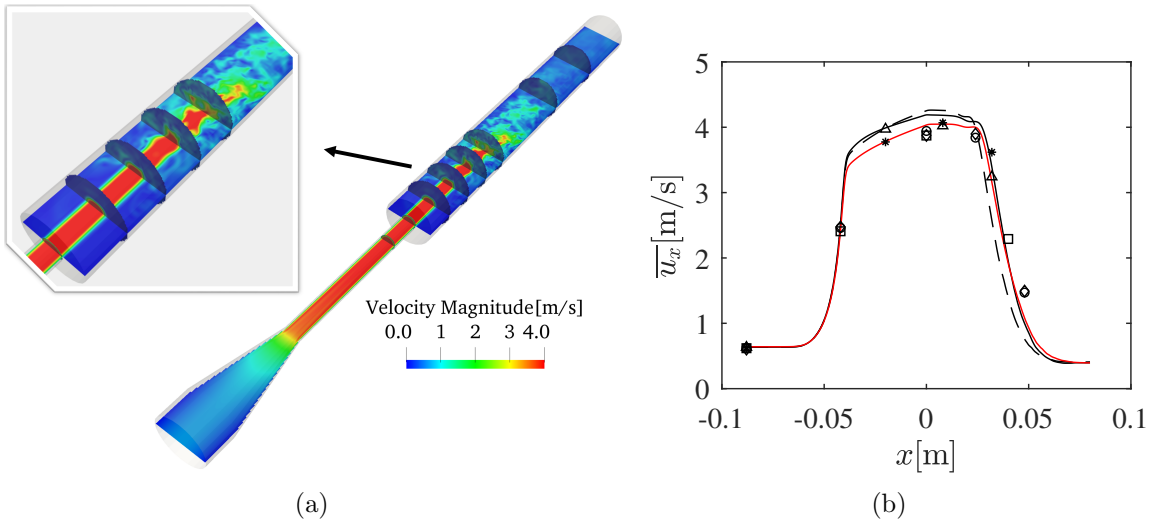

Figure 3.21: Results for Re = 3500. (a) Snapshots of instantaneous velocity field as obtained from R3 simulation at time $t = 4.2$ s. The top-left inlay is a zoom over the sudden expansion. (b) Comparison of mean axial velocity between LBM results and PIV experiments along the center-line of the nozzle. The results from R1, R2 and R3 are indicated by solid black, dashed black and solid red lines, respectively.

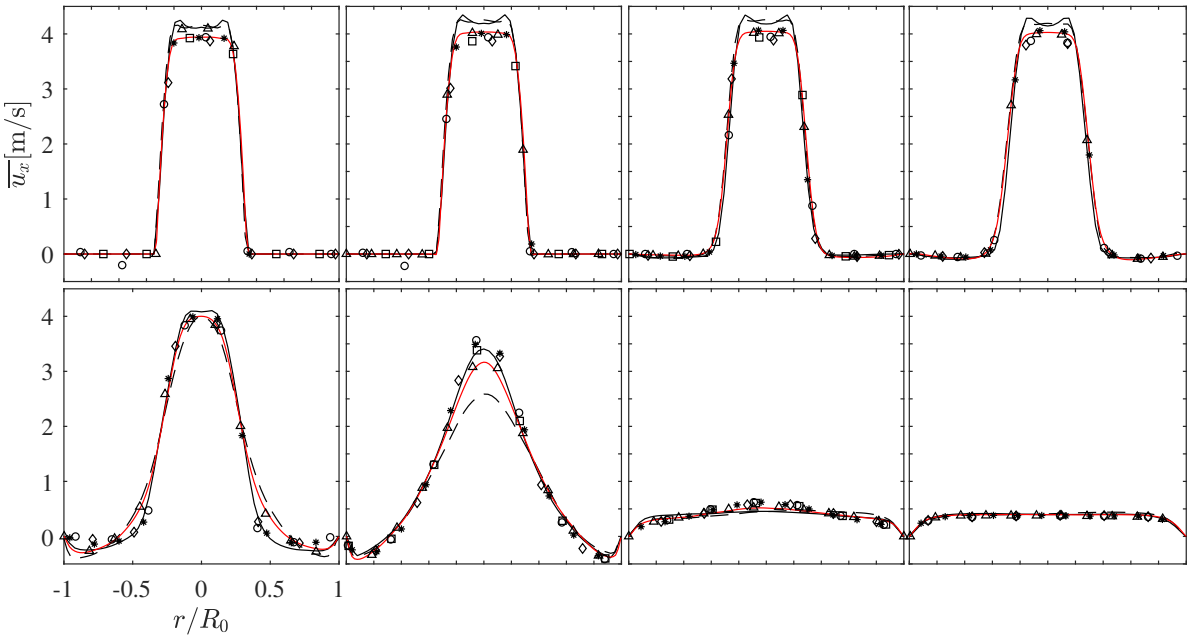

Figure 3.22: Results for Re = 3500. Time-averaged axial velocity profiles compared with PIV experiments at selected cross-sections. The radial distance is normalized by the radius of the nozzle, R_0. The results from R1, R2 and R3 are indicated by solid black, dashed black and solid red lines respectively. Cross-section planes X_1 to X_8 are represented from top left to bottom right.

toroidal zone. Further downstream, the profiles slowly grow into a parabolic distribution with a decreasing peak value, down to 0.5 m/s at the late stages, i.e. the last plane X_8. Visible differences between different grid resolutions are observed most notably at X_6, where the highest levels of turbulence (and hence smallest structures) are present, as will be discussed later. The results with the finest mesh R3 (red lines in Figure 3.22) lead everywhere to an excellent agreement with measurement data. Even strongly under-resolved simulations, like R1, lead to fully correct and stable qualitative predictions, and stay even in fair quantitative agreement with measurement data outside of the transitional region, demonstrating the robustness of the employed numerical solver.

Viscous shear stress The magnitude of the mean viscous shear stress component σ_{xy} is shown in Figure 3.23. The peak of the viscous shear stress is found at around 25 Pa in the

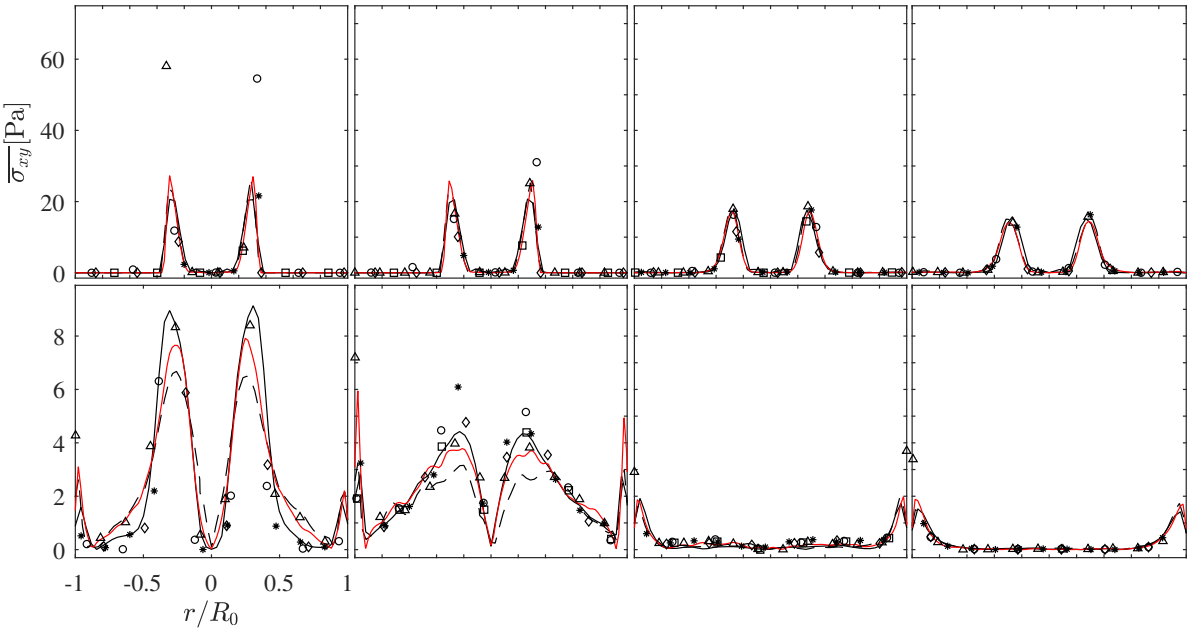

Figure 3.23: Results for Re = 3500. Time-averaged viscous shear stress compared with PIV experiments at selected cross-sections. The results from R1, R2 and R3 are indicated by solid black, dashed black and solid red lines respectively. Cross-section planes X_1 to X_8 are represented from top left to bottom right. Note the different vertical scales between the two rows.

throat section. The stress decreases gradually from plane X_2 to the end of the nozzle. The peak is shifted toward the shear layer between the jet and the recirculation zone during jet breakdown. The shear stress remains zero in the boundary layers of the recirculation region at planes X_3 and X_4, while it starts increasing there at plane X_5, before progressively going back to zero further downstream (relaminarization).

Reynolds stress Figures 3.24 and 3.25 show the normal Reynolds normal in axial direction at selected cross-sections and along the center-line, respectively. Ahead of the sudden

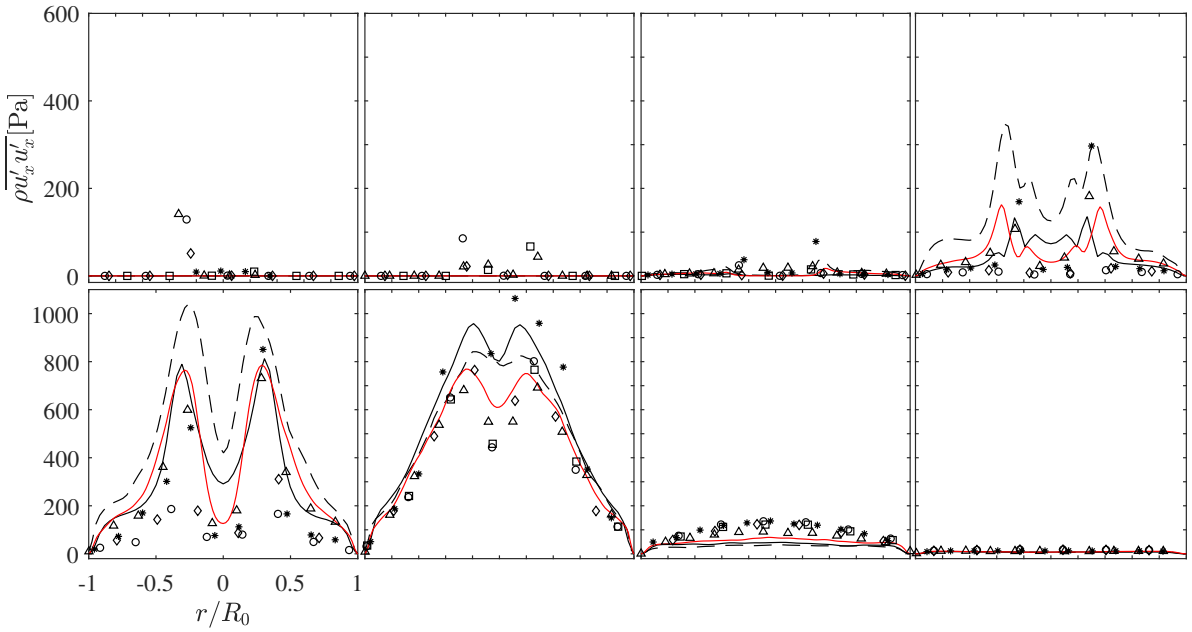

Figure 3.24: Results for Re = 3500. Time-averaged normal Reynolds stress in axial direction compared with PIV experiments at selected cross-sections. The results from R1, R2 and R3 are indicated by solid black, dashed black and solid red lines respectively. Cross-section planes X_1 to X_8 are represented from top left to bottom right. Note the different vertical scales between the two rows.

expansion section, the Reynolds stress is nearly zero, indicating laminar conditions.

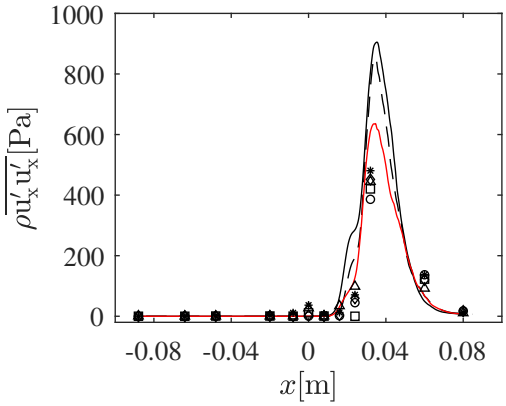

Figure 3.25: Results for Re = 3500. Comparison between LBM results and experimental data for normal Reynolds stress in axial direction along the center-line. The results from R1, R2 and R3 are indicated by solid black, dashed black, and solid red lines, respectively.

It experiences a sharp increase around plane X_4, reaching maximum values in planes X_5 and X_6. The peak of the normal Reynolds stress is found to be around 800 Pa for the finest resolution at X_6, where strong flow instabilities can be observed from Figure 3.21(a). Further downstream (cross-section planes X_7 & X_8) the turbulent stress goes back to zero, indicating

again relaminarization of the flow. While noticeable differences are observed among the three different resolutions (especially around the jet breakdown region), they are observed to converge toward experimental data, as seen in Figure 3.25. The numerical results from the finest mesh R3 fall within the PIV data and follow closely the corresponding trends, leading to an accurate description of jet breakdown. It must also be kept in mind that an accurate measurement of the Reynolds stress tensor based on PIV remains extremely challenging due to the needed resolution in space and time. As such, the experimental data used for the present comparison is certainly associated with a non-negligible level of experimental uncertainty, already visible in the widely different results obtained by the three experimental groups involved in the study.

3.3.3.3 Mildly turbulent flow, Re = 6500

At Re = 6500 (inlet Reynolds number of 2171), the flow regime is observed to be locally turbulent downstream of the sudden expansion region in the PIV and in the numerical simulations (see Figure 3.26(a)).

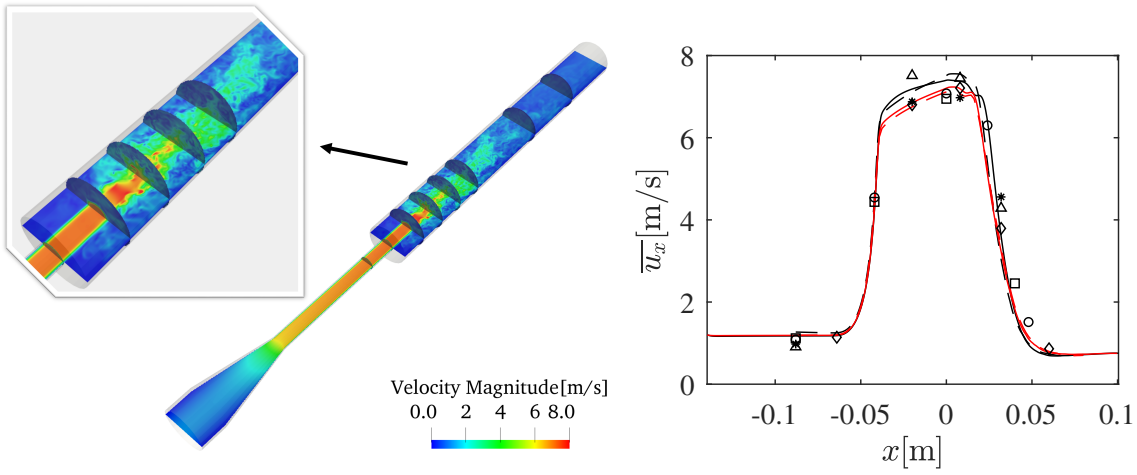

(a) (b)

Figure 3.26: Results for Re = 6500. (a) Instantaneous axial velocity field for mesh R1 at time $t = 11.925$ s. (b) Comparison between LBM results and PIV experiments for mean axial velocity along the center-line of the nozzle. The results from solid black, dashed black, solid red and dashed red lines, respectively.

Axial velocity The profiles of time-averaged axial velocity for the PIV data-sets and for the four LBM meshes (R1, R2, R3 and R4) are shown along the center-line in Figure 3.26(b). As in Figure 3.21(b) the LBM axial velocity profiles show very good agreement with PIV experimental data-sets. The results with mesh resolution R3 and R4 fall within the experimental symbols. It is worth noting that the jet from the coarsest mesh, R1, starts breakdown slightly later than at higher resolution. The axial velocity increases to a peak value around 7.5 m/s at $x = 0.01$ m, before decreasing very sharply to less than 0.5 m/s. This abrupt

decrease marks the onset of jet breakdown. All four resolutions are able to accurately predict the axial velocity distribution along the center-line throughout the FDA nozzle.

Radial profiles of axial velocity along sampling planes The time-averaged axial velocity profiles are illustrated at the selected cross-sections along the flow direction in Figure 3.27. It can be seen from the first two plots that the flow remains at the same peak

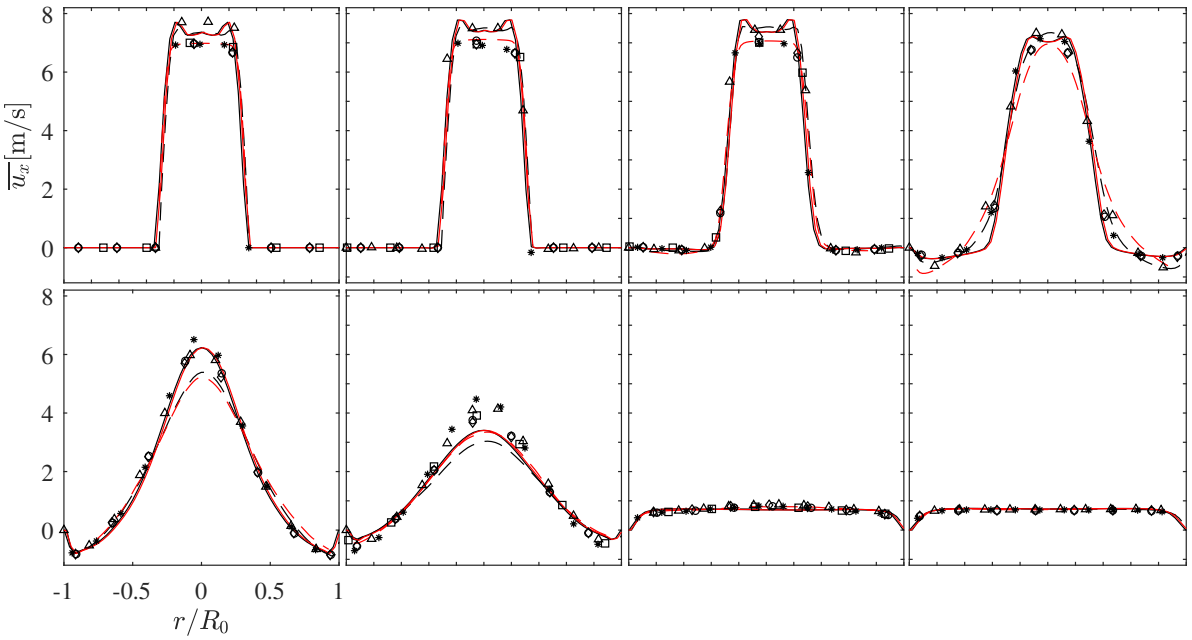

Figure 3.27: Results for Re = 6500. Time-averaged axial velocity compared with PIV experiments at the chosen cross-sections along the center-line. The radial distance is normalized by the radius of the nozzle, R_0. The results from R1, R2, R3 and R4 are indicated by solid black, dashed black, solid red and dashed red lines respectively. Cross-section planes X_1 to X_8 are represented from top left to bottom right.

velocity in the throat section; the numerical results from the four resolutions match well with the PIV experiments. Although the flow enters the expansion section at location X_3, the peak axial velocity is still the same as in the previous locations, in good agreement with PIV data. It is worth noting that a small negative velocity appears at cross-section X_4 near the boundary layers, while the peak axial velocity decreases only slightly. On the other hand, the peak axial velocity decreases drastically from section X_5 to X_6 in association with jet breakdown. At later stages, in the cross-sections X_7 and X_8, it can be observed that the peak values are relatively small (around 0.75 m/s). The numerical predictions match very well with the PIV data in this region where the jet collapses almost completely and the flow reattaches. Overall, the LBM results are in very good agreement with the experiments concerning jet breakdown. The mesh R3 captures correctly the axial velocity profile and the jet breakdown process throughout the nozzle.

Viscous shear stress The magnitude of the time-averaged viscous shear stress component σ_{xy} is shown at selected cross-sections in Figure 3.28. It can be noted that the viscous shear

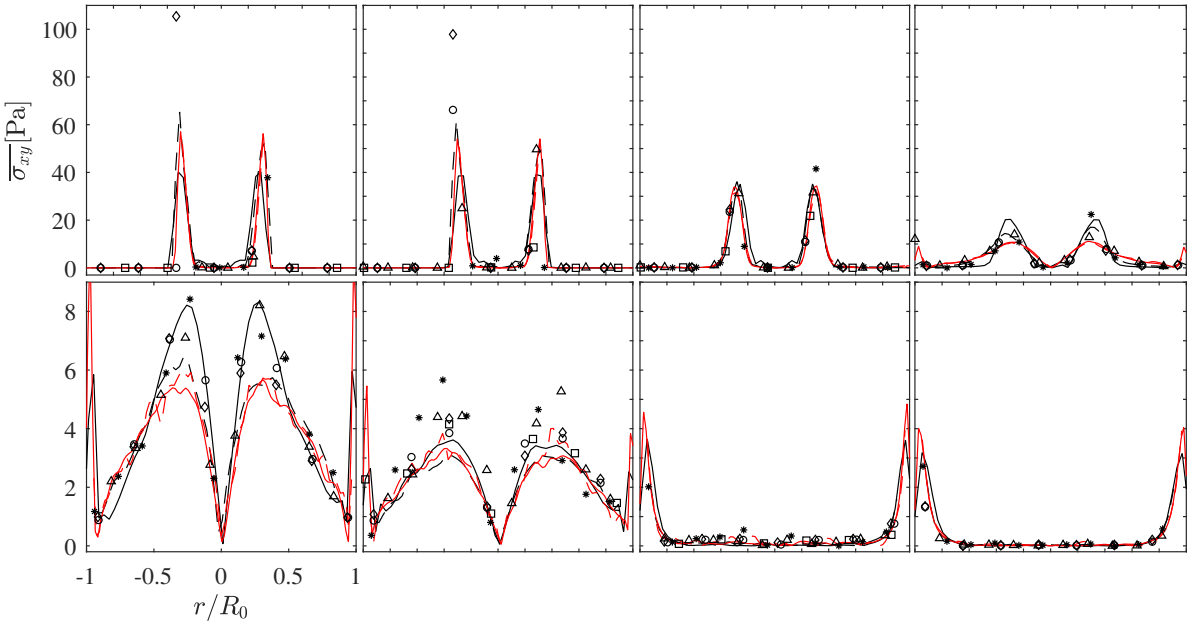

Figure 3.28: Results for Re = 6500. Time-averaged viscous shear stress compared with PIV experiments at selected cross-sections along the center-line. The results from R1, R2, R3 and R4 are indicated by solid black, dashed black, solid red and dashed red lines, respectively. Cross-section planes X_1 to X_8 are represented from top left to bottom right. Note the different vertical scales between the two rows.

stress reaches a peak around 50 Pa in the throat section, the largest velocity gradients being found as expected in the boundary layer. In the sudden expansion section, the peak of the viscous shear stress is predicted to be less than 8 Pa and is found in the shear layers between the central, high-velocity jet and the recirculating fluid. The peak of the viscous shear stress decreases further downstream. Later on, the effect of viscous shear stress can be fully neglected due to the uniform and low velocity found in the nozzle. The largest (but low) shear stress is found close to the boundary layer in cross-sections X_7 and X_8, which can be attributed to the jet reattachment to the wall. As expected, the shear stress is zero along the center-line. The height of the boundary layer is estimated to be around half of the throat diameter in both experimental and numerical results.

Overall, viscous shear can be neglected as the peak viscous stress is very small throughout the nozzle. Such a value should not be able to damage red blood cells. Depending on the studies, a shear stress exceeding about 100 Pa is necessary to observe any hemolysis [153].

Reynolds stress Figures 3.29 and 3.30 illustrate the normal Reynolds stress for selected cross-planes and along the center-line, respectively. It can be observed that the results are in good agreement with the experimental data throughout the nozzle, keeping in mind the large variations also found in the experiments. In the throat section (planes X_1& X_2), the

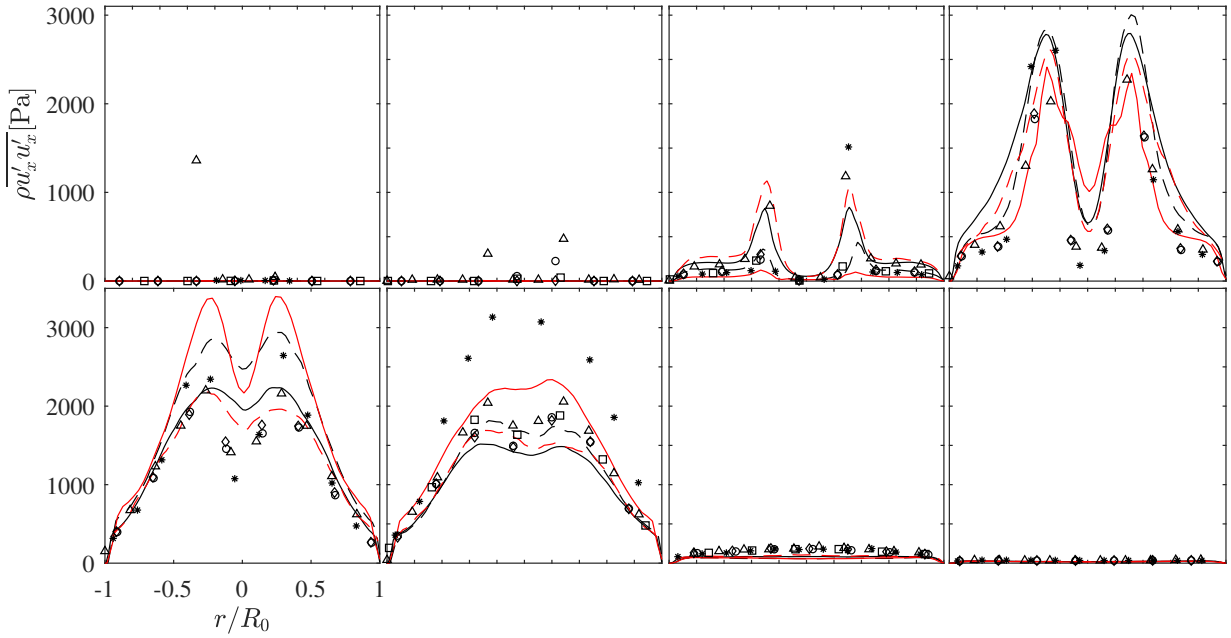

Figure 3.29: Results for Re = 6500. Comparison between LBM results and experimental data for axial Reynolds normal stress at different cross-sections. The results from R1, R2, R3 and R4 are indicated by solid black, dashed black, solid red and dashed red lines, respectively. Cross-section planes X_1 to X_8 are represented from top left to bottom right.

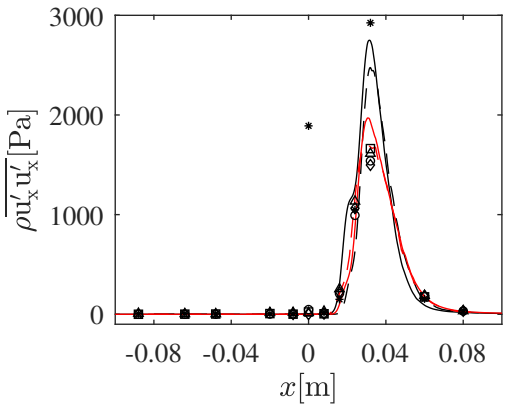

Figure 3.30: Results for Re = 6500. Comparison between LBM results and experimental data for axial Reynolds normal stress along the center-line. The results from R1, R2, R3, and R4 are indicated by solid black, dashed black, solid red and dashed red lines respectively.

numerical results are close to zero, as in most measurements (while few experimental sets show local peaks up to 1500 Pa; the experimental results vary very widely there). After flowing through the sudden expansion region, the Reynolds stress increases largely until the late stage of jet breakdown. The peak of Reynolds stress appears in this region in the shear layers between the central high-speed jet and the surrounding recirculating fluid, reaching around 3000 Pa between cross-sections X_5 and X_6. Further downstream, the Reynolds stress

starts decreasing sharply towards zero. The Reynolds stress is negligible in the throat as well as at the end of the nozzle.

3.3.4 Discussion

In this section, further information is provided concerning agreement and/or discrepancies between numerical results and PIV measurements in this study.

Laminar flow The in-house numerical tool ALBORZ successfully predicts the nature of the laminar flow. The jet induced after leaving the throat does not break down in the sudden expansion section. The numerical simulations accurately capture the fields of velocity and viscous shear stress.

Transitional flow Both numerical simulations and experiments show a transitional regime with a jet breakdown in the sudden expansion section at this Reynolds number of 3500. The location of the jet breakdown is accurately predicted by the simulations, around $x = 0.02$ m, which is later than for Re = 6500. The effect of the viscous shear stress would be negligible regarding hemolysis, due to its low peak value. Concerning the Reynolds stress, used to quantify the strength of turbulent velocity fluctuations and to assess indirectly the potential damage to blood cells, the obtained values are much higher and would be sufficient to trigger hemolysis. However, as explained in Yu et al. [153], there is still no clear consensus regarding critical values and unsteady effects must be taken into account to clearly assess the impact of stress on hemolysis.

Mildly turbulent flow The turbulent flow exhibits an earlier onset of jet breakdown, already around $x = 0.01$ m. Ahead of the sudden expansion section, the value of the Reynolds stresses are small, showing that there is no notable flow disturbance produced before and within the throat, as expected. Some discrepancies are found between numerical results and PIV measurements regarding Reynolds normal stress for cross-section planes X_5 and X_6. However, the differences are below the variations observed among the different experimental data-sets, the orders of magnitude are well predicted, and the shapes of the profiles coincide. It is therefore impossible to decide if the disagreements come from the numerical model or from experimental limitations.

3.3.5 Conclusions

Lattice Boltzmann simulations were performed on the FDA's benchmark nozzle, mimicking a simplified blood-contacting medical device, to assess the capability of the in-house solver ALBORZ in modelling such flows under laminar, transitional, and mildly turbulent conditions. For this purpose, Reynolds numbers Re = 500, 3500, and 6500 have been considered, for which experimental data are available. Velocity, viscous shear stress, and turbulent Reynolds stress were compared to the inter-laboratory PIV experiments documented in the literature [139]. Overall, numerical results are in very good agreement with the experimental

data, demonstrating that the solver is capable of predicting accurately the underlying flow physics. This applies even for under-resolved simulations (grid R1), allowing therefore very fast estimates, since results on grid R1 are typically obtained almost 20 times faster than on grid R3. When a very high accuracy is required, by increasing the resolution, results converge toward experimental profiles within the corresponding uncertainty. This shows that the solver can be used in a stable manner either 1) for a fast estimate of the flow conditions with a fair accuracy, or 2) to get very accurate flow predictions at the price of a much longer computational time. To our knowledge, this work is the first LBM study of the FDA's benchmark nozzle considering simultaneously laminar, transitional, and mildly turbulent flow conditions, providing comprehensive quantitative comparisons for the flow fields.

3.4 Validation of non-Newtonian fluid model

Part of this section has been published as:
Seyed Ali Hosseini, **Feng Huang**, Dominique Thévenin. Lattice Boltzmann model for simulation of flow in intracranial aneurysms considering non-newtonian effects. Physics of Fluids, 34(7):073105, 2022.

3.4.1 Plane Poiseuille flow

We consider a 2D flow between parallel plates driven by a constant and uniform body force along the channel. The height of the channel is H. The applied body force is $\boldsymbol{F} = (F_x, F_y)$. The fluid shows power-law fluid property, following:

$$\frac{\mu}{\rho} = \frac{k}{\rho}\dot{\gamma}^{(n-1)}, \tag{3.13}$$

where μ and ρ are the dynamic viscosity and density, respectively; k is the consistency index with the unit of $\mathrm{kg} \cdot \mathrm{s}^{n-2}/\mathrm{m}$, n is the power index. The fluid is shear-thinning when $0 \leq n < 1$; the fluid behaves as shear-thickening (or dilatant) when $1 < n$; while a fluid becomes Newtonian with constant viscosity of k when $n = 1$.

The Reynolds number is defined as:

$$\mathrm{Re} = \frac{u_{\max}^{2-n} H^n}{k/\rho}, \tag{3.14}$$

where the velocity reaches a maximum $u_{\max}$ at the centerline of the channel.

For such a 2D steady flow, the analytical solution of this system can be expressed as:

$$u_x(y) = \frac{n}{n+1}\left(\frac{F_x}{k/\rho}\right)^{\frac{1}{n}}\left(\left|\frac{H}{2}\right|^{\frac{n+1}{n}} - \left|\frac{H}{2} - y\right|^{\frac{n+1}{n}}\right). \tag{3.15}$$

To assess the accuracy of our solver, a series of simulations were carried out under different values of the power index n. The convergence analysis was done using different grid resolutions $N_y = \frac{H}{\delta r} \in \{20, 30, 40, 50, 60\}$ where δr is the grid size. On the basis of the below convergence criterion, the simulations were considered to have reached a steady state.

$$\sqrt{\frac{\sum_{i,j}(u_x(t,x,y) - u_x(t-\delta t,x,y))^2}{\sum_{i,j} u_x(t,x,y)^2}} < 10^{-10}. \tag{3.16}$$

The list of the above-mentioned parameters for the simulations are given in Table 3.3.

Table 3.3: Maximum velocities and force in Hagen-Poiseuille simulations.

n	0.25	0.5	0.75	1.0	1.25	1.5	1.75
F_x [-]	4.1E-5	1.25E-5	3.5E-6	1E-6	2.5E-7	7.0E-8	1.8E-8
$U_{\max}$ [-]	0.131	0.1373	0.1351	0.1406	0.1312	0.1359	0.133

After the flow reaches steady state, the velocity profiles were compared to the analytical solution from Eq. 3.15. The relative errors were estimated via an L2 norm:

$$E_{L2} = \sqrt{\frac{\sum_{i,j}(u_x - u_x^{\text{ref}})^2}{\sum_{i,j}(u_x^{\text{ref}})^2}}, \tag{3.17}$$

where $u_x^{\text{ref}}(x,y)$ is the analytical velocity in x direction.

Figure 3.31 demonstrates the velocity comparison between numerical results obtained from the finest resolution and the corresponding analytical solutions under different values of the power index n. This comparison points to an excellent agreement.

To further assess the accuracy of our solver, we summarize the relative error obtained from all simulations listed in Table 3.4 and plot the relative error vs. resolution in Figure 3.32. It can be clearly observed that for all power indices our numerical model is second-order accurate in space.

Table 3.4: L2 norm of error for Hagen-Poiseuille power-law fluid flow simulations.

N_y n	0.25	0.5	0.75	1.0	1.25	1.5	1.75
20	1.5E-02	6.4E-03	4.4E-03	3.6E-03	3.1E-03	2.8E-03	2.7E-03
30	6.7E-03	2.8E-03	2.0E-03	1.6E-03	1.4E-03	1.3E-03	1.3E-03
40	3.7E-03	1.5E-03	1.1E-03	9.2E-04	8.3E-04	7.8E-04	7.5E-04
50	2.5E-03	9.6E-04	7.3E-04	5.9E-04	5.4E-04	5.1E-04	5.0E-04
60	1.8E-03	7.2E-04	5.2E-04	4.1E-04	3.7E-04	3.6E-04	3.5E-04

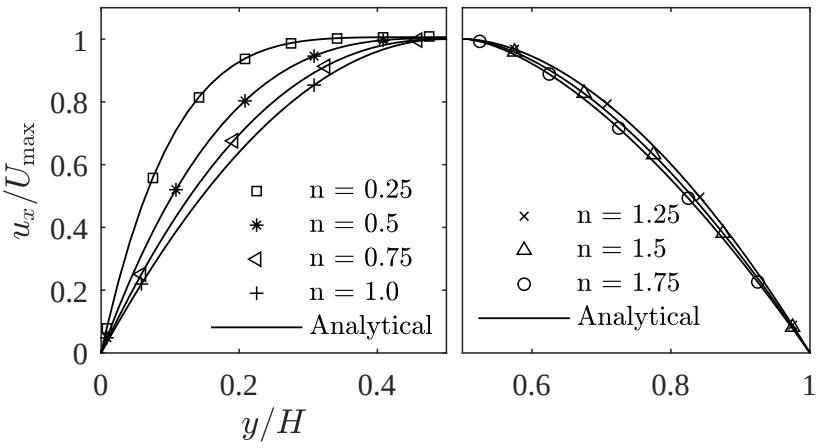

Figure 3.31: Comparison of velocity profiles for the power-law flows with different index n for Re = 100. The markers represent the numerical solutions and the solid lines are the corresponding analytical solution. It should be noted that for the sake of readability not all simulation grid-points are shown with the symbols.

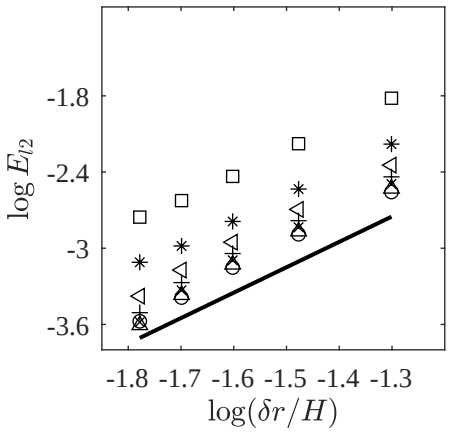

Figure 3.32: Scaling of the L2 norm of the global error for the 2-D steady Hagen-Poiseuille case. Symbols follow those selected in Figure 3.31. The solid line shows second-order convergence in space.

3.4.2 Lid-driven cavity

To further validate the accuracy and robustness of our solver, a lid-driven cavity case was chosen to test the model with a non-Newtonian fluid. A square box is considered with a side length of L; the top wall is moving with the horizontal velocity U_0. The other walls are static and a no-slip boundary condition is applied there. The Reynolds number is defined as:

$$\mathrm{Re} = \frac{U_0^{2-n} L^n}{k/\rho}. \tag{3.18}$$

We will consider both power indices 0.5 and 1.5 at Re = 500. The domain is discretized with 200 grid points in each direction. The grid size is thus set to $\delta r = L/200$ and the speed of the moving wall is non-dimensionalized as $U_0 = 0.1\delta r/\delta t$. The simulations are carried out until the convergence criterion is reached as defined in Eq. 3.16. The velocity data are extracted along the horizontal and vertical centerlines and then compared against the reference data from [6]. The results for both numerical simulations are shown in Figure 3.33 and point to an excellent agreement with the reference velocity profiles. To better illustrate the effect of

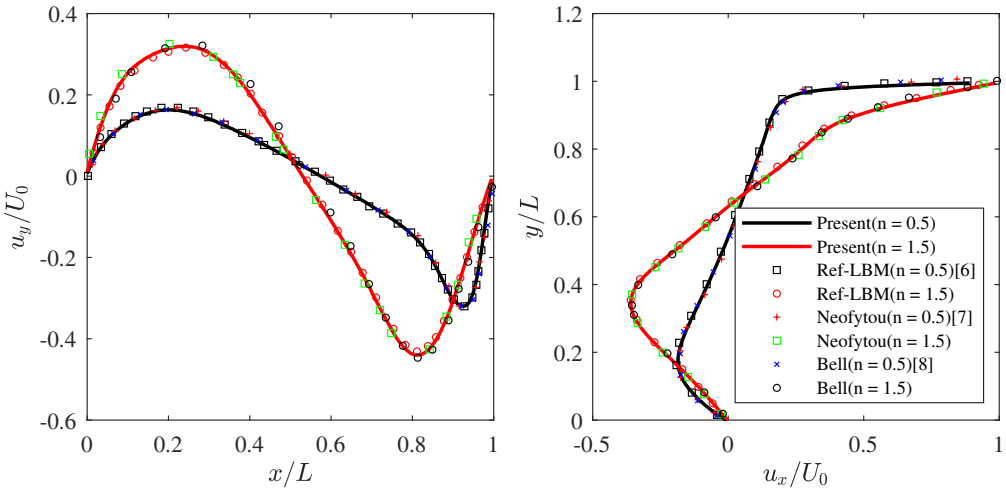

Figure 3.33: Steady-state velocity profiles along the (left) horizontal and (right) vertical centerlines at Re = 500 for (in red) $n = 1.5$ and (black) $n = 0.5$ as obtained from (solid lines) simulations and (markers) extracted from [6],[7],[8].

the fluid behavior index on the flow structure at the fixed Reynolds number, the vorticity magnitude fields of both cases are shown in Figure 3.34. It is observed that both peripheral

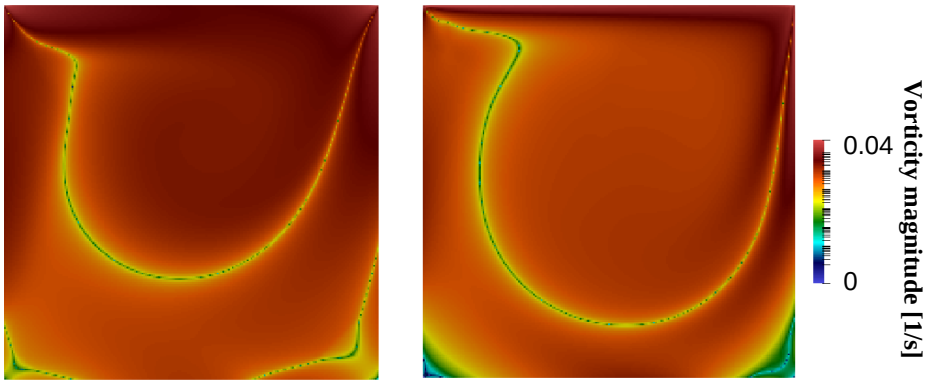

Figure 3.34: Steady-state vorticity magnitude field as obtained from simulations at Re = 500 for (left) $n = 1.5$ and (right) $n = 0.5$.

secondary vortices and the primary vortex are affected. The primary vortex is smaller and

more energetic for $n = 1.5$. This fact is also confirmed by the larger maximum/minimum velocities as shown in Figure 3.33. This concludes the successful validation of all numerical models employed in the present investigation.

Chapter 4

Importance of non-Newtonian effects in intracranial aneurysms

Contents

Part of this chapter has been published as:
Seyed Ali Hosseini, **Feng Huang**, Dominique Thévenin. Lattice Boltzmann model for simulation of flow in intracranial aneurysms considering non-newtonian effects. Physics of Fluids, 34(7):073105, 2022.

4.1 Introduction

From a biomechanical perspective, it is widely accepted that hemodynamic forces such as wall shear stress and pressure play a significant role in aneurysm rupture. When the forces acting on the aneurysm lumen wall exceed the strength of the lumen tissues, this results in material failure, tissues degradation, and ultimately rupture [154]. From a geometric point of view, the aspect ratio, shape and size of aneurysms may also have an effect on rupture risk [155, 156]. While considerable progress has been made in the past years, access to details of flow structures and accurate measurements of the velocity field within IAs via experimental measurements is still quite challenging. In recent years, given the rapid progress of numerical tools in computational fluid dynamics, those are becoming interesting non-intrusive alternatives to experimental studies in order to conduct systematic studies and get a better understanding of flow dynamics in IAs [30, 157, 158, 159, 160, 161].

Of the many open questions in that area, the issue of viscosity modeling for blood is one that has attracted much attention [162, 163, 164, 165, 166]. Blood is known to exhibit a shear-thinning behavior, which results from the mixture of suspended cells in the plasma. The velocity profile of blood is found to be flattened [167, 168] as compared to its counter-part under a Newtonian viscosity assumption. Compared to a pseudo-Newtonian blood there is less circulation, stagnation, and flow separation in the aneurysms [168]. In spite of this, most studies carried out simulations in cerebral aneurysms assuming a Newtonian fluid, as discussed e.g. by Fukazawa et al. [169]. However, it must be noted that the studies confirming usability of the Newtonian assumption were carried out in healthy arteries; there, the magnitude of shear rate is normally larger than 100 s^{-1} making non-Newtonian effects negligible [170]. On the other hand, IAs show a wide range of morphological variability leading to complex flow structures involving regions with low shear-rate [171, 172]. To the best of the authors' knowledge, there is still no consensus on whether rheological models should be employed to simulate intracranial aneurysms [162]. Therefore, further comprehensive studies using efficient numerical tools are needed to settle this issue. It must be noted that at smaller scales and Reynolds numbers non-Newtonian effects are more important, for instance in micro-vasculatures or the vasculature at arteriole/venules level. This is another area were non-intrusive methods like computational fluid dynamics can be used to elucidate non-Newtonian effects on the dynamic of the flow.

While publications on blood flow simulations using the lattice Boltzmann method are now quite well-spread, hemodynamic simulations of realistic 3-D patient-specific geometries and flow-rates involving non-Newtonian properties are still rather limited [173, 174]. Publications considering the specific context of cerebral aneurysms are even more scarce [105], even if the first article describing the implementation of non-Newtonian viscosity laws within the

lattice Boltzmann framework can be dated back to as far as 1993 [175]. Many articles have since been published [176, 177, 178, 179, 180, 181, 182], but all of them have been limited to simple flow configurations with no specific intent of porting the model to medical flows. Furthermore, from a more technical point of view, most if not all models proposed since [175] rely on a second-order expansion of the equilibrium distribution function leading to well-known Galilean-variant errors in the viscous shear stress tensor. On top of this, both single relaxation and multiple relaxation time formulations[183, 184] have considered the full rate-of-strain tensor including dilatation contributions when computing the apparent viscosity of non-Newtonian models. Given that in lattice Boltzmann simulations the sound speed is rescaled and orders of magnitude smaller than the actual speed of sound of the configurations of interest, which in turn leads to large compressibility effects and velocity field divergence, this could possibly cause a noticeable over-estimation of the apparent viscosity.

In this work, we propose a solver overcoming most issues related to the classical lattice Boltzmann formulation when dealing with incompressible flows. The model makes use of the full Hermite expansion of the discrete equilibrium distribution function, eliminating the cubic errors in the deviatoric components of the viscous stress tensor and making the apparent viscosity in non-Newtonian fluid simulations Galilean-invariant. The collision model is replaced with a modified version of the central Hermite polynomials-based multiple relaxation time model allowing for a much wider domain of stability and independent control over the dissipation rate of acoustic modes [53, 185]. This is an interesting property for the simulations considered here, as it allows for a very fast elimination of acoustic waves; given the re-scaling of the speed of sound in lattice Boltzmann, those are non-physical, spurious, and should be avoided as far as possible. Finally, the rate-of-strain contribution is computed excluding dilatation, as done classically using a classical discretization (finite volumes, elements, or differences), using the second-order moment of the non-equilibrium part of the distribution function and the resulting system of equations, i.e. the evaluation of the apparent viscosity, is solved via a point-wise implicit solver.

4.2 Simulations of fluid flow with non-Newtonian models.

4.2.1 Idealized aneurysm model

As the first non-canonical configuration we consider an idealized aneurysm geometry. The corresponding geometry has already been presented in Figure 3.1(a), with inflow conditions shown in Figure 3.2. In Section 3.1.2.2 the viscosity was defined via a Newtonian fluid model in order to reproduce the experiment in which a (Newtonian) mixture of distilled water, glycerin, sodium iodide and sodium thiosulphate with a density of $\rho_{\mathrm{BAL}} = 1221$ kg/m^3 and a viscosity of $\mu_{\mathrm{BAL}}/\rho = 3.2 \times 10^{-6}$ m^2/s was used. Now, non-Newtonian fluid models are employed in the same configuration. To provide a first illustration of non-Newtonian effects in a typical cerebral aneurysm four simulations with four different viscosity models are conducted: (a) Newtonian, (b) power-law, (c) Carreau-Yasuda and (d) Cross model.

While the power-law model follows that defined in previous sections, the Carreau-Yasuda model is defined as:

$$\mu(\dot{\gamma}) = \mu_\infty + (\mu_0 - \mu_\infty)[1 + (\lambda\dot{\gamma})^a]^{\frac{(n-1)}{a}} \tag{4.1}$$

where μ_0 and μ_∞ are the zero-shear-rate and infinite-shear-rate dynamic viscosities, respectively, λ and n are the relaxation time constant and the power-law index, while the last parameter a is a dimensionless coefficient that characterizes the width of the transition region between the zero-shear-rate region and the power-law region. The Carreau-Yasuda model turns into the Carreau model if $a = 2$. The Cross model is defined as:

$$\mu(\dot{\gamma}) = \mu_\infty + \frac{\mu_0 - \mu_\infty}{[1 + (\lambda\dot{\gamma})^n]}. \tag{4.2}$$

The parameters used in each model follow those proposed in the literature and are listed in Table 4.1.

Table 4.1: Summary of model parameters used for the ideal aneurysm configuration.

model	μ_∞[Pa.s]	μ_0[Pa.s]	λ[s]	a	n
Newtonian	0.004	-	-	-	-
Power law	0.01467	-	-	-	0.7755
Carreau-Yasuda	0.0035	0.16	8.2	0.64	0.2128
Cross	0.0036	0.126	8.2	1	0.64

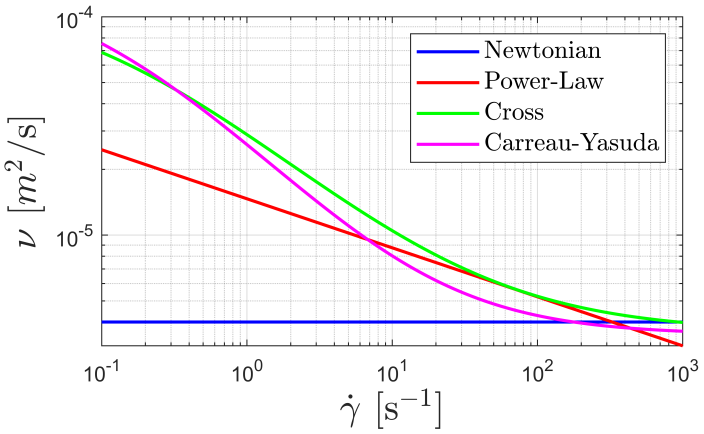

Figure 4.1: Shear-rate dependent viscosity as described by the four different laws used for the ideal aneurysm case: (blue) Newtonian, (red) power-law, (green) Cross and (magenta) Carreau-Yasuda.

To better illustrate the difference between the four models, the apparent viscosity as a function of shear rate is plotted in Figure 4.1.

As discussed in the introduction it is indeed observed that in the limit of high shear rate values, i.e. above 100 s^{-1} all four models converge to the Newtonian fluid behavior. In order

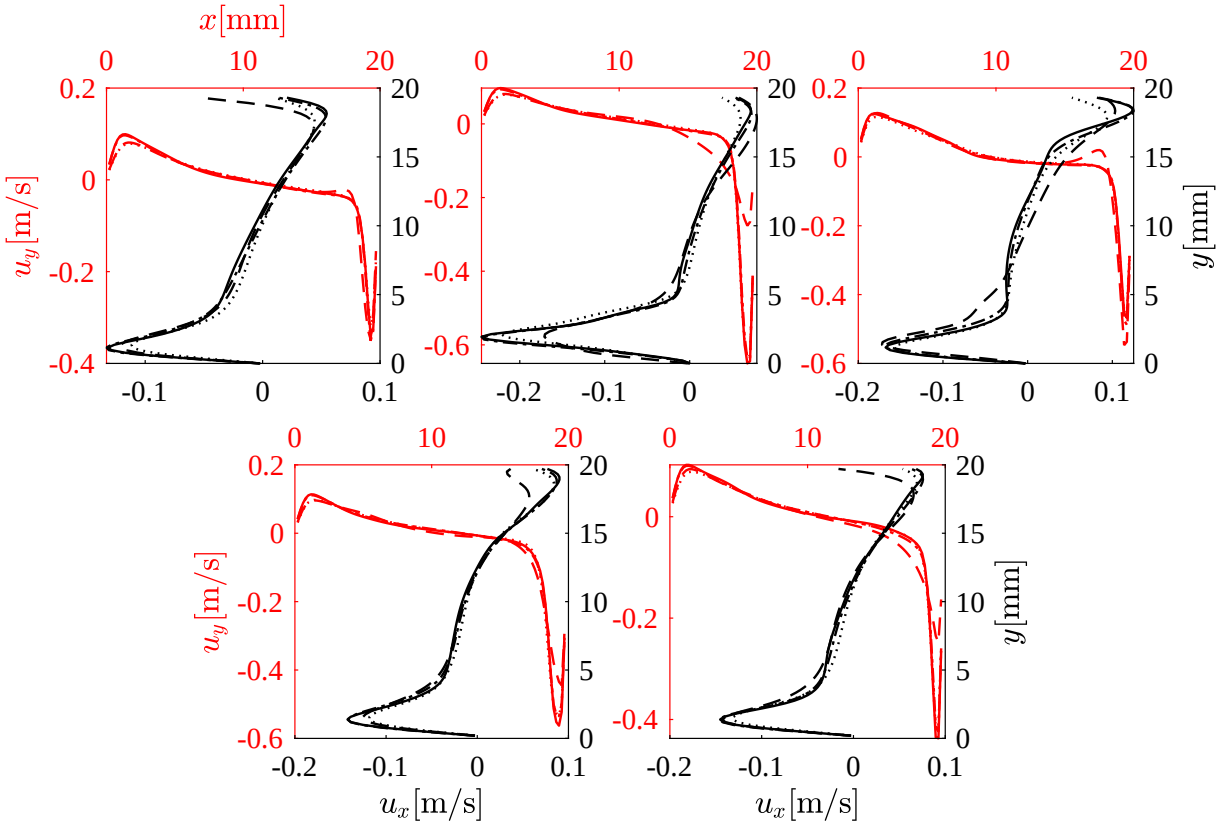

Figure 4.2: Velocity profiles on the center-lines along the (red) x- and (black) y-axes as obtained from simulations using: (plain line) Newtonian, (dashed line) power-law, (dash-dotted line) Carreau-Yasuda, and (dotted line) Cross at different times: (top row from left to right) 0.2, 0.3, 0.5 and (bottom row from left to right) 0.6 and 1 s.

to make sure that the impact of the initial condition is negligible, the simulations were carried out over four cardiac cycles and only data from the last cycle was used. In all simulations time-step and mesh sizes were set to $\delta t = 1.5 \times 10^{-5}$ s and $\delta r = 1.25 \times 10^{-4}$ m, respectively. This choice resulted in $2,687,000$ grid-points and $267,000$ time-steps. Simulations were run with 300 cores at an average speed of 0.6 million lattice updates per second per core. The velocity profiles at different times of a cycle along the two center-lines inside the sac are shown in Figure 4.2. While no major difference in terms of flow structure is observed, velocity profiles exhibit non-negligible differences both in the central (low strain) region and close to the aneurysm sac walls, where a larger strain-rate is found. These differences are further illustrated with iso-surfaces of the velocity magnitude in Figure 4.3. To clarify the reason behind these differences, we extracted a normalized probability distribution function

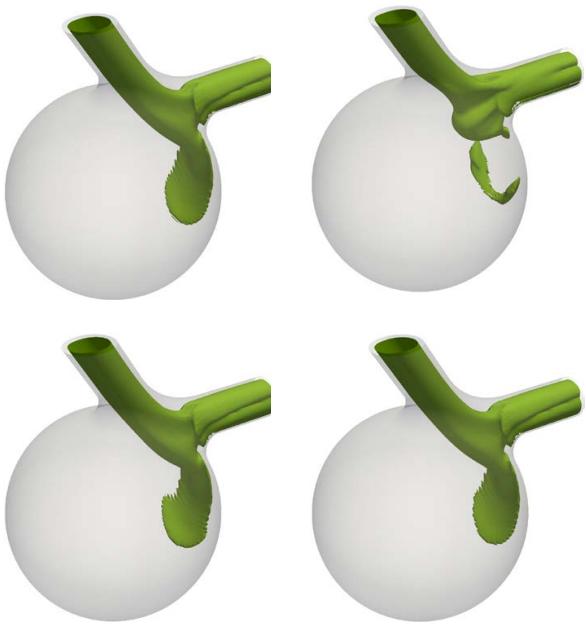

Figure 4.3: Isosurface of velocity (magnitude of 0.4 m/s) at peak systole. From top left to bottom right: Newtonian, Power-law, Carreau-Yasuda, and Cross model.

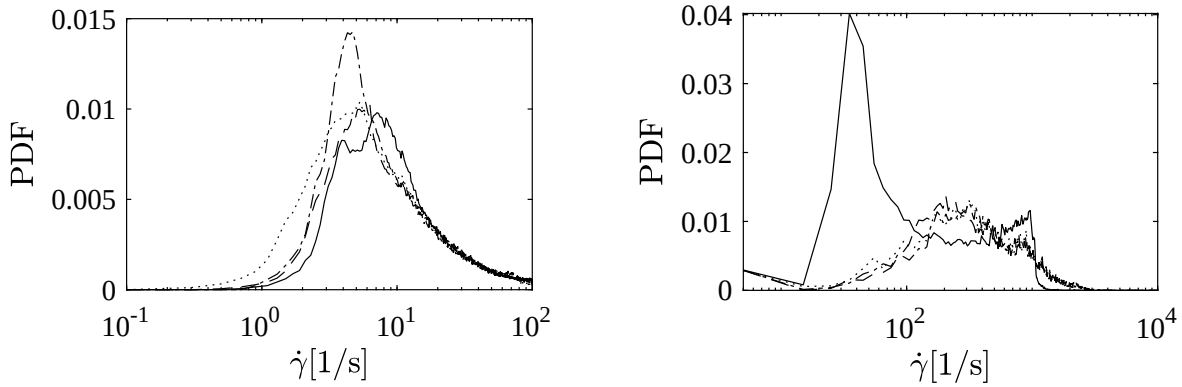

(a) Inside the sac

(b) Outside the sac

Figure 4.4: Probability distribution function of the shear rate inside and outside the aneurysm sac at peak systole as obtained from simulations using (plain line) Newtonian, (dashed line) power-law, (dash-dotted line) Carreau-Yasuda, and (dotted line) Cross model. Note the different horizontal scales.

for the shear rate in the sac region, $f(\dot{\gamma}, \boldsymbol{r}, t)$ such that:

$$\int_{\dot{\gamma}=0}^{\dot{\gamma}=\infty} \int_V f(\dot{\gamma}, \boldsymbol{r}, t) d\dot{\gamma} dV = 1. \tag{4.3}$$

This probability distribution function at peak systole is illustrated in Figure 4.4.

Here, it is clearly observed that contrary to healthy cerebral arteries the majority of the volume within the sac is subject to low shear rates, i.e. $1 < \dot{\gamma} < 30$ s^{-1}, meaning that non-Newtonian effects might indeed become non-negligible. To further confirm the difference between hemodynamics in healthy arteries and in the sac a similar plot is shown for regions outside the sac in Figure 4.4.

In agreement with observations reported in the literature, the majority of the flow volume is subject to high shear rates in the arteries, explaining why the use of a Newtonian assumption is reasonable there.

4.2.2 Patient-specific cerebral aneurysm

To better illustrate the robustness of the solver and also provide additional details on the behavior of the shear rate in realistic configurations, we finally consider the cases of two

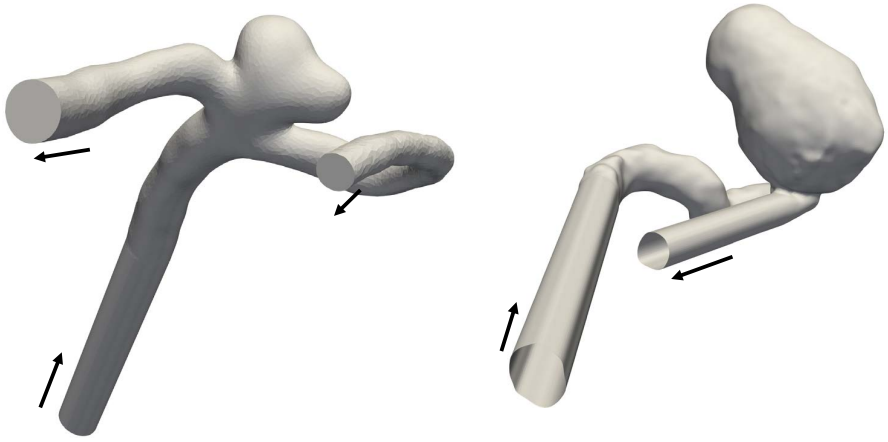

Figure 4.5: Geometries for the patient-specific cerebral aneurysm cases (first configuration: left, second configuration: right).

patient-specific cerebral aneurysms. The corresponding geometries are shown in Figure 4.5. The simulations are carried out assuming a density of $\rho = 1054$ kg/m^3 and using a modified Cross viscosity law defined following [165]:

$$\mu = \mu_{\text{inf}} + \frac{\mu_0 - \mu_{\text{inf}}}{(1 + \lambda^n \dot{\gamma}^n)^a}, \tag{4.4}$$

with $\mu_{\text{inf}} = 0.00369$ Pa $\cdot$ s, $\mu_0 = 0.056$ Pa $\cdot$ s, $\lambda = 3.736$ s^{-1}, $n = 2.406$ and $a = 0.254$. In both simulations time-step and grid sizes are set to $\delta r = 7.5 \times 10^{-6}$ s and $\delta t = 7.5 \times 10^{-5}$ m which result in respectively 4.9 and 14.5 million grid-points and 530 thousand time-steps.

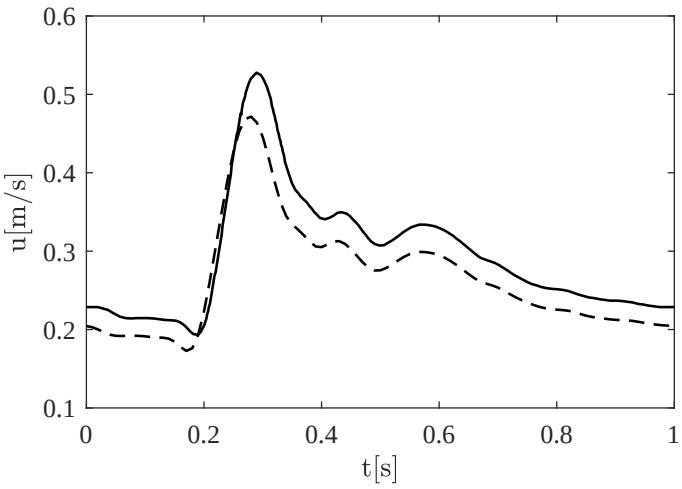

Figure 4.6: Inlet velocity changes with time over one cycle for the patient-specific aneurysm cases. Plain line: first configuration, dashed line: second configuration.

Simulations were carried out using 500 cores for an average performance of 0.63 million lattice updates per second per core. Outlets are modeled via a constant-pressure boundary condition, set to $P_{\text{out}} = \rho c_s^2$, while inlets are subject to pulsatile velocity conditions with a plug-flow profile. The prescribed inlet velocities over time are shown in Figure 4.6. The simulations are conducted over four cycles and only data from the last cycle is used for the analysis.

Figure 4.7: Streamlines at different times over a cycle for the first patient-specific configuration. From left to right: 0.1, 0.3, 0.5, 0.7 and 0.9 s. The red iso-surfaces show regions with shear rates below 100 s^{-1}.

The flow field of the first configuration over a cycle is illustrated in Figure 4.7. As for most aneurysms a persistent vortical structure fed by the incoming flow is observed within the aneurysm sac. At the difference of the ideal configuration, there does not seem to be a large

low shear rate region within the aneurysm sac at peak systole. This is further confirmed by the probability distribution function of the shear rate. The distribution of shear rate at two different times corresponding to the minimum and maximum inlet velocities are shown in Figure 4.8(a). The plot shows that while at peak systole the shear rates within the sac

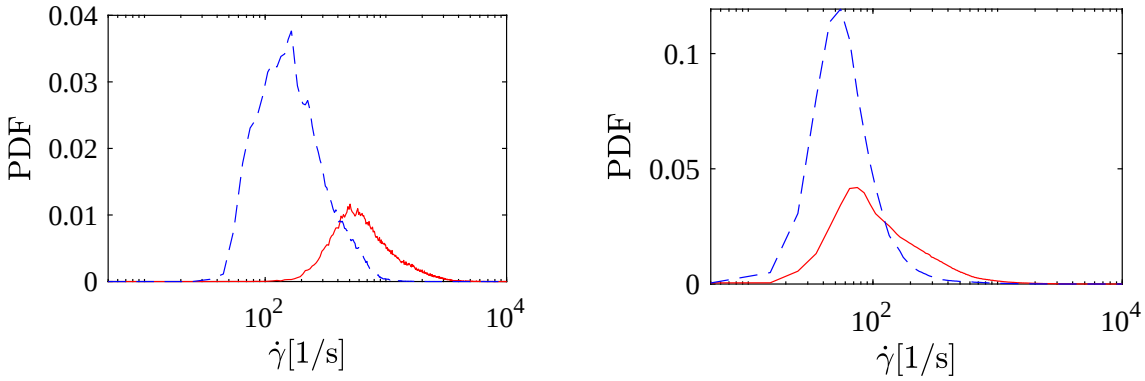

(a) Configuration 1

(b) Configuration 2

Figure 4.8: Probability distribution function of the shear rate inside the patient-specific aneurysm sac for both configurations at two different times: (blue dashed line) $t = 0.2$ s, minimum inlet velocity; and (red solid line) $t = 0.3$ s, maximum inlet velocity.

are concentrated around a large value of 400 s^{-1}, they do not go much below 100 s^{-1} at the lowest inlet velocity.

The second configuration, involving a larger aneurysm, along with the corresponding shear rate field within the sac over one cycle is illustrated in Figure 4.9. Different from the previous patient-specific configuration, large portions of the sac have shear rates below 100 s^{-1}. This is confirmed by looking at the shear rate distribution within the sac, shown in Figure 4.8(b). This demonstrates the high sensitivity of shear rate – and hence of viscosity modeling - towards the exact vasculature geometry.

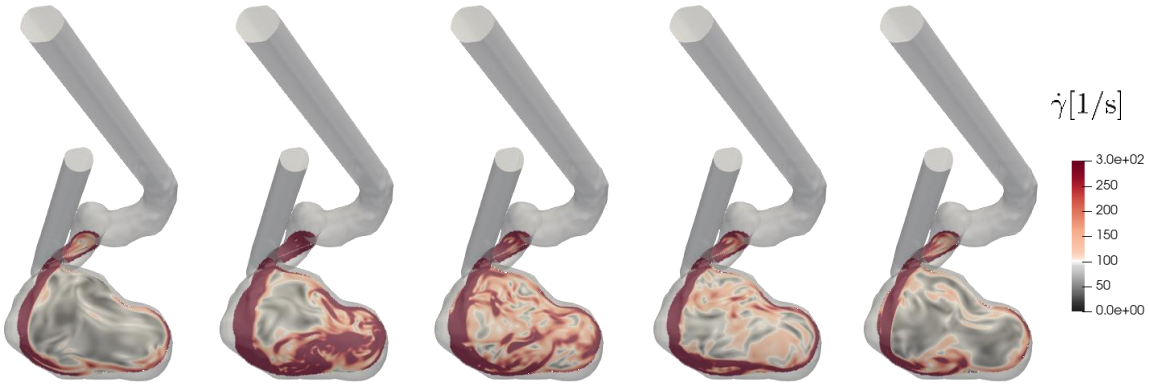

Figure 4.9: Shear rates at different times over a cycle for the second patient-specific configuration. From left to right: 0.1, 0.3, 0.5, 0.7 and 0.9 s.

4.3 Summary

In this chapter the developed lattice Boltzmann solver has been extended for the simulation of non-Newtonian blood flows, allowing an accurate description of hemodynamics in cerebral aneurysms. The model ensures Galilean-invariant viscosities and allows for independent control over the bulk viscosity. Furthermore, the use of the central Hermite polynomials-based collision operator allows for a wider stability domain and therefore a wider range of accessible time-step and mesh sizes. The solver was used to model the flow in an ideal cerebral aneurysm geometry with different viscosity laws. The results showed that the choice of the viscosity model noticeably affects the flow field, especially within the aneurysm sac – in its center as well as close to the walls. The importance of non-Newtonian effects was further characterized via a probability distribution function for the shear rate showing that large parts of the volume within the aneurysm sac are subject to low shear rates; there, non-Newtonian effects are prominent. We finally demonstrated the robustness of the numerical model by simulating the pulsating flow in patient-specific aneurysms, revealing noticeable differences and opening the door for systematic studies of non-Newtonian effects in different types of cerebral aneurysms to clarify their role and importance.

Chapter 5

Transition to turbulence in intracranial aneurysms: study of hydrodynamic fluctuations

Contents

5.1 Introduction

With the development of non-invasive medical imaging techniques, unruptured intracranial aneurysms are being increasingly detected. While many patients with aneurysms may remain healthy throughout their life, the risk of rupture stays present in connection with aneurysm growth. The rupture, in turn, can be fatal or often lead to severe disabilities [16, 186]. Most treatments for aneurysms involve surgical interventions, which may result in complications and sometimes even increase again the risk of aneurysm rupture. This highlights the need for a better *a priori* evaluation of rupture risk. To address this, a number of attempts have been made to systematically quantify rupture risk. E.g., Greving et al. [187] developed a risk score system (PHASES) used to predict the risk of aneurysm rupture based on various patients and aneurysm characteristics, such as smoking habits, size and location of aneurysms, etc. Despite lower risk scores indicating that there is no need for further treatment, such aneurysms may still rupture, pointing to the need for further research to better understand and predict the rupture risk and improve patient treatment outcomes.

It has been argued that hemodynamics play an important role in the initiation, growth, and subsequent rupture of intracranial aneurysms [85, 172]. The presence of oscillatory shear stress distributions and complex flow patterns within the aneurysm sac has been hypothesized to be a potential contributor to the rupture of aneurysms [188, 189]. The existence of such unsteady flow structures is currently a hot topic of discussion within the community. Advanced in vivo experiments and numerical studies observing non-laminar blood flow behavior associated with intracranial aneurysms have been documented in the literature [4, 126, 190, 191]. Kurokawa et al. [192] reported sound at frequencies in the range of 150-800 Hz caused by flow-induced vibration of the aneurysm wall. Steiger et al. [193] reported low-frequency flow fluctuations in cerebral saccular aneurysms of six patients out of twelve using Intraoperative Doppler recording. A spectral analysis and concomitant glass model studies showed a correlation between flow fluctuation and aneurysm type. Unexpected vibrations were also reported in experimental aneurysm studies, which are possibly associated with fluctuating flows [194, 195, 196, 197, 198]. The significance of fluctuations in blood flow has been thoroughly explored and discussed by Steinman and his research team [199]. They found that significant narrow-band vibrations ranging from 100 to 500 Hz could be detected in two out of the three tested aneurysm geometries. This finding is in accordance with the study by Jain [200]. Furthermore, the pulsatile nature of blood flow has been observed to influence aneurysm stability in both numerical and experimental studies [201, 202]. It is indeed known that a pulsatile flow can become transitional in a straight pipe during the deceleration phase of the oscillation at Reynolds numbers below 2000 [203]. This explains why several studies discovered indications of transitional flow in cerebral vessels, despite the low Reynolds numbers found there, and suggesting an elevated risk of rupture [204, 205].

CFD, due to its non-invasive nature, is increasingly used to investigate the hemodynamics in patient-specific intracranial aneurysms. Numerous high-fidelity CFD studies have been conducted to study, among other aspects, flow fluctuations in ruptured and unruptured intracranial aneurysms [172, 206, 207, 208, 209]. From statistical analysis, they found that

the occurrence of a rupture in aneurysms is correlated with abnormally high and low wall shear stresses, high oscillatory shear acting on the vessel wall, the presence of complex flow structures, and concentrated inflow jets. Baek et al. [210] reported flow instabilities occurring during the deceleration phase of a cardiac cycle at the internal carotid artery and concluded that the occurrence of low-frequency fluctuations depended on the geometry. Ford et al. [211] and Valen-Sendstad et al. [205, 212] confirmed the presence of high-frequency fluctuations in patient-specific terminal and intracranial aneurysms. Still, many CFD studies may be overlooking potentially relevant flow features such as high-frequency flow instabilities, simply due to inappropriate solver properties (highly dissipative schemes) and/or inadequate spatial and temporal resolutions, fluid models, or boundary conditions [213, 214].

As of today, a generalizable criterion for accurately assessing the risk of rupture in intracranial aneurysms remains elusive [215]. In an attempt to contribute to the discussion on the existence and properties of flow fluctuations, we consider in the present study five patient-specific intracranial aneurysms with known outcomes via direct numerical simulations (DNS, i.e., resolving properly all physical scales in time and space): two remaining unruptured, and the other cases rupturing within the sac. Additionally, both Newtonian and non-Newtonian fluid models will be considered in the DNS, since non-Newtonian behaviour could play an important role, as discussed in the previous chapter.

This comparative study can be used to provide valuable information regarding the underlying mechanisms and possible consequences on hemodynamics.

5.2 Configurations and numerical set-up

5.2.1 Case description

In the present study, hemodynamic features are investigated in five patient-specific intracranial aneurysm geometries. The configurations are shown in Figure 5.1. The flow values at up to 9 points were tracked upstream and downstream of the aneurysms, as well as within the aneurysm sac, in order to monitor any manifestation of possible flow fluctuations. It is worth noting that all the inlets and outlets were extended five diameters along the normal vector of the corresponding surfaces to reduce possible effects of the inlet and outlet boundary conditions. Furthermore, for Newtonian cases, blood was assumed to be an incompressible fluid with a constant density and viscosity. However, in the non-Newtonian scenario, the modified Cross model was employed to depict the rheological properties of blood. Detailed parameters can be found in the accompanying Table 5.1. All simulations were conducted over three cycles, with data sampling carried out during the third cycle in order to eliminate any potential effects stemming from initial transients.

Patient A This aneurysm was detected in the posterior inferior cerebellar artery (PICA) in a 51-year-old female patient. The rupture location is known within the aneurysm sac. The 3D-DSA scan was carried out on an AXIOM-Artis (Siemens Healthineers AG, Forchheim, Germany) with the same spatial resolution (0.28 mm) as in the other cases. The raw images

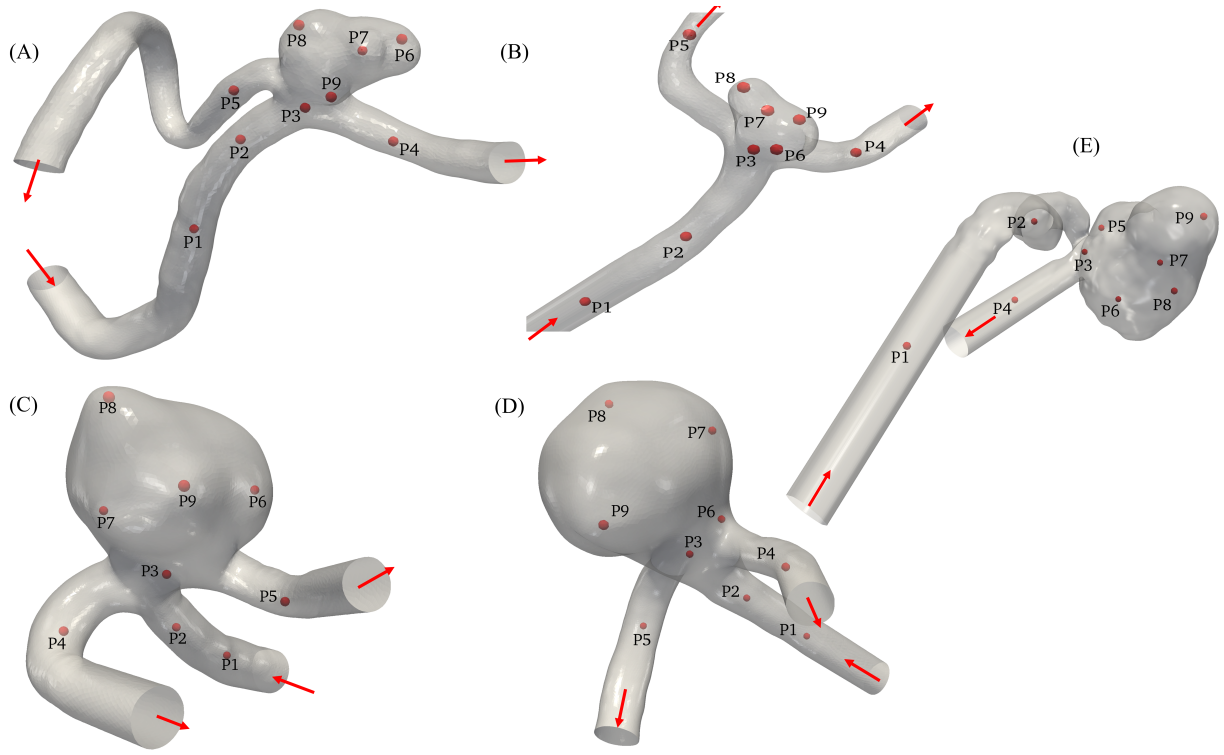

Figure 5.1: Representation of the five patient-specific aneurysm models (Case A, B, C, D, E) employed in simulations. The red arrows point to the inlets and outlets, respectively. Note that point P6 corresponds to the ruptured location in case A, while the ruptured points are unknown in other patients.

Table 5.1: Summary of numerical simulation parameters used in this study, encompassing aneurysm status, size, three different spatial (δ_r) and temporal (δ_t) resolutions (low resolution LR, medium resolution MR, high resolution HR), the corresponding Courant- Friedrichs-Lewy number (CFL), computation time in core hours, as well as the physical properties including density and viscosity.

Case ID	Status	Size[mm^3]	δ_r[m] / δ_t[s]			CFL	ρ[kg/m^3]	ν[m^2/s]	Core-h
			LR	MR	HR				
A	Ruptured	21.20*37.61*19.70	2.6×10^{-4}/ 7.6×10^{-6}	1.3×10^{-4} / 3.8×10^{-6}	6.5×10^{-5} / 1.9×10^{-6}	0.052	1000	4.0E-6	8.76E3
B	Unruptured	32.50*18.40*11.10							3.81E3
C	Ruptured	12.29*20.59*14.06	-	-	6.5×10^{-5} / 1.9×10^{-6}	0.052	1055	3.8E-6	2.06E3
D	Unruptured	13.30*14.56*17.30	-	-	6.5×10^{-5} / 1.9×10^{-6}	0.052	1055	3.8E-6	1.94E3
E	Ruptured	59.26*34.48*34.98	-	-	6.5×10^{-5} / 1.9×10^{-6}	0.052	1000	4.0E-6	3.90E4

were reconstructed using the "EE/auto" kernel (Siemens Healthcare GmbH, Forschheim, Germany). The geometric models of the aneurysms were reconstructed on this basis and further processed to simplify numerical simulations, retaining only the intracranial aneurysms and the corresponding major arteries to guarantee reasonable inflow and outflow, while the

distal arterial segments were cut off.

Patient B The unruptured aneurysm (of size 1.6 mm) was found in the middle cerebral artery (MCA) in a 53-year-old female patient who experienced an acute subarachnoid hemorrhage and severe headaches and was treated by coiling. The three-dimensional rotational angiography (3DRA) was performed on an Artis Q angiography system (Siemens Healthineers AG, Forchheim, Germany) with a spatial resolution of 0.28 × 0.28 × 0.28 mm to produce tomography slices of the volume of interest. Subsequently, the reconstructed raw image was acquired from a syngo X Workplace (Siemens Healthcare GmbH, Forchheim, Germany) through an "HU auto" kernel. Further details can be found in reference [216].

Patient C and D The two patient-specific aneurysms were roughly matched based on sex (female), age (83 years old for patient C and 63 years for patient D), location (middle cerebral artery), size (11.7 mm maximum diameter for patient C and 9.6 mm for patient D), and similar shape. Additional information about the patient's medical histories can be found in the reference [217].

Patient E In order to study the effect of Reynolds number on the flow instability, the ruptured giant cerebral aneurysm (of size 26 mm) from Steinman et al. [4] was selected, which was detected in the left internal carotid artery (ICA) in a 62 years old female patient. The nominal inlet diameter was measured to be 5.58 mm, and the corresponding peak Reynolds numbers were 513 and 651, respectively. Further information regarding the patients' history is available in reference [5].

5.2.2 Quantitative analysis methods

5.2.2.1 Fluctuating kinetic energy

Fluctuating (or turbulent) kinetic energy (FKE) serves as a crucial metric for quantifying flow fluctuations. In the context of the present study, we will focus the majority of our analysis on fluctuating components of the velocity field. To quantify the variations, the instantaneous velocity is decomposed into a mean component $\overline{\boldsymbol{u}}(\boldsymbol{r},t)$ and a fluctuating component $\boldsymbol{u}'(\boldsymbol{r},t)$ where:

$$\overline{\boldsymbol{u}}(\boldsymbol{r},t) = \frac{1}{\Delta t}\int_{t_0}^{t_0+\Delta t} \boldsymbol{u}(\boldsymbol{r},t)dt, \tag{5.1}$$

where Δt is the averaging period and:

$$\boldsymbol{u}'(\boldsymbol{r},t) = \boldsymbol{u}(\boldsymbol{r},t) - \overline{\boldsymbol{u}}(\boldsymbol{r},t). \tag{5.2}$$

FKE, a variable we will be using quite frequently, is expressed as:

$$\mathrm{FKE}(\boldsymbol{r},t) = \frac{1}{2\Delta t}\int_{t_0}^{t_0+\Delta t} \boldsymbol{u}'(\boldsymbol{r},t)\boldsymbol{u}'(\boldsymbol{r},t)dt. \tag{5.3}$$

5.2.2.2 Power spectral density

Power spectral density (PSD) shows how the power of a signal is distributed over the frequency domain; this provides a quantitative measure of flow fluctuations. Here, the PSD at each probe point has been computed using Matlab (Welch's method).

The discrete-time power spectral density ($S_{xx}(f)$) is defined at frequency f by [218]:

$$S_{xx}(f) = \frac{\delta_t^2}{\Delta t} \left| \sum_{t=t_0}^{t_0+\Delta t} \phi(t) \exp\left[-2\pi\sqrt{-1} f(t-t_0)\right] \right|^2 \tag{5.4}$$

where δt and Δt are the sample interval and the length of the signal, respectively, while $\phi(t)$ is the velocity signal.

5.2.2.3 Spectral entropy

In order to quantify the temporal flow instability in the velocity field of interest, the spectral entropy S_d is computed by a Proper Orthogonal Decomposition (POD) of the velocity [219]. The flow regimes can then be distinguished into stable or unstable flows based on spectral entropy. The relative energy in the aneurysm P_i is obtained from the corresponding eigenvalue λ_i, which quantifies the energy content of the i_{th} mode:

$$P_i = \frac{\lambda_i}{\sum_{j=1}^{N} \lambda_j} \tag{5.5}$$

where N is the total number of modes in the analysis.

The spectral entropy measures the average energy distributed in the aneurysm across the N modes, which can be used to quantify the stability of hemodynamic flows. The definition is as below:

$$S_d = -\sum_{i=1}^{N} P_i \ln P_i \tag{5.6}$$

Based on Eq. (5.6), the spectral entropy reaches its maximal value when the energy is evenly distributed over all the N modes. Entropy is minimized when the velocity signal contains only one single mode, meaning a steady flow ($S_d = 0$).

5.2.3 Numerical simulation

Simulations have been carried out using our in-house LBM solver ALBORZ, which has already been thoroughly validated using a variety of benchmark studies [30, 115, 220], as discussed in the previous chapters of this thesis. To make sure simulations are converging to the incompressible limit and keep computation costs as low as possible, the time-step size refinement follows an acoustic scaling resulting in a fixed CFL number, set to a low value of 0.052. Simulations have been carried out using three different resolutions (Low resolution (LR), Middle resolution (MR) and High resolution (HR)) in cases A and B, allowing to make

sure extracted results are converged physical data, as opposed to numerical artifacts such as Gibbs oscillations. For cases B, C, D and E, the highest resolutions (HR) are chosen to perform simulations.

Boundary conditions The inlet boundary conditions were configured with pulsatile velocity profiles, and the corresponding inflow velocity waveforms are depicted in Figure 5.2. The duration of each cardiac cycle is as follows: 1 s for cases A&B, 0.81 s for case C, 0.925 s

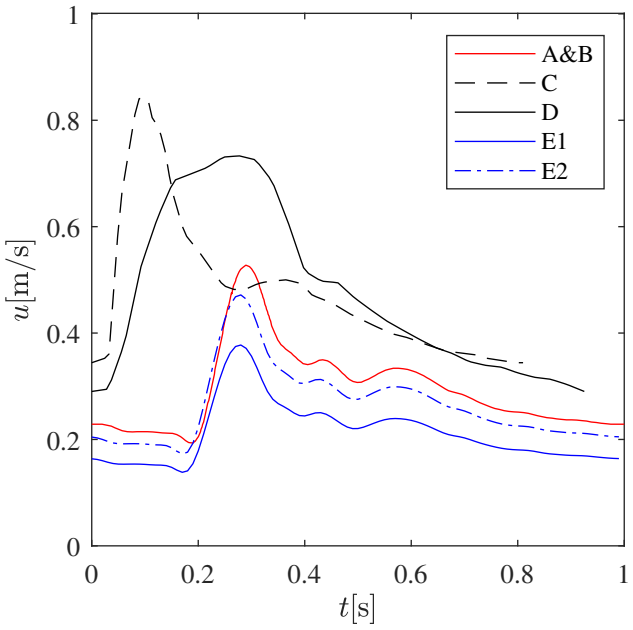

Figure 5.2: Illustration of the inflow velocity waveforms over an entire cardiac cycle imposed at the inlet of patients A&B (red), C (black dashed), D (black solid) and E (blue), respectively. Note that E1 and E2 indicate low and high inlet velocity profiles.

for case D and 0.99 s for case E (E1&E2), respectively. Additionally, constant pressure was prescribed as the boundary condition at all outlets, primarily due to the limited availability of pressure measurements at the outlet vessels or the lack of information regarding the correlation between flow rate and pressure in most cases. The vessel walls were assumed to be rigid, and no-slip boundary conditions were applied.

All results, with a focus on fluctuations, are now detailed in the next section.

5.3 Results

The following section presents qualitative and quantitative comparisons of hemodynamic simulations between ruptured (A, C, E) and unruptured cases (B, D), considering both Newtonian and non-Newtonian models

5.3.1 Impact of grid resolution on flow characteristics

In order to obtain accurate results while keeping acceptable computational costs, we first conducted a grid-independence study on case A and B considering Newtonian simulations. The grid size and time-step were varied simultaneously (keeping CFL number constant) from 260 μm down to 65 μm and from 7.6 μs to 1.9 μs, respectively.

As expected, the high-frequency fluctuations were found to be remarkably sensitive to both temporal and spatial resolutions. As shown in the top row of Figure 5.3, the low-resolution simulation (LR, blue lines) failed to capture any high-frequency fluctuation across the entire domain for both cases. Furthermore, it exhibited pronounced discrepancies when compared to velocity profiles acquired at higher resolutions for both aneurysms. Specifically, in both intermediate (MR, red lines) and high-resolution (HR, black lines) simulations, the noticeable high-frequency oscillations were evident under the exact conditions and at the same locations, specifically at points P3 to P9 within case A. However, these fluctuations are entirely absent in case B.

Still, minor discrepancies are still visible between MR and HR for case A at points P7 and P8, within the aneurysm sac. These discrepancies could be attributed partly to the fact that the monitoring points were fixed to the nearest grid points, causing a slight shift in actual position between resolutions. It is also possible that the resolution HR still has not reached complete grid-independence. However, it must be kept in mind that the central objective of this study is to detect high-frequency fluctuations in cases where they appear. In that regard, the outcomes derived from MR and HR simulations are fully identical, revealing such fluctuations at identical positions for the equivalent conditions and with similar spectra. Taking into account that the total computational load is high but still acceptable using High-Performance Computers for the highest resolution (HR), it was decided to maintain this resolution for the subsequent sections of this paper to optimize precision.

A similar conclusion can be drawn from the spectral analysis. The spectral profiles derived from both MR and HR simulations are nearly indistinguishable, as depicted in the bottom row of Figure 5.3. This alignment indicates a remarkably consistent flow behavior between the two. In contrast, the spectra from the lower resolution LR simulations reveal a reduced energy content in comparison to the higher resolution outcomes in patient A, signifying a relatively laminar flow pattern. It is worth noting that the energy level remains consistently lower across all three simulations in patient B, serving as evidence of a laminar flow configuration.

Therefore, the choice of an appropriate resolution significantly influences the acquisition of accurate data concerning high-frequency oscillations. Opting for a lower resolution might potentially lead to an underestimation of the impact of high-frequency fluctuations in clinical assessments.

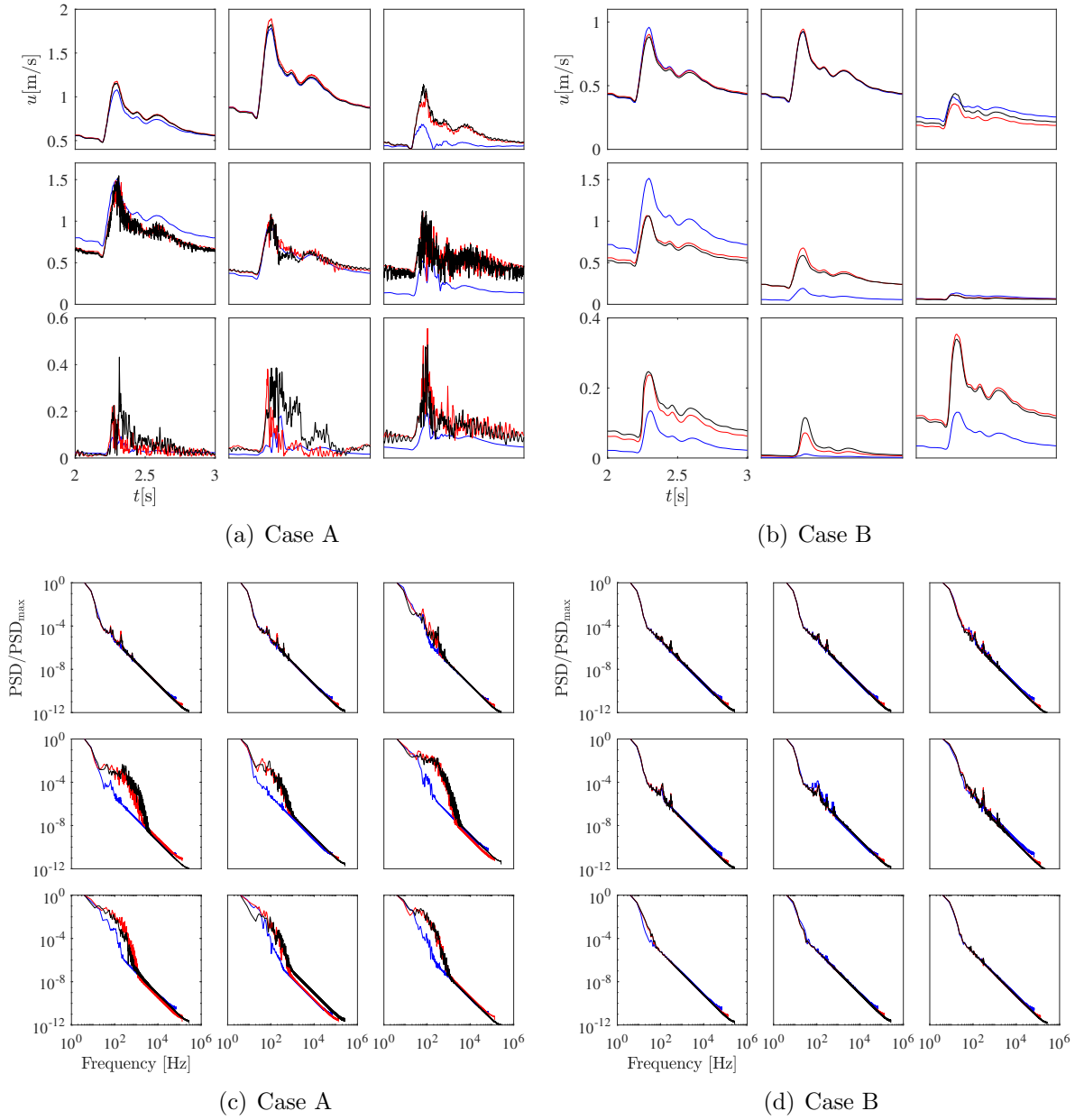

(a) Case A (b) Case B

(c) Case A (d) Case B

Figure 5.3: Time histories of the simulated velocity (top row) and corresponding energy spectra of the velocity distributions (bottom row) for patients A (left) and B (right) at nine monitoring points during the last cardiac cycle. The blue, red and black solid lines denote the flow velocity and energy spectra for increasing resolution (LR: low, MR: middle, and HR: high, respectively). From top left to bottom right in each quadrant, results at points P1 to P9 are shown.

5.3.2 Comparison of flow characteristics in the Newtonian scenario

Flow patterns within the aneurysm sac Figure 5.4 provides a qualitative comparison of flow streamlines within the aneurysm sac, offering insights into the dynamic behavior

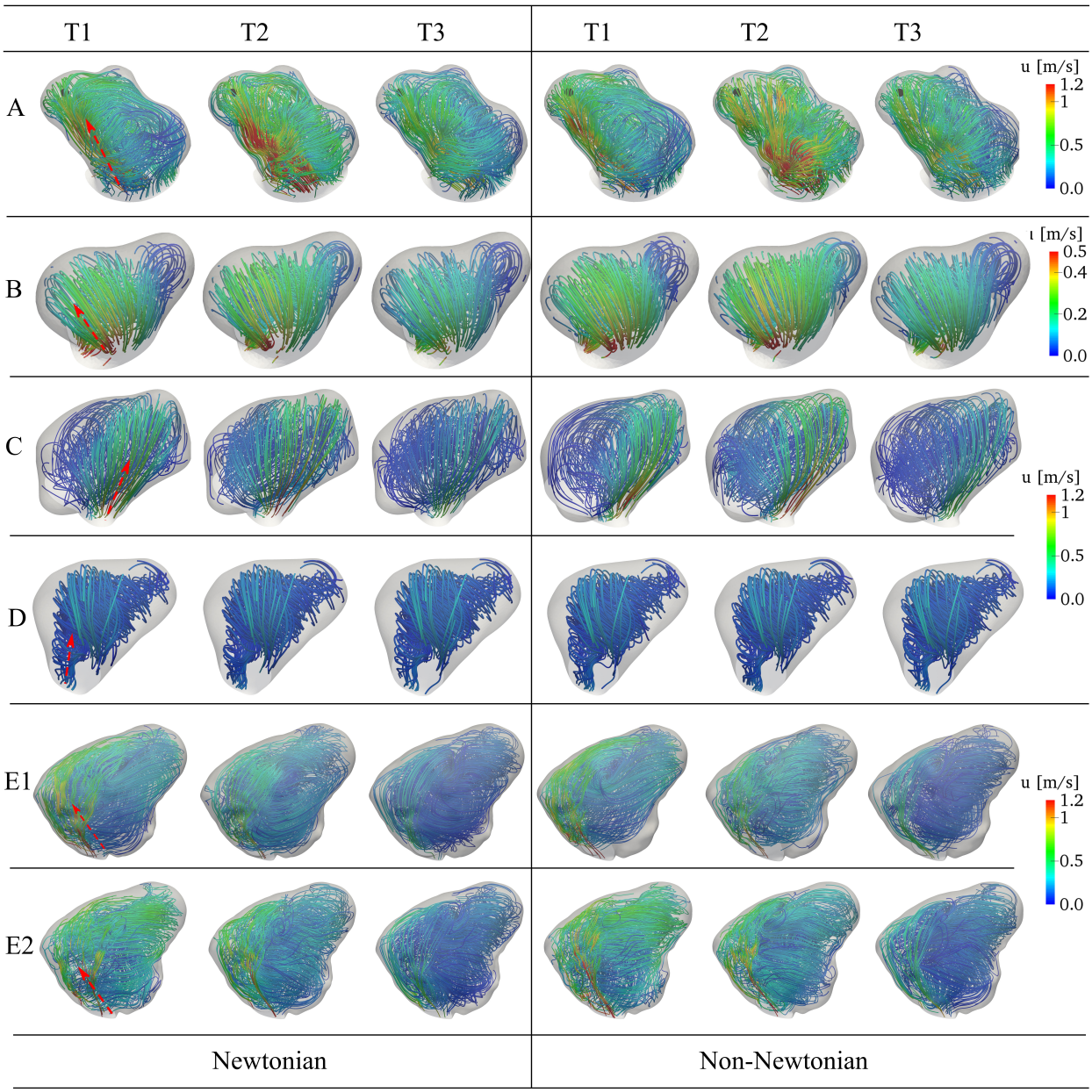

Figure 5.4: Flow streamlines colored by flow velocity inside the aneurysm sac for case A, B, C, D, and E (E1&E2) at the acceleration (T1), peak (T2), and deceleration (T3) systole, respectively. The black point and red arrow indicate the rupture location and high-speed jet, respectively. The left column of the figure shows results for the Newtonian model, right column corresponds to the non-Newtonian (Cross) model.

during different phases of the cardiac cycle (acceleration, peak systole, and deceleration phases). This illustration contrasts these flow streamlines under two distinct scenarios: one assuming Newtonian fluid behavior (left column) and the other considering non-Newtonian characteristics (right column).

The initial comparison reveals distinctions between flow streamlines in ruptured and unruptured cases. For the ruptured aneurysms (A, C, E), a concentrated high-speed jet originating from the parent vessel, striking the opposing wall at a specific angle, generates intricate vortical structures and disturbed flow patterns. In contrast, the unruptured cases (B, D) present a quite stable flow pattern characterized by a single large-scale vortex that persists consistently over all three cycles at the three selected time points. The flow streamlines within unruptured cases display a smoother and more laminar flow.

One further interesting observation that can be made here is that while Newtonian and non-Newtonian results are visually quite similar for the unruptured cases, they exhibit pronounced differences for the ruptured cases, also concerning large-scale flow structures. Corresponding effects will be discussed in more detail in a later section.

This first, qualitative analysis revealed a stronger flow with larger variations in time in the ruptured cases. Therefore, velocity fluctuations in time appear to play an important role and will be quantified in what follows.

Temporal velocity fluctuation To gain a more precise understanding of the occurrence and spatial distribution of flow fluctuations within the aneurysm sac, the findings should be further examined. Figure 5.3(a) shows the temporal variations of velocity, in particular at probe P6 in case A (remember that point P6 corresponds to the known rupture location in this case).

Firstly, it is important to note that discernible flow instabilities are absent in the parent artery (points P1&P2). Instead, flow fluctuations emerge initially at the bifurcation point (P3), and subsequently propagate throughout the entire sac and extend to the two outlets (points P4&P5). At bifurcation point P3, only subtle fluctuations are evident, primarily around the peak systole phase. Similar dynamics have been reported by Le et al. [221], where a highly dynamic inflow jet was observed in the ostium of intracranial aneurysms. Their findings, through dynamic mode decomposition analysis, highlighted that high-frequency modes, characterized by brief duration, corresponded to flow separation at the proximal neck and the impingement of the jet onto the aneurysm wall. Within the aneurysm sac (points P6 to P9), both the frequency and amplitude of flow fluctuations exhibit notable escalation (as evident in the second row of Figure 5.3). On the other hand, as the flow passes beyond peak systole, both the amplitude and frequency gradually decay, even if velocity instabilities persist over the entire cardiac cycle in part of the sac. Interestingly, these fluctuations are particularly pronounced during the deceleration phase of the cardiac cycle. This phenomenon can be attributed to the suppression of transition effects during the acceleration phase and their enhancement during the deceleration phase, as also observed in pulsating flows in straight tubes [222].

To better study the velocity fluctuations at the rupture point (P6), one cardiac cycle was divided into three distinct phases (2-2.2 s, 2.2-2.8 s, 2.8-3.0 s, see Figure 5.5), facilitating the analysis. Examining the top row of the plot, at the commencement of the cardiac cycle (left subfigure), fluctuations appear uniform and the average velocity hovers around 0.4 m/s.

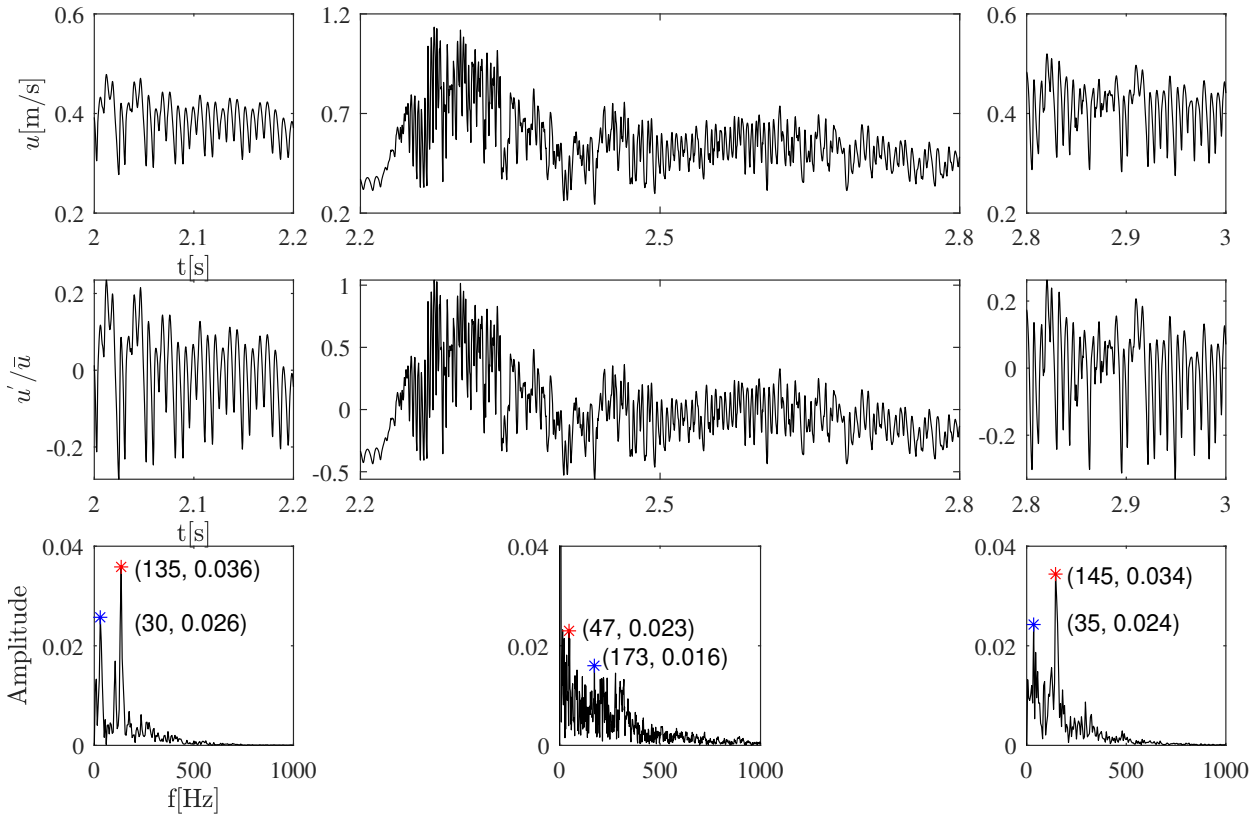

Figure 5.5: Time history of velocity (top), normalized fluctuating velocity (center), and FFT of velocity (bottom) at point P6 in case A during the last cardiac cycle (from 2 to 3 s from left to right), considering blood as a Newtonian fluid. Note that the figures in the two top rows use different vertical scales for a better readability. The red and blue stars in the bottom row indicate the first and second dominant frequencies.

Subsequently, substantial fluctuations manifest after peak systole, driving the maximum velocity to almost 1.2 m/s. In the final phase, the flow instability diminishes toward the end of the deceleration phase, transitioning into low-frequency fluctuations with an average velocity of approximately 0.4 m/s (right figure), closely resembling the flow characteristics observed at the start of the cardiac cycle (compare left and right subfigures).

The middle row exhibits the normalized fluctuating velocity profile over time. It reveals that the relative amplitude of the velocity fluctuations is roughly 20% during the early and late phases of the cardiac cycle, increasing significantly to around 100% during peak systole.

The bottom row depicts the fast Fourier transform (FFT) of the fluctuating velocity signal. This analysis indicates that the dominant frequencies (represented by red stars) are approximately 140 Hz during both the early and late phases of the cardiac cycle. During peak systole, the frequency spectrum becomes more complex, with multiple frequencies participating and the FFT signal becoming highly populated, indicative of the onset of turbulent conditions. In this phase, the dominant frequency is roughly 47 Hz, accompanied by

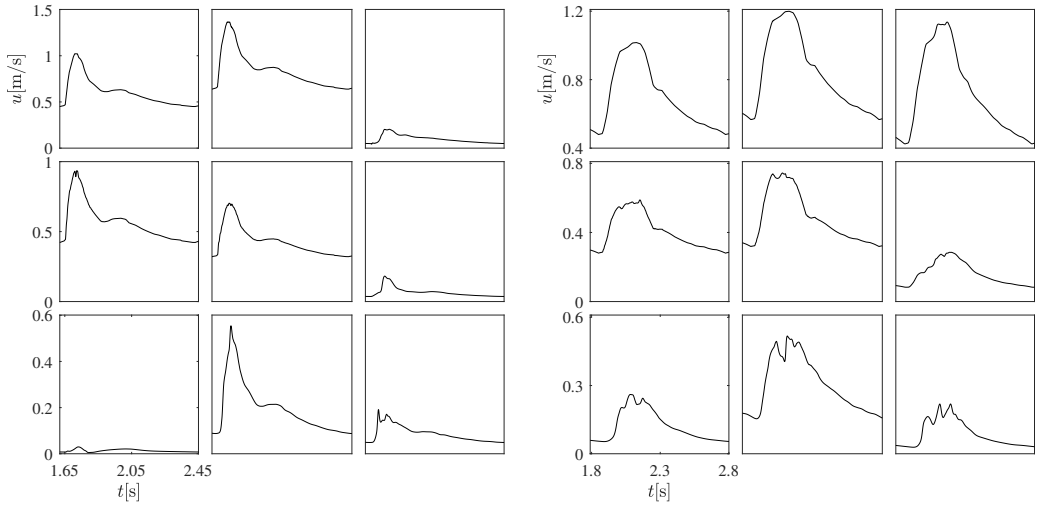

(a) Case C (b) Case D

Figure 5.6: Time histories of the simulated velocity in case C and D at nine monitoring points during the last cardiac cycle. From top left to bottom right, results at points P1 to P9 are shown.

a secondary peak at 173 Hz. The lower-frequency fluctuation observed here may possibly be attributed to cycle-to-cycle fluctuations arising as the flow decelerates, a phenomenon previously documented in studies [212, 223].

Moving on to cases C and D in Figure 5.6(b), a closer examination of the velocity profiles reveals a notable trend. In the nine monitored points within the sac, only minimal fluctuations can be observed. These fluctuations are nearly negligible, strongly implying the prevalence of laminar flow patterns in these cases.

5.3.3 Fluctuating kinetic energy

A more in-depth analysis of cases A and E is conducted by calculating FKE. As demonstrated in Figure 5.7, the distribution of FKE at the monitoring points in ruptured cases (A and E1) offers valuable insights. Notably, the time evolution of FKE within the parent artery (points P1&P2) remains consistently at zero for both cases. This absence of FKE aligns with the smooth velocity profiles and absence of discernible fluctuations in these regions. Furthermore, the peaks of maximum FKE primarily occur during peak systole in both cases. However, uniquely in case A, distinct fluctuations are also observed at the rupture site (P6) during late systole, with the second-highest peak reaching $\sim 1 \times 10^{-4}$ m^2/s^2. This value surpasses the overall peak FKE at all other points both within and outside the aneurysm sac. Interestingly, the highest level of FKE also occurs at P6 in case E1 (orders of magnitude larger, $\sim 6 \times 10^{-5}$ m^2/s^2).

At the bifurcation point P3 of case A, a low level of FKE ($\sim 2 \times 10^{-6}$ m^2/s^2) emerges during peak systole, revealing the initiation of flow instability. In contrast, FKE at this juncture

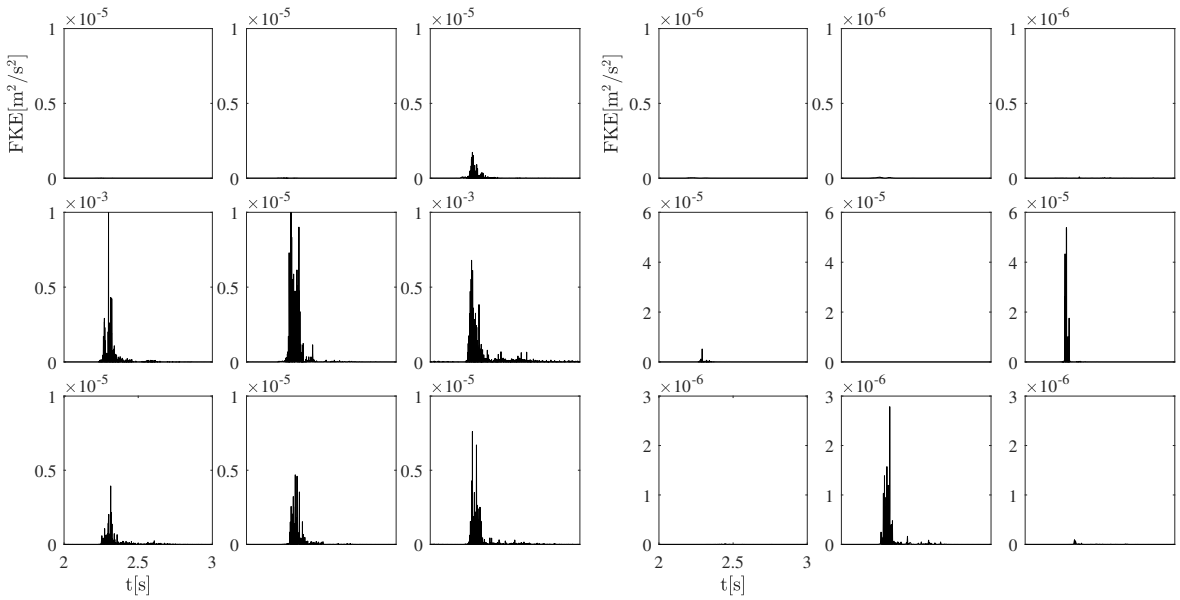

(a) Case A (b) Case E1

Figure 5.7: Time evolution of FKE in the cases A and E1 at all monitoring points during the last cardiac cycle, considering blood as a Newtonian fluid. From top left to bottom right, results at points P1 to P9 are shown. Note the different vertical scales.

in case E1 remains at negligible levels. At the outlets, remarkably pronounced fluctuations are also apparent, with a noteworthy disparity in FKE between both outlets in case A. This variance can potentially be attributed to the specific geometry of the ruptured aneurysm and vessel tree configuration. It is noteworthy that the flow rate exiting through the outlet associated with P4 greatly surpasses that of the outlet containing P5. Minor fluctuations are also discernible at the outlet of case E, with FKE at approximately $\sim 5 \times 10^{-5}$ m^2/s^2 while the FKE level is zero in the other outlet (P5).

The remaining points within the aneurysm sac of case A (points P7, P8, P9) exhibit lower FKE values compared to the other monitoring points. At the start and conclusion of the cardiac cycle, FKE effectively diminishes to near zero in these areas. Likewise, FKE values at points P5, P7, P9 in case E1 also converge to zero. However, at point P8, the FKE level remains around $\sim 3 \times 10^{-6}$ m^2/s^2.

Overall, these distinctive features of FKE suggest that intensive flow instability, as measured by FKE, may serve as a characteristic hallmark of the potential rupture location within the aneurysm sac.

5.3.4 Power spectral density

Figure 5.8 shows the energy spectra of flow velocity at the designated monitoring points for cases A, B, C, and D. Notably, within the aneurysm sac, the PSD of case A (depicted in red) consistently ranks the highest in comparison to the other cases. Case A shows distinctive

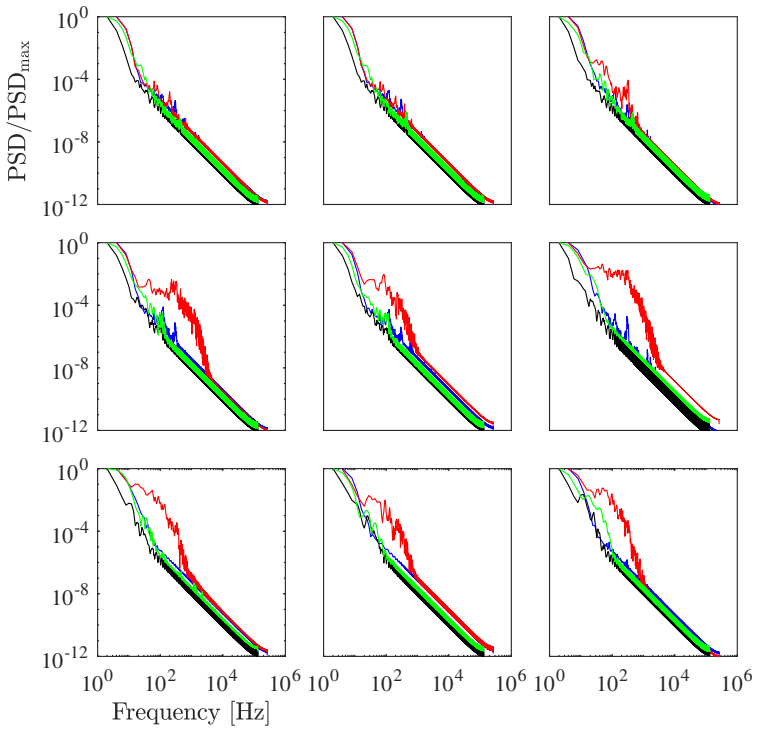

Figure 5.8: Energy spectra of velocity in case A (red), case B (blue), case C (green) and case D (black) at the 9 monitoring points during the last cardiac cycle, considering blood as a Newtonian fluid. From top left to bottom right, results at points P1 to P9 are shown.

spectral characteristics indicative of turbulent-like flow with pronounced fluctuations. A notable and expansive rise in PSD is discernible around the approximate frequency of 100 Hz. This unique behavior is consistent across all points from P4 to P9 and within the aneurysm sac. Conversely, the PSD of the flow velocity for cases B, C, and D reveal a nearly monotonic decline relative to frequency, devoid of prominent peaks. Overall, the simulation outcomes unequivocally affirm that the flow in case A exhibits distinct spectral traits divergent from the other cases, particularly conspicuous at the rupture point P6. At this specific location, a clear frequency peak emerges at approximately 120 Hz prior to and subsequent to peak systole, hinting at the potential significance of high-frequency features in the context of aneurysm rupture.

5.3.5 Spectral entropy analysis

The analysis based on spectral entropy S_d is able to deliver a single, scalar value characterizing the state of an unsteady, 3D flow (as found here). The lowest possible value of S_d (i.e., 0) corresponds to laminar conditions. Previous investigations have shown that transition occurs around $S_d \approx 1$ (see previously cited studies for more detailed values). Here, the values of S_d are compared 1) between ruptured and unruptured aneurysms, and 2) using either Newtonian or non-Newtonian viscosity models. The results are summarized in Table 5.2. The obtained values of S_d show that the ruptured intracranial aneurysm A exhibits significantly

Table 5.2: Summary of the values of spectral entropy computed in all cases in Newtonian or non-Newtonian scenario.

Case	S_d (Newtonian)	S_d (non-Newtonian)	Flow regime
A	1.16	1.50	Unstable / Unstable
B	0.10	0.12	Stable / Stable
C	0.22	0.24	Stable / Stable
D	0.30	0.34	Stable / Stable
E1	0.52	0.55	Stable / Stable
E2	0.54	0.63	Stable / Stable

higher spectral entropy compared to the other cases, corresponding to an unstable flow state with strong fluctuations. The value of S_d for the ruptured case A is approximately 10 times

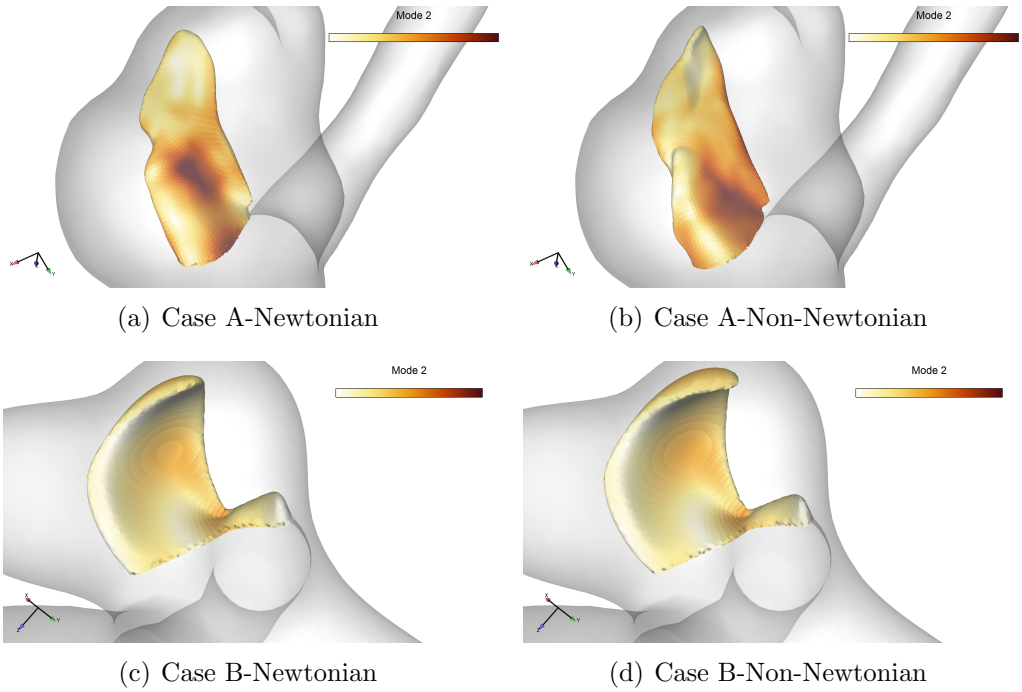

(a) Case A-Newtonian (b) Case A-Non-Newtonian

(c) Case B-Newtonian (d) Case B-Non-Newtonian

Figure 5.9: Hybrid visualization (based on [9]) of the isosurface obtained with the help of the first POD mode, but colored by the second POD mode for both aneurysms A (top, ruptured) and B (bottom, unruptured) with either Newtonian (left) or non-Newtonian models (right).

larger than for the very stable flow found in the unruptured aneurysm B ($S_d \approx 0.1$). This shows that spectral entropy can safely be used to delineate between stable and unstable flow configurations in intracranial aneurysms, as already discussed by Cebral and co-workers [224] and Janiga [225]. Additionally, it is observed that the spectral entropy increases by approximately 20% in cases (A, B, C, D) when a non-Newtonian model is applied. However, this does not change the predicted flow state (stable for unruptured aneurysm B; unstable for ruptured aneurysm A) in the present cases. In case E, a roughly 20% increased spectral en-

tropy is observed with the rise in the inlet flow rate in both Newtonian and non-Newtonian cases. Despite the increase in spectral entropy, they still fall into a stable flow regime.

Figure 5.9 illustrates a combined qualitative illustration of the first two most energetic POD modes in ruptured (A) and unruptured (B) aneurysms as suggested by [9]. The temporal averaged flow information is represented by the first POD mode, therefore, it can effectively characterize the primary flow. It can be observed that the jet flow to the aneurysm sac has a higher velocity in the ruptured case A compared to the unruptured aneurysm B.

The second POD mode represents the secondary flow structures, which can be used to demonstrate the temporal variation of the blood flow. The higher POD modes are generally not straightforward to interpret physically. In Figure 5.9, the second mode is used to color-code the isosurface obtained from the first POD mode. The dark colors indicate stronger secondary flow features. The lighter colors associated with lower secondary flow features symbolize a stable flow throughout the cardiac cycle. This qualitative combined visualization of the first two POD modes enables the identification of high or low areas in the secondary flow and can efficiently help analyzing the complexity of the hemodynamics.

5.3.6 Effect of non-Newtonian behavior

The preceding discussion has predominantly rested on the assumption of Newtonian blood behavior. Despite real blood being recognized as non-Newtonian and shear-thinning, the relevance of these non-Newtonian characteristics has often been overlooked in prior studies, as discussed in the previous chapter. Our recent investigations, e.g. [226] have delved into the impact of non-Newtonian behavior on the flow distribution within aneurysms. The findings indicate that the adoption of a non-Newtonian model significantly influences the flow field, particularly within the aneurysm sac and in proximity to its walls, given the prevalence of low shear rates across substantial portions of the sac.

In Figure 5.4, the streamlines have been qualitatively compared between Newtonian and non-Newtonian cases among these aneurysms, revealing evident distinctions in the ruptured case. A further comparison of velocity fluctuations between ruptured and unruptured cases is presented in Figure 5.10. In cases B, C, and D, the non-Newtonian model displays only a small impact, as indicated by nearly overlapping black and red curves. However, in case A (rupture), very strong differences emerge, particularly at point P8 within the sac. High-frequency fluctuations are absent in case B (unruptured), regardless of the fluid behavior assumption. The situation contrasts significantly in case A where the impact of the non-Newtonian model is negligible in the parent artery (points P1& P2) and at the neck (P3) while the velocity fluctuations are much stronger when considering a non-Newtonian behavior, particularly at point P6 and point P8. Similar tendencies are evident in case E1 (also ruptured), where the non-Newtonian model substantially impacts points P6 and P8.

Comparing Case C (ruptured) and Case D (unruptured), the differences induced by the non-Newtonian fluid model are also larger in the former, in particular at point P8, even if they remain small.

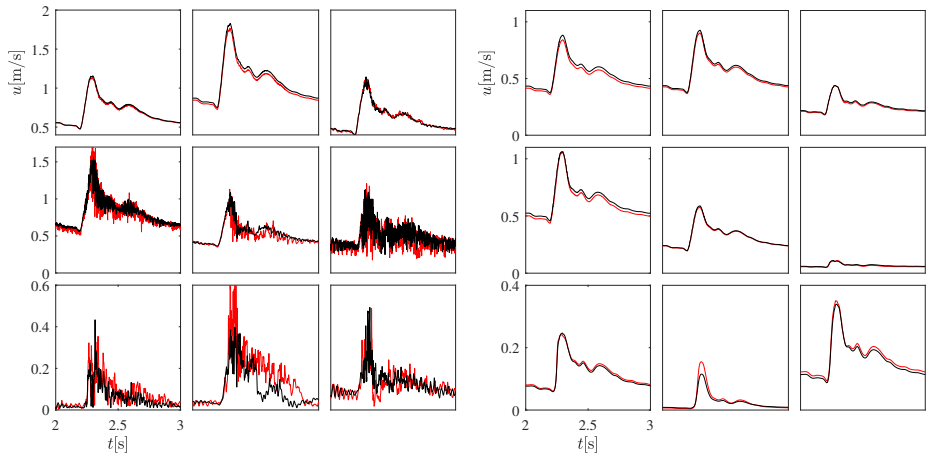

(a) Case A

(b) Case B

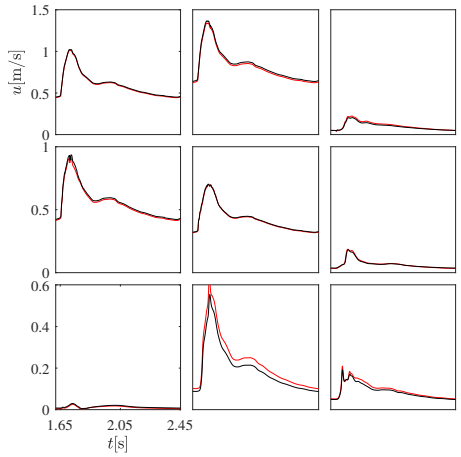

(c) Case C

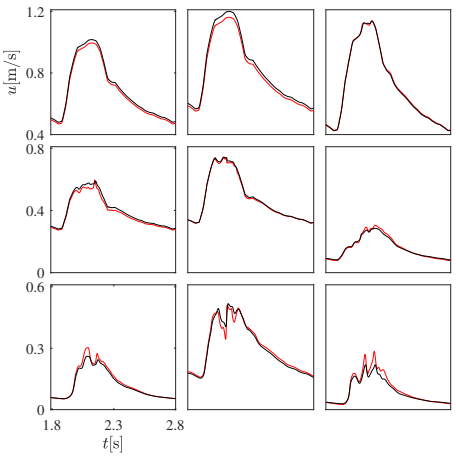

(d) Case D

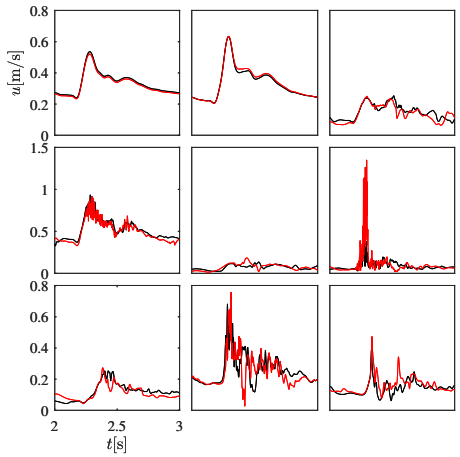

(e) Case E1

Figure 5.10: Velocity over time in case A, B, C, D and E at the nine monitoring points during the last cardiac cycle. The black and red solid lines denote the velocity magnitude computed using a Newtonian or a non-Newtonian (Cross) model, respectively. From top left to bottom right in each block, results at points P1 to P9 are shown. Note the different vertical scales.

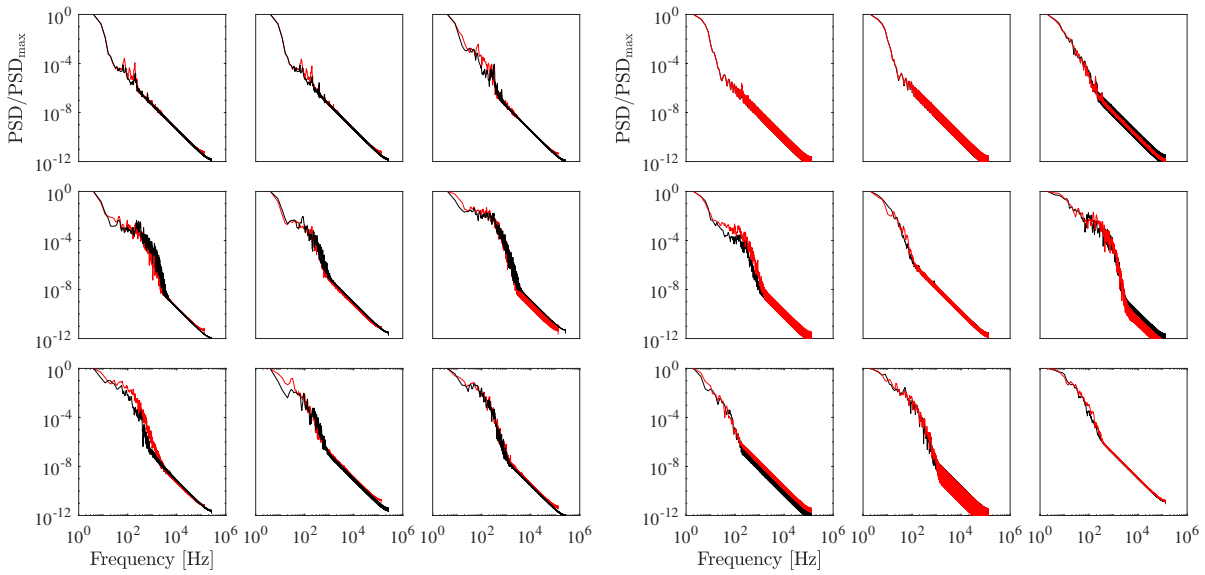

(a) Case A (b) Case E1

Figure 5.11: Energy spectra of the velocity over frequency in the case A and E1. The black and red solid lines denote the energy spectra computed using a Newtonian or a non-Newtonian (Cross) model, respectively. From top left to bottom right, results at points P1 to P9 are shown.

Figure 5.11 presents the energy spectra of the velocity in two ruptured cases (A&E1), unveiling higher energy levels in the non-Newtonian model compared to the Newtonian counterpart. These outcomes again suggest that a non-Newtonian fluid behavior may amplify flow instability. Additionally, the local shear rate at the various monitoring points among these cases is shown in Figure 5.12, investigating the potential impact of the different viscosity models. In the unruptured cases (B&D), the evolution of the shear rates exhibit similar trends under both Newtonian and non-Newtonian considerations, with peak systole-associated relative differences below 25%. Although high-frequency fluctuations are not observed in case B, there are weak velocity fluctuations within the sac in case D. Furthermore, the shear rates are quite small and stay below 1000 s^{-1} at most of the points.

In the ruptured cases (A, C & E1), this correlation holds also true within the cerebral artery preceding the aneurysm (points P1&P2). The shear rate fluctuations remain modest at the bifurcation point (P3), yet very considerable fluctuations are observable at points P4 to P9 in cases A and E1. The peak shear rate even exceeds 4000 s^{-1} at point P6 and reaches 1500 s^{-1} at peak systole at the outlet P4 in both cases. This finding confirms the presence of significant velocity variations at these two points. However, Case C (also ruptured) shows no significant difference to Case D (unruptured). The findings of the present study certainly depend on the specific configuration considered and must be confirmed by involving even more cases in the analysis.

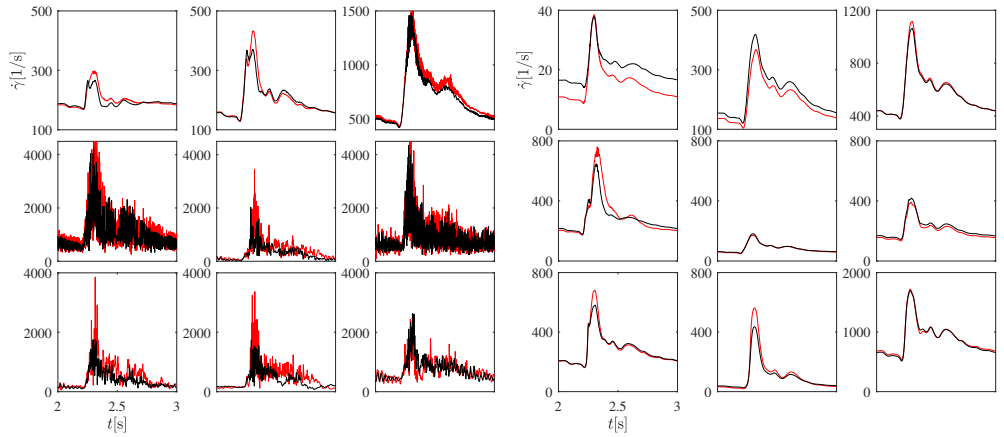

(a) Case A

(b) Case B

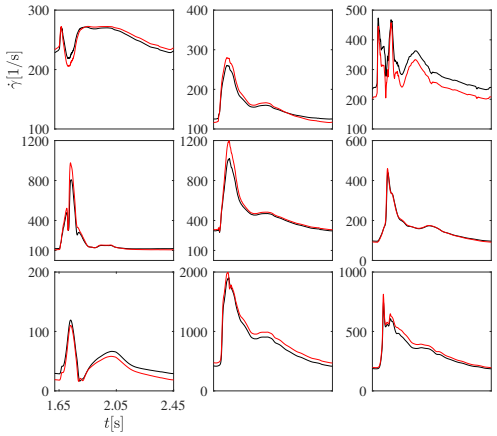

(c) Case C

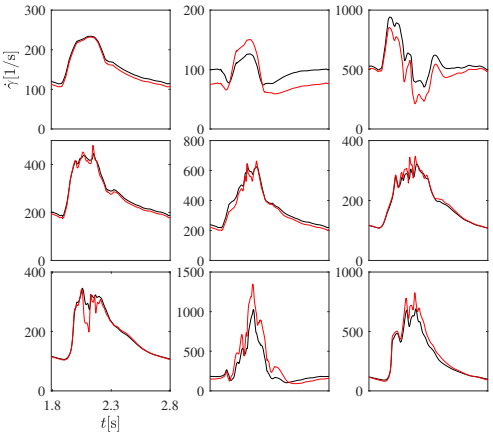

(d) Case D

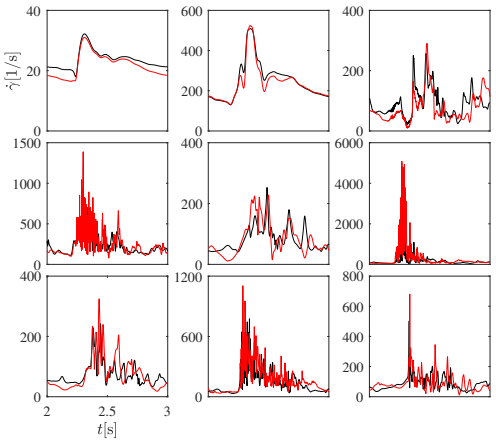

(e) Case E1

Figure 5.12: Shear rate over time in cases A, B, C, D and E1 at the nine monitoring points during the last cardiac cycle. The black and red solid lines denote the shear rate computed using a Newtonian or a non-Newtonian (Cross) model, respectively. From top left to bottom right in each block, results at points P1 to P9 are shown. Note the different vertical scales.

In conclusion, the non-Newtonian model generally tends to induce higher amplitudes of shear rate fluctuations, with notable differences observed at specific points. Unexpectedly, this does not really apply to the rupture point P6 in case A, P6. Here, large fluctuations are observed, but at a very similar level for the Newtonian and the non-Newtonian fluid model. Further investigations will be necessary to check this observation.

5.3.7 Effect of flow rate

Figure 5.13 illustrates the evolution of velocity magnitude, PSD over frequency, shear rate over time, and FKE over time for case E under two distinct inlet flow rates (low: E1; high: E2). This figure shows that an increase in the inlet velocity profile leads to enhanced velocity fluctuations regarding both intensity and frequency. At point P6, the disparity can be as substantial as threefold for FKE. While the PSD profile shows a relatively weak content in terms of frequencies, noticeable fluctuations emerge in particular in the shear rate profile, as also confirmed by FKE. These fluctuations are evident not only at point P6 but also at the other points within the entire sac. The FKE profile reveals maximal velocity fluctuation at P6 and P8, attaining values of 4×10^{-4} and 6×10^{-6} m^2/s^2, respectively.

Comparing the outcomes between low and high inlet velocities, it becomes apparent that elevated inlet velocity serves to magnify fluctuations, potentially contributing to an augmented risk of aneurysm rupture. This observation underscores the significance of using a realistic inlet flow rate due to its influence on flow dynamics within the aneurysm, ultimately with strong potential implications for rupture susceptibility.

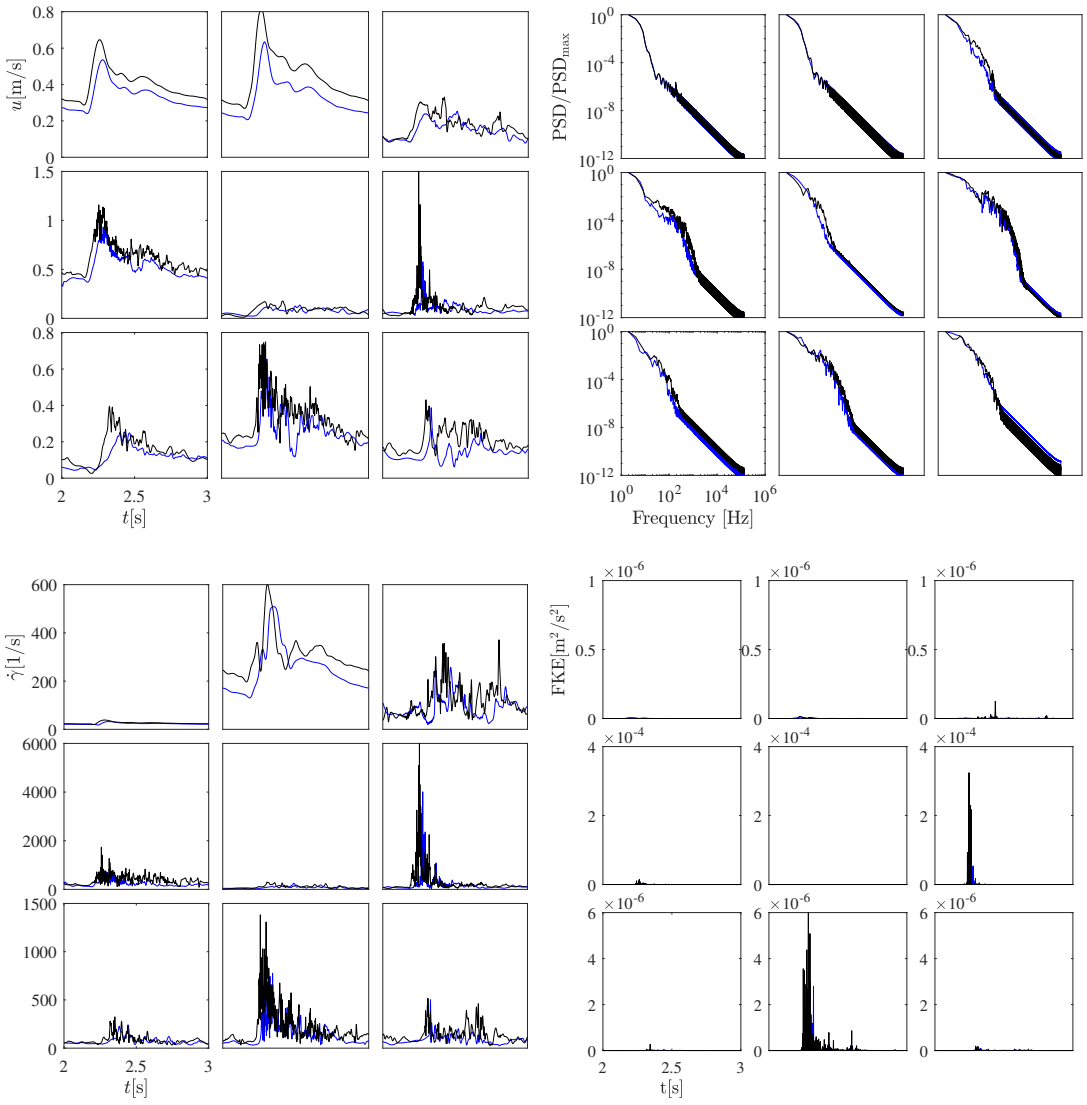

Figure 5.13: Evolution of (top left) velocity magnitude over time, (top right) PSD over frequency, (bottom left) shear rate over time, and (bottom right) FKE over time in case E with two different flow rates at the nine monitoring points during the last cardiac cycle. The blue and black solid lines denote simulation results employed with low (E1) or high (E2) inlet flow rates, respectively. From top left to bottom right in each block, results at points P1 to P9 are shown. Note the different vertical scales.

5.4 Conclusions and discussion

In conclusion, this comparative study provides valuable insights regarding hemodynamic characteristics among ruptured and unruptured, patient-specific intracranial aneurysms. the findings drawn from the aforementioned analysis indicate that high-frequency fluctuations can in general be identified within ruptured intracranial aneurysms. This observation aligns qualitatively with earlier computational investigations of intracranial aneurysms, such as the

work conducted by Varble et al. [227] and more recent works on that topic, e.g. [228, 229]. However, it is worth noting that the presence of high-frequency fluctuations may not be a consistent characteristic of all rupture cases, as seen for configuration C.

Additionally, these findings also suggest that a high level of spatial and temporal resolution is required to investigate high-frequency fluctuations possibly occurring in such configurations; using a coarser grid and a large time step leads to increased numerical dissipation and damps artificially the onset of flow instability.

Furthermore, these investigations also demonstrate that non-Newtonian models may have a very large impact on shear rate at specific locations, particularly around peak systole. This appears to be even more important in ruptured aneurysms. However, the exact rupture point is unexpectedly almost not affected by the shear rate – so that further studies involving additional configurations will be needed to clarify the picture. Still, it cannot be assumed that the shear rate will exceed 100 s^{-1} at all locations and at all times, so that using a suitable non-Newtonian model is recommended to be on the safe side; this might be particularly important when assessing flow instability in patient-specific aneurysms.

Several limitations should be mentioned in connection with the present study. The first one is obviously the very limited number of configurations considered – only three ruptured and two unruptured cases. It is well known that aneurysm size, shape, location, the ratio of size and neck... will affect hemodynamics and aneurysm rupture. A much larger number of patient-specific configurations must be considered in future studies. Secondly, all vessels have been assumed to be rigid. Clearly, the obtained findings might be modified when taking into account fluid-structure interactions; however, this would only be possible when having a detailed knowledge of wall resistance and structure, which is extremely challenging [230, 231]. Nonetheless, it is important to acknowledge that uncertainties remain regarding the existence of fluctuations when the number of monitored points is increased. Further investigation and analysis would be required to ascertain whether fluctuations are found at additional monitoring points across the entire sac.

Finally, it is worth noting that the interplay between hemodynamic factors and biological processes regarding aneurysm formation and rupture remain poorly understood. Best-practice rules are needed for the assessment of aneurysm hemodynamics using numerical simulations, in order to support more robust and reliable comparisons among studies [217, 232, 233]. Ultimately, this would open the door for an efficient support of clinicians, possibly leading to highly personalized, optimized treatment options.

Chapter 6

Conclusions and Outlook

Contents

6.1 Conclusions

This thesis was centered on the validation and application of our in-house numerical solver, based on LBM, for the simulation of medical flows, with a primary focus on investigating the hemodynamics within aneurysms. The research encompassed various numerical simulations, ranging from idealized aneurysm models to complex patient-specific cases and standard benchmark scenarios. The following key conclusions and achievements have emerged:

- We successfully developed and integrated shear-thinning non-Newtonian models (including Power law, Carreau-Yasuda, and Cross models) for the first time into our solver. In this manner it becomes possible to capture in a realistic manner the non-Newtonian behavior of blood. The outcomes of our simulations underscore the substantial impact of the chosen viscosity model on the flow field, particularly within the aneurysm sac, where the differences were pronounced both near the center and close to the walls. This work demonstrated the robustness of our numerical model, enabling systematic investigations into non-Newtonian effects across diverse types of cerebral aneurysms. This offers valuable insights into the role and significance of non-Newtonian behavior in these complex flows.
- The study delved into the occurrence of flow fluctuations, contrasting Newtonian and non-Newtonian fluid models in patient-specific intracranial aneurysms using high-resolution lattice Boltzmann simulations. The quantification of flow instabilities through various metrics, including power spectral density, proper orthogonal decomposition, spectral entropy, and fluctuating kinetic energy of velocity fluctuations, led to critical insights. Specifically, our findings unveiled hydrodynamic instabilities in the pulsatile inflow through the neck of two ruptured aneurysms, manifesting as high-frequency fluctuations around the rupture location throughout the entire cardiac cycle.

This research has extended our understanding of hemodynamics in intracranial aneurysms, shedding light on the transition to weakly turbulent flows within these critical medical conditions. The implications of these findings are far-reaching, as they offer insights into the pathophysiology of aneurysm rupture and hold promise for the development of medical devices to mitigate such flow instabilities. It is imperative to note that the accurate assessment of these occurrences necessitates a substantial commitment to high spatial and temporal resolutions in patient-specific aneurysm simulations. This work contributes significantly to the broader field of computational hemodynamics, with potential applications in clinical practice and medical device design at a later stage.

6.2 Principal limitations

The limitations of this study have been discussed in detail throughout each chapter, and are summarized here:

- **Limited Cohort of Patient-Specific Aneurysms:** One generic limitation is the relatively small cohort of patient-specific aneurysms that were studied. To draw more

robust conclusions regarding the presence of transitional flows in aneurysms, a larger and more diverse dataset would be beneficial. A larger cohort would provide a more comprehensive understanding of the factors influencing transition and flow instabilities. Moreover, the inclusion of aneurysms with varying morphological and geometrical characteristics would add depth to the analysis.

An expanded dataset would not only enhance the statistical strength of our findings but also allow us to delve into the vast diversity of aneurysm shapes, sizes, and locations. These individual characteristics are known to significantly impact hemodynamics and, by extension, the risk of rupture. Therefore, future research should strive to incorporate a more extensive array of patient-specific cases to account for this variability.

- **Exclusion of Aneurysm Wall Movement and Properties:** Another notable limitation is the omission of any movement or biological degradation of the aneurysm wall in the context of fluctuating or pulsatile flow within aneurysm sacs. Previous research, such as Zimny's work [234], has identified discernible effects of wall motion on wall shear stress in aneurysms and has proposed potential consequences of this aspect on thrombus formation. It is reasonable to assume that the interaction between hemodynamics and the aneurysm wall, considering its movement, would have a significant impact on transitional hemodynamics. The intensity of these hemodynamic fluctuations may, in turn, be influenced by the behavior of the aneurysm wall.

  The study of transitional flow is inherently linked to the complex interplay between blood flow and the aneurysm wall. Future investigations should aim to bridge this gap by incorporating fluid-structure interaction (FSI) models. FSI simulations can provide a more comprehensive understanding of how the dynamic behavior of the aneurysm wall affects transitional hemodynamics. This will pave the way for more accurate risk assessments and treatment strategies.

- **Multi-Modal Data Fusion:** While the unavailability of 4D MRI-based patient-specific inflow profiles is in general a current limitation, future research should explore methods for obtaining and incorporating such data. This step would enhance the realism and precision of computational simulations. Additionally, future work should focus on establishing clear links between transitional flow patterns and clinical outcomes, particularly the prediction of aneurysm rupture.

  Combining various data sources, including patient-specific imaging, computational simulations, and clinical outcomes will provide a holistic perspective on aneurysm dynamics and the transition to rupture, ultimately guiding optimal and even safer medical decisions.

6.3 Perspectives

While this thesis has explored several patient-specific cases, the sample size remains limited due to computational constraints. In the future, we aim to expand our research by devel-

oping a numerical procedure capable of simulating a broader range of patient-specific cases with high accuracy. This expansion will enable us to analyze hemodynamics across a larger dataset, providing a more comprehensive understanding of aneurysm behavior. Additionally, we plan to extend our investigations to include numerical simulations involving stents placed within aneurysms. This will allow us to assess the effectiveness of different medical devices already used or under development for aneurysm treatment and seek opportunities for optimization or explore new geometric configurations.

Furthermore, a significant avenue for future research involves the simulation of thrombosis within patient-specific aneurysms. Hemostasis, the complex process involving various biochemical and hemodynamic factors leading to thrombus formation [235], is a topic closely related to aneurysms. Despite extensive study, the intricate mechanisms and coagulation pathways that underlie thrombus formation and growth continue to challenge medical research. Blood components, including both inactive and active platelets and red blood cells, along with a multitude of chemical species such as pro- and anti-coagulant proteins, contribute to the complexity of this phenomenon.

Our numerical tool encompasses solvers for the flow field, species, and energy fields, based on methods combining the lattice Boltzmann method with finite differences. This tool has already demonstrated its utility on large parallel clusters and exhibits excellent scalability. Our future work will initially involve modeling simple configurations using reaction networks available in the literature [236, 237]. We will assess different bioreaction schemes, transport models, and adhesion models for platelets found in the literature by incorporating them into our simulations, utilizing the thermo-chemistry library REGATH available within ALBORZ. These models will be used to simulate academic test-cases based on in-vitro experimental studies from existing literature. Subsequently, we will apply the most suitable models, including chemical schemes and platelet transport models, to more complex patient-specific geometries, advancing our understanding of thrombosis within aneurysms.

In summary, the future work will focus on expanding our dataset of patient-specific cases, exploring the role of stents, and advancing our understanding of thrombosis within aneurysms. This research will contribute to the field of hemodynamics and improve the assessment and treatment of aneurysms.

Bibliography

[1] L. Heimer. *The human brain and spinal cord: functional neuroanatomy and dissection guide*. Springer Science & Business Media, 2012.

[2] F. Gaidzik, D. Stucht, C. Roloff, O. Speck, D. Thévenin, and G. Janiga. Transient flow prediction in an idealized aneurysm geometry using data assimilation. *Computers in Biology and Medicine*, 115:103507, 2019.

[3] Q. Li, N. Hong, B. Shi, and Z. Chai. Comparison of intracranial aneurysm flow quantification techniques: standard PIV vs stereoscopic PIV vs tomographic PIV vs phase-contrast MRI vs CFD. *Journal of Neurointerventional Surgery*, 11(3):275–282, 2019.

[4] D. A. Steinman, Y. Hoi, P. Fahy, L. Morris, M.T. Walsh, N. Aristokleous, A. S. Anayiotos, Y. Papaharilaou, A. Arzani, S. C. Shadden, et al. Variability of computational fluid dynamics solutions for pressure and flow in a giant aneurysm: the ASME 2012 Summer Bioengineering Conference CFD Challenge. *Journal of Biomechanical Engineering*, 135(2), 2013.

[5] J. R. Cebral, F. Mut, M. Raschi, E. Scrivano, R. Ceratto, P. Lylyk, and C. M. Putman. Aneurysm rupture following treatment with flow-diverting stents: computational hemodynamics analysis of treatment. *American Journal of Neuroradiology*, 32(1):27–33, 2011.

[6] Q. Li, N. Hong, B. Shi, and Z. Chai. Simulation of power-law fluid flows in two-dimensional square cavity using multi-relaxation-time lattice Boltzmann method. *Communications in Computational Physics*, 15(1):265–284, 2014.

[7] P. Neofytou. A 3rd order upwind finite volume method for generalised newtonian fluid flows. *Advances in Engineering Software*, 36(10):664–680, 2005.

[8] B. C. Bell and K. S. Surana. p-version least squares finite element formulation for two-dimensional, incompressible, non-newtonian isothermal and non-isothermal fluid flow. *International journal for numerical methods in fluids*, 18(2):127–162, 1994.

[9] G. Janiga. Novel feature-based visualization of the unsteady blood flow in intracranial aneurysms with the help of proper orthogonal decomposition (POD). *Computerized Medical Imaging and Graphics*, 73:30–38, 2019.

[10] World Health Organization. *The world health report 2002: reducing risks, promoting healthy life*. World Health Organization, 2002.

[11] A. Quarteroni, M. Tuveri, and A. Veneziani. Computational vascular fluid dynamics: problems, models and methods. *Computing and Visualization in Science*, 2(4):163–197, 2000.

[12] M. H. Vlak, A. Algra, R. Brandenburg, and G. J. E. Rinkel. Prevalence of unruptured intracranial aneurysms, with emphasis on sex, age, comorbidity, country, and time period: a systematic review and meta-analysis. *The Lancet. Neurology*, 10(7):626–636, 2011.

[13] A. I. Karttunen, P. H. Jartti, V. A. Ukkola, J. Sajanti, and M. Haapea. Value of the quantity and distribution of subarachnoid haemorrhage on CT in the localization of a ruptured cerebral aneurysm. *Acta Neurochirurgica*, 145:655–661, 2003.

[14] S. Cornejo, A. Guzmán, A. Valencia, J. Rodríguez, and E. Finol. Flow-induced wall mechanics of patient-specific aneurysmal cerebral arteries: Nonlinear isotropic versus anisotropic wall stress. *Proceedings of the Institution of Mechanical Engineers, Part H: Journal of Engineering in Medicine*, 228(1):37–48, 2014.

[15] J. G. JR. van Gijn and G. J. E. Rinkel. Subarachnoid haemorrhage: diagnosis, causes and management. *Brain*, 124(2):249–278, 2001.

[16] J. W. Hop, G. J. E. Rinkel, A. Algra, and J. Van Gijn. Case-fatality rates and functional outcome after subarachnoid hemorrhage: a systematic review. *Stroke*, 28(3):660–664, 1997.

[17] R. Gasparotti and R. Liserre. Intracranial aneurysms. *European Radiology*, 15:441–447, 2005.

[18] M. J. Ali, B. R. Bendok, R. G. Tawk, C. C. Getch, and H. H. Batjer. Trapping and revascularization for a dissecting aneurysm of the proximal posteroinferior cerebellar artery: technical case report and review of the literature. *Neurosurgery*, 51(1):258–263, 2002.

[19] K. Barami and K. Ko. Ruptured mycotic aneurysm presenting as an intraparenchymal hemorrhage and nonadjacent acute subdural hematoma: case report and review of the literature. *Surgical neurology*, 41(4):290–293, 1994.

[20] B. F. Tomandl, N. C. Köstner, M. Schempershofe, W. J. Huk, C. Strauss, L. Anker, and P. Hastreiter. CT angiography of intracranial aneurysms: a focus on postprocessing. *Radiographics*, 24(3):637–655, 2004.

[21] P. M. White, J. M. Wardlaw, and V. Easton. Can noninvasive imaging accurately depict intracranial aneurysms? A systematic review. *Radiology*, 217(2):361–370, 2000.

[22] B. K. Velthuis, M. S. van Leeuwen, T. D. Witkamp, L. M. P. Ramos, J. W. B. van der Sprenkel, and G. J. E. Rinkel. Computerized tomography angiography in patients with

subarachnoid hemorrhage: from aneurysm detection to treatment without conventional angiography. *Journal of Neurosurgery*, 91(5):761–767, 1999.

[23] N. Young, N. W. C. Dorsch, R. J. Kingston, G. Markson, and J. McMahon. Intracranial aneurysms: evaluation in 200 patients with spiral CT angiography. *European Radiology*, 11:123–130, 2001.

[24] Z. Watanabe, Y. Kikuchi, K. Izaki, N. Hanyu, F. S. H. Lim, H. Gotou, J. Koizumi, T. Gotou, M. Kowada, and K. Watanabe. The usefulness of 3D MR angiography in surgery for ruptured cerebral aneurysms. *Surgical Neurology*, 55(6):359–364, 2001.

[25] M. J. H. Wermer, G. J. E. Rinkel, and J. van Gijn. Repeated screening for intracranial aneurysms in familial subarachnoid hemorrhage. *Stroke*, 34(12):2788–2791, 2003.

[26] T. Metens, F. Rio, D. Baleriaux, T. Roger, P. David, and G. Rodesch. Intracranial aneurysms: detection with gadolinium-enhanced dynamic three-dimensional MR angiography—initial results. *Radiology*, 216(1):39–46, 2000.

[27] S. Succi. *The lattice Boltzmann equation: for fluid dynamics and beyond*. Oxford University Press, 2001.

[28] R. Noël, F. Ge, Y. Zhang, L. Navarro, and G. Courbebaisse. Lattice Boltzmann method for modelling of biological phenomena. In *25th European Signal Processing Conference (EUSIPCO)*, pages 2654–2658. IEEE, (2017).

[29] R. Ouared, B. Chopard, B. Stahl, D.A. Rüfenacht, H. Yilmaz, and G. Courbebaisse. Thrombosis modeling in intracranial aneurysms: a lattice Boltzmann numerical algorithm. *Computer Physics Communications*, 179(1-3):128–131, 2008.

[30] S. A. Hosseini, P. Berg, F. Huang, C. Roloff, G. Janiga, and D. Thévenin. Central moments multiple relaxation time LBM for hemodynamic simulations in intracranial aneurysms: An in-vitro validation study using PIV and PC-MRI. *Computers in Biology and Medicine*, 131:104251, 2021.

[31] K. Jain. Efficacy of the FDA nozzle benchmark and the lattice Boltzmann method for the analysis of biomedical flows in transitional regime. *Medical & Biological Engineering & Computing*, 58:1817–1830, 2020.

[32] M. Hasert, K. Masilamani, S. Zimny, H. Klimach, J. Qi, J. Bernsdorf, and S. Roller. Complex fluid simulations with the parallel tree-based Lattice Boltzmann solver Musubi. *Journal of Computational Science*, 5(5):784–794, 2014.

[33] O. Malaspinas, A. Turjman, D. Ribeiro de Sousa, G. Garcia-Cardena, M. Raes, P.-T.T. Nguyen, Y. Zhang, G. Courbebaisse, C. Lelubre, K. Zouaoui Boudjeltia, and B. Chopard. A spatio-temporal model for spontaneous thrombus formation in cerebral aneurysms. *Journal of Theoretical Biology*, 394:68–76, 2016.

[34] J. W. S. McCullough and P. V. Coveney. An efficient, localised approach for the simulation of elastic blood vessels using the lattice Boltzmann method. *Scientific Reports*, 11(1):24260, 2021.

[35] J. W. S. McCullough and P. V. Coveney. High fidelity blood flow in a patient-specific arteriovenous fistula. *Scientific Reports*, 11(1):22301, 2021.

[36] O. E. Kadri, V. D. Chandran, M. Surblyte, and R. S. Voronov. In vivo measurement of blood clot mechanics from computational fluid dynamics based on intravital microscopy images. *Computers in Biology and Medicine*, 106:1–11, 2019.

[37] A. Khosravanian, M. Rahmanimanesh, P. Keshavarzi, and S. Mozaffari. Fast level set method for glioma brain tumor segmentation based on superpixel fuzzy clustering and lattice Boltzmann method. *Computer Methods and Programs in Biomedicine*, 198:105809, 2021.

[38] H. H. Afrouzi, M. Ahmadian, M. Hosseini, H. Arasteh, D. Toghraie, and S. Rostami. Simulation of blood flow in arteries with aneurysm: Lattice Boltzmann Approach (LBM). *Computer Methods and Programs in Biomedicine*, 187:105312, 2020.

[39] U. Frisch, D. d'Humières, B. Hasslacher, P. Lallemand, Y. Pomeau, and J.-P. Rivet. Lattice gas hydrodynamics in two and three dimensions. In *Lattice Gas Methods for Partial Differential Equations*, pages 77–136. CRC Press, 2019.

[40] J. Hardy, Y. Pomeau, and O. De Pazzis. Time evolution of a two-dimensional classical lattice system. *Physical Review Letters*, 31(5):276, 1973.

[41] U. Frisch, B. Hasslacher, and Y. Pomeau. Lattice-gas automata for the Navier-Stokes equation. *Physical Review Letters*, 56(14):1505, 1986.

[42] H. Chen, S. Chen, and W. H. Matthaeus. Recovery of the Navier-Stokes equations using a lattice-gas Boltzmann method. *Physical Review A*, 45(8):R5339, 1992.

[43] L. P. Kadanoff, G. R. McNamara, and G. Zanetti. From automata to fluid flow: Comparisons of simulation and theory. *Physical Review A*, 40(8):4527, 1989.

[44] F. J. Higuera, S. Succi, and R. Benzi. Lattice gas dynamics with enhanced collisions. *EPL (Europhysics Letters)*, 9(4):345, 1989.

[45] X. He and L.-S. Luo. Theory of the lattice Boltzmann method: From the Boltzmann equation to the lattice Boltzmann equation. *Physical Review E*, 56(6):6811, 1997.

[46] P. L. Bhatnagar, E. P. Gross, and M. Krook. A model for collision processes in gases. I. Small amplitude processes in charged and neutral one-component systems. *Physical Review*, 94(3):511, 1954.

[47] X. Shan, X.-F. Yuan, and H. Chen. Kinetic theory representation of hydrodynamics: a way beyond the Navier–Stokes equation. *Journal of Fluid Mechanics*, 550:413–441, 2006.

[48] S. A. Hosseini, C. Coreixas, N. Darabiha, and D. Thévenin. Stability of the lattice kinetic scheme and choice of the free relaxation parameter. *Physical Review E*, 99(6):063305, 2019.

[49] T. Krüger, H. Kusumaatmaja, A. Kuzmin, O. Shardt, G. Silva, and E. M. Viggen. The lattice Boltzmann method. *Springer International Publishing*, 10:978–3, 2017.

[50] N. I. Prasianakis and I. V. Karlin. Lattice Boltzmann method for simulation of compressible flows on standard lattices. *Physical Review E*, 78(1):016704, 2008.

[51] I. Karlin and P. Asinari. Factorization symmetry in the lattice Boltzmann method. *Physica A: Statistical Mechanics and its Applications*, 389(8):1530–1548, 2010.

[52] S. A. Hosseini, N. Darabiha, and D. Thévenin. Compressibility in lattice Boltzmann on standard stencils: effects of deviation from reference temperature. *Philosophical Transactions of the Royal Society A*, 378(2175):20190399, 2020.

[53] S. A. Hosseini. *Development of a lattice Boltzmann-based numerical method for the simulation of reacting flows*. PhD thesis, Université Paris-Saclay & Otto von Guericke University, 2020.

[54] M. H. Saadat, F. Bösch, and I. V. Karlin. Lattice Boltzmann model for compressible flows on standard lattices: Variable Prandtl number and adiabatic exponent. *Physical Review E*, 99(1):013306, 2019.

[55] C. Pan, L. S. Luo, and C. T. Miller. An evaluation of lattice Boltzmann schemes for porous medium flow simulation. *Computers & Fluids*, 35(8-9):898–909, 2006.

[56] S. A. Hosseini, N. Darabiha, and D. Thévenin. Theoretical and numerical analysis of the lattice kinetic scheme for complex flow simulations. *Physical Review E*, 99(2):023305, 2019.

[57] I. Ginzburg, F. Verhaeghe, and D. d'Humieres. Two-relaxation-time lattice Boltzmann scheme: About parametrization, velocity, pressure and mixed boundary conditions. *Communications in Computational Physics*, 3(2):427–478, 2008.

[58] D. d'Humières. Generalized lattice-Boltzmann equations. In B. D. Shizgal and D. P. Weave, editors, *Rarefied Gas Dynamics: Theory and Simulations*, volume 159 of *Progress in Astronautics and Aeronautics*, pages 450–458. AIAA, Washington, D. C, USA, 1992.

[59] P. Lallemand and L.-S. Luo. Theory of the lattice Boltzmann method: Dispersion, dissipation, isotropy, Galilean invariance, and stability. *Physical Review E*, 61(6):6546, 2000.

[60] D. d'Humières. Multiple–relaxation–time lattice Boltzmann models in three dimensions. *Philosophical Transactions of the Royal Society of London. Series A: Mathematical, Physical and Engineering Sciences*, 360(1792):437–451, 2002.

[61] M. Geier, A. Greiner, and J. G. Korvink. Cascaded digital lattice Boltzmann automata for high Reynolds number flow. *Physical Review E*, 73(6):066705, 2006.

[62] J. Latt and B. Chopard. Lattice Boltzmann method with regularized pre-collision distribution functions. *Mathematics and Computers in Simulation*, 72(2-6):165–168, 2006.

[63] S. Ansumali and I. V. Karlin. Single relaxation time model for entropic lattice Boltzmann methods. *Physical Review E*, 65(5):056312, 2002.

[64] I. V. Karlin, F. Bösch, and S. S. Chikatamarla. Gibbs' principle for the lattice-kinetic theory of fluid dynamics. *Physical Review E*, 90(3):031302, 2014.

[65] F. Bösch, S. S. Chikatamarla, and I. V. Karlin. Entropic multirelaxation lattice Boltzmann models for turbulent flows. *Physical Review E*, 92(4):043309, 2015.

[66] P. Lallemand and L.-S. Luo. Theory of the lattice Boltzmann method: Acoustic and thermal properties in two and three dimensions. *Physical Review E*, 68(3):036706, 2003.

[67] P. J. Dellar. Bulk and shear viscosities in lattice Boltzmann equations. *Physical Review E*, 64(3):031203, 2001.

[68] M. Geier. De-aliasing and stabilization formalism of the cascaded lattice Boltzmann automaton for under-resolved high Reynolds number flow. *International Journal for Numerical Methods in Fluids*, 56(8):1249–1254, 2008.

[69] S. A. Hosseini, B. Dorschner, and I. V. Karlin. Towards a consistent lattice Boltzmann model for two-phase fluids. *Journal of Fluid Mechanics*, 953:A4, 2022.

[70] T. Krüger, F. Varnik, and D. Raabe. Shear stress in lattice Boltzmann simulations. *Physical Review E*, 79(4):046704, 2009.

[71] L. Goubergrits, R. Mevert, P. Yevtushenko, J. Schaller, U. Kertzscher, S. Meier, S. Schubert, E. Riesenkampff, and T. Kuehne. The impact of MRI-based inflow for the hemodynamic evaluation of aortic coarctation. *Annals of Biomedical Engineering*, 41:2575–2587, 2013.

[72] A. L. Marsden. Optimization in cardiovascular modeling. *Annual Review of Fluid Mechanics*, 46:519–546, 2014.

[73] R. Balossino, G. Pennati, F. Migliavacca, L. Formaggia, A. Veneziani, M. Tuveri, and G. Dubini. Computational models to predict stenosis growth in carotid arteries: which is the role of boundary conditions? *Computer Methods in Biomechanics and Biomedical Engineering*, 12(1):113–123, 2009.

[74] I. E. Vignon-Clementel, C. A. Figueroa, K. E. Jansen, and C. A. Taylor. Outflow boundary conditions for three-dimensional finite element modeling of blood flow and pressure in arteries. *Computer Methods in Applied Mechanics and Engineering*, 195(29-32):3776–3796, 2006.

[75] Q. Zou and X. He. On pressure and velocity boundary conditions for the lattice Boltzmann BGK model. *Physics of Fluids*, 9(6):1591–1598, 1997.

[76] D. Hardman, S. I. Semple, J. M. J. Richards, and P. R. Hoskins. Comparison of patient-specific inlet boundary conditions in the numerical modelling of blood flow in abdominal aortic aneurysm disease. *International Journal for Numerical Methods in Biomedical Engineering*, 29(2):165–178, 2013.

[77] A. M. Artoli, A. G. Hoekstra, and P. M. A. Sloot. 3D pulsatile flow with the lattice Boltzmann BGK method. *International Journal of Modern Physics C*, 13(08):1119–1134, 2002.

[78] D. P. Ziegler. Boundary conditions for lattice Boltzmann simulations. *Journal of Statistical Physics*, 71:1171–1177, 1993.

[79] S. Chen, D. Martinez, and R. Mei. On boundary conditions in lattice Boltzmann methods. *Physics of Fluids*, 8(9):2527–2536, 1996.

[80] O. Filippova and D. Hänel. Grid refinement for lattice-BGK models. *Journal of Computational Physics*, 147(1):219–228, 1998.

[81] P. Lallemand and L.-S. Luo. Lattice Boltzmann method for moving boundaries. *Journal of Computational Physics*, 184(2):406–421, 2003.

[82] M. Bouzidi, M. Firdaouss, and P. Lallemand. Momentum transfer of a Boltzmann-lattice fluid with boundaries. *Physics of Fluids*, 13(11):3452–3459, 2001.

[83] L. Liang, D. A. Steinman, O. Brina, C. Chnafa, N. M. Cancelliere, and V. M. Pereira. Towards the clinical utility of CFD for assessment of intracranial aneurysm rupture – a systematic review and novel parameter-ranking tool. *Journal of Neurointerventional Surgery*, 11(2):153–158, 2019.

[84] K. M. Saqr, S. Rashad, S. Tupin, K. Niizuma, T. Hassan, T. Tominaga, and M. Ohta. What does computational fluid dynamics tell us about intracranial aneurysms? A meta-analysis and critical review. *Journal of Cerebral Blood Flow & Metabolism*, 40(5):1021–1039, 2020.

[85] H. Meng, V. M. Tutino, J. Xiang, and A. Siddiqui. High WSS or low WSS? complex interactions of hemodynamics with intracranial aneurysm initiation, growth, and rupture: toward a unifying hypothesis. *American Journal of Neuroradiology*, 35(7):1254–1262, 2014.

[86] J. Cebral, E. Ollikainen, B. J. Chung, F. Mut, V. Sippola, B. R. Jahromi, R. Tulamo, J. Hernesniemi, M. Niemelä, A. Robertson, and J. Frösen. Flow conditions in the intracranial aneurysm lumen are associated with inflammation and degenerative changes of the aneurysm wall. *American Journal of Neuroradiology*, 38(1):119–126, 2017.

[87] D. Fiorella, C. Sadasivan, H. H. Woo, and B. Lieber. Regarding "Aneurysm rupture following treatment with flow-diverting stents: computational hemodynamics analysis of treatment". *American Journal of Neuroradiology*, 32(5):E95, 2011.

[88] D. F. Kallmes. Point: CFD–computational fluid dynamics or confounding factor dissemination. *American Journal of Neuroradiology*, 33(3):395–396, 2012.

[89] P. Berg, S. Saalfeld, S. Voß, O. Beuing, and G. Janiga. A review on the reliability of hemodynamic modeling in intracranial aneurysms: why computational fluid dynamics alone cannot solve the equation. *Neurosurgical Focus*, 47(1):E15, 2019.

[90] M. D. Ford, H. N. Nikolov, J. S. Milner, S. P. Lownie, E. M. Demont, W. Kalata, F. Loth, D. W. Holdsworth, and D. A. Steinman. PIV-measured versus CFD-predicted flow dynamics in anatomically realistic cerebral aneurysm models. *Journal of Biomechanical Engineering*, 130(2):021015, 2008.

[91] M. Raschi, F. Mut, G. Byrne, C. M. Putman, S. Tateshima, F. Viñuela, T. Tanoue, K. Tanishita, and J. R. Cebral. CFD and PIV analysis of hemodynamics in a growing intracranial aneurysm. *International Journal for Numerical Methods in Biomedical Engineering*, 28(2):214–228, 2012.

[92] T. Yagi, A. Sato, M. Shinke, S. Takahashi, Y. Tobe, H. Takao, Y. Murayama, and M. Umezu. Experimental insights into flow impingement in cerebral aneurysm by stereoscopic particle image velocimetry: transition from a laminar regime. *Journal of the Royal Society, Interface*, 10(82):20121031, 2013.

[93] P. Bouillot, O. Brina, R. Ouared, K.-O. Lovblad, M. Farhat, and V. M. Pereira. Particle imaging velocimetry evaluation of intracranial stents in sidewall aneurysm: hemodynamic transition related to the stent design. *PloS one*, 9(12):e113762, 2014.

[94] P. Berg, C. Roloff, O. Beuing, S. Voss, S.-I. Sugiyama, N. Aristokleous, A. S. Anayiotos, N. Ashton, A. Revell, N. W. Bressloff, A. G. Brown, B. J. Chung, J. R. Cebral, G. Copelli, W. Fu, A. Qiao, A. J. Geers, S. Hodis, D. Dragomir-Daescu, E. Nordahl, Y. Bora Suzen, M. Owais Khan, K. Valen-Sendstad, K. Kono, P. G. Menon, P. G. Albal, O. Mierka, R. Münster, H. G. Morales, O. Bonnefous, J. Osman, L. Goubergrits, J. Pallares, S. Cito, A. Passalacqua, S. Piskin, K. Pekkan, S. Ramalho, N. Marques, S. Sanchi, K. R. Schumacher, J. Sturgeon, H. Švihlová, J. Hron, G. Usera, M. Mendina, J. Xiang, H. Meng, D. A. Steinman, and G. Janiga. The computational fluid dynamics rupture challenge 2013–phase II: variability of hemodynamic simulations in two intracranial aneurysms. *Journal of Biomechanical Engineering*, 137(12):121008, 2015.

[95] P. Van Ooij, J. J. Schneiders, H. A. Marquering, C. B. Majoie, E. Van Bavel, and A. J. Nederveen. 3-D cine phase-contrast MRI at 3T in intracranial aneurysms compared with patient-specific computational fluid dynamics. *American Journal of Neuroradiology*, 34(9):1785–1791, 2013.

[96] J. R. Cebral, R. S. Pergolizzi Jr, and C. M. Putman. Computational fluid dynamics modeling of intracranial aneurysms:: Qualitative comparison with cerebral angiography. *Academic Radiology*, 14(7):804–813, 2007.

[97] N. Paliwal, R. J. Damiano, N. A. Varble, V. M. Tutino, Z. Dou, A. H. Siddiqui, and H. Meng. Methodology for computational fluid dynamic validation for medical use: application to intracranial aneurysm. *Journal of Biomechanical Engineering*, 139(12), 2017.

[98] M. Müller, S. Schirm, and M. Teschner. Interactive blood simulation for virtual surgery based on smoothed particle hydrodynamics. *Technology and Health Care*, 12(1):25–31, 2004.

[99] J. Qin, W.-M. Pang, B. P. Nguyen, D. Ni, and C.-K. Chui. Particle-based simulation of blood flow and vessel wall interactions in virtual surgery. In *Proceedings of the 2010 Symposium on Information and Communication Technology*, pages 128–133, 2010.

[100] G. Závodszky and G. Paál. Validation of a lattice Boltzmann method implementation for a 3D transient fluid flow in an intracranial aneurysm geometry. *International Journal of Heat and Fluid Flow*, 44:276–283, 2013.

[101] M. D. Mazzeo and P. V. Coveney. Hemelb: A high performance parallel lattice-Boltzmann code for large scale fluid flow in complex geometries. *Computer Physics Communications*, 178(12):894–914, 2008.

[102] D. Groen, J. Hetherington, H. B. Carver, R. W. Nash, M. O. Bernabeu, and P. V. Coveney. Analysing and modelling the performance of the hemelb lattice-Boltzmann simulation environment. *Journal of Computational Science*, 4(5):412–422, 2013.

[103] H. Anzai, M. Ohta, J.-L. Falcone, and B. Chopard. Optimization of flow diverters for cerebral aneurysms. *Journal of Computational Science*, 3(1-2):1–7, 2012.

[104] C. Huang, B. Shi, Z. Guo, and Z. Chai. Multi-GPU based lattice Boltzmann method for hemodynamic simulation in patient-specific cerebral aneurysm. *Communications in Computational Physics*, 17(4):960–974, 2015.

[105] R. Ouared and B. Chopard. Lattice Boltzmann simulations of blood flow: non-Newtonian rheology and clotting processes. *Journal of Statistical Physics*, 121(1):209–221, 2005.

[106] M. Finck, D. Hänel, and I. Wlokas. Simulation of nasal flow by lattice Boltzmann methods. *Computers in Biology and Medicine*, 37(6):739–749, 2007.

[107] Y. Chen, L. Navarro, Y. Wang, and G. Courbebaisse. Segmentation of the thrombus of giant intracranial aneurysms from CT angiography scans with lattice Boltzmann method. *Medical Image Analysis*, 18(1):1–8, 2014.

[108] Y. Ma, R. Mohebbi, M. M. Rashidi, and Z. Yang. Numerical simulation of flow over a square cylinder with upstream and downstream circular bar using lattice Boltzmann method. *International Journal of Modern Physics C*, 29(04):1850030, 2018.

[109] Y. Ma, R. Mohebbi, M. M. Rashidi, Z. Yang, and M. A. Sheremet. Numerical study of mhd nanofluid natural convection in a baffled U-shaped enclosure. *International Journal of Heat and Mass Transfer*, 130:123–134, 2019.

[110] J. Latt, O. Malaspinas, D. Kontaxakis, A. Parmigiani, D. Lagrava, F. Brogi, M. B. Belgacem, Y. Thorimbert, S. Leclaire, S. Li, et al. Palabos: Parallel lattice Boltzmann solver. *Computers & Mathematics with Applications*, 2020.

[111] M. Hasert, K. Masilamani, S. Zimny, H. Klimach, J. Qi, J. Bernsdorf, and S. Roller. Complex fluid simulations with the parallel tree-based lattice Boltzmann solver Musubi. *Journal of Computational Science*, 5(5):784–794, 2014.

[112] T. Suzuki, C. Ioan Nita, S. Rapaka, H. Takao, V. Mihalef, S. Fujimura, C. Dahmani, P. Sharma, H. Mamori, T. Ishibashi, T. Redel, M. Yamamoto, and Y. Murayama. Verification of a research prototype for hemodynamic analysis of cerebral aneurysms. *Conference proceedings : Annual International Conference of the IEEE Engineering in Medicine and Biology Society. IEEE Engineering in Medicine and Biology Society. Annual Conference*, 2016:2921–2924, 2016.

[113] P. Berg, S. Saalfeld, S. Voß, T. Redel, B. Preim, G. Janiga, and O. Beuing. Does the DSA reconstruction kernel affect hemodynamic predictions in intracranial aneurysms? An analysis of geometry and blood flow variations. *Journal of Neurointerventional Surgery*, 10(3):290–296, 2018.

[114] T. Suzuki, H. Takao, S. Rapaka, S. Fujimura, C. Ioan Nita, Y. Uchiyama, H. Ohno, K. Otani, C. Dahmani, V. Mihalef, P. Sharma, A. Mohamed, T. Redel, T. Ishibashi, M. Yamamoto, and Y. Murayama. Rupture risk of small unruptured intracranial aneurysms in Japanese adults. *Stroke*, 51(2):641–643, 2020.

[115] S. A. Hosseini, H. Safari, N. Darabiha, D. Thévenin, and M. Krafczyk. Hybrid lattice Boltzmann-finite difference model for low Mach number combustion simulation. *Combustion and Flame*, 209:394–404, 2019.

[116] P. Berg, D. Stucht, G. Janiga, O. Beuing, O. Speck, and D. Thévenin. Cerebral blood flow in a healthy Circle of Willis and two intracranial aneurysms: computational fluid dynamics versus four-dimensional phase-contrast magnetic resonance imaging. *Journal of Biomechanical Engineering*, 136(4), 2014.

[117] C. Roloff, P. Berg, T. Redel, G. Janiga, and D. Thevenin. Tomographic particle image velocimetry for the validation of hemodynamic simulations in an intracranial aneurysm. In *2017 39th Annual International Conference of the IEEE Engineering in Medicine and Biology Society (EMBC)*, pages 1340–1343. IEEE, 2017.

[118] Y. Murayama, S. Fujimura, T. Suzuki, and H. Takao. Computational fluid dynamics as a risk assessment tool for aneurysm rupture. *Neurosurgical Focus*, 47(1):E12, 2019.

[119] P. Berg, S. Vos, M. Becker, S. Serowy, T. Redel, G. Janiga, M. Skalej, and O. Beuing. Bringing hemodynamic simulations closer to the clinics: a CFD prototype study for intracranial aneurysms. *Conference proceedings: Annual International Conference of the IEEE Engineering in Medicine and Biology Society.*, 2016:3302–3305, 2016.

[120] S. Tupin, K. M. Saqr, and M. Ohta. Effects of wall compliance on multiharmonic pulsatile flow in idealized cerebral aneurysm models: comparative PIV experiments. *Experiments in Fluids*, 61(7):164, 2020.

[121] C. Coreixas, B. Chopard, and J. Latt. Comprehensive comparison of collision models in the lattice Boltzmann framework: Theoretical investigations. *Physical Review E*, 100(3):033305, 2019.

[122] K. M. Saqr, O. Mansour, S. Tupin, T. Hassan, and M. Ohta. Evidence for non-Newtonian behavior of intracranial blood flow from Doppler ultrasonography measurements. *Medical & Biological Engineering & Computing*, 57(5):1029–1036, 2019.

[123] U. Y. Lee, J. Jung, H. S. Kwak, D. H. Lee, G. H. Chung, J. S. Park, and E. J. Koh. Patient-specific computational fluid dynamics in ruptured posterior communicating aneurysms using measured non-Newtonian viscosity: A preliminary study. *Journal of Korean Neurosurgical Society*, 62(2):183–192, 2019.

[124] S. Mahrous, N. A. C. Sidik, and K. M. Saqr. Newtonian and non-Newtonian CFD models of intracranial aneurysm: A review. *CFD Letters*, 12(1):62–86, 2020.

[125] M. O. Khan, D. A. Steinman, and K. Valen-Sendstad. Non-Newtonian versus numerical rheology: Practical impact of shear-thinning on the prediction of stable and unstable flows in intracranial aneurysms. *International Journal for Numerical Methods in Biomedical Engineering*, 33(7), 2017.

[126] M. D. Ford, H. N. Nikolov, J. S. Milner, S. P. Lownie, E. M. DeMont, W. Kalata, F. Loth, D. W. Holdsworth, and D. A. Steinman. PIV-measured versus CFD-predicted flow dynamics in anatomically realistic cerebral aneurysm models. *Journal of Biomechanical Engineering*, 130:21015, 2008.

[127] M. Raschi, F. Mut, G. Byrne, C. M. Putman, S. Tateshima, F. Viñuela, T. Tanoue, K. Tanishita, and J. R. Cebral. CFD and PIV analysis of hemodynamics in a growing intracranial aneurysm. *International Journal for Numerical Methods in Biomedical Engineering*, 28(2):214–228, 2012.

[128] V. L. Rayz, L. Boussel, G. Acevedo-Bolton, A. J. Martin, W. L. Young, M. T. Lawton, R. Higashida, and D. Saloner. Numerical simulations of flow in cerebral aneurysms: comparison of CFD results and in vivo MRI measurements. *Journal of Biomechanical Engineering*, 130:051011, 2008.

[129] A. Arzani, P. Dyverfeldt, T. Ebbers, and S. C. Shadden. In vivo validation of numerical prediction for turbulence intensity in an aortic coarctation. *Annals of Biomedical Engineering*, 40:860–870, 2012.

[130] A. G. Radaelli, L. Augsburger, J. R. Cebral, M. Ohta, D. A. Rüfenacht, R. Balossino, G. Benndorf, D. R. Hose, A. Marzo, R. Metcalfe, et al. Reproducibility of haemodynamical simulations in a subject-specific stented aneurysm model—a report on the Virtual Intracranial Stenting Challenge 2007. *Journal of Biomechanics*, 41(10):2069–2081, 2008.

[131] S. F. C. Stewart, E. G. Paterson, G. W. Burgreen, P. Hariharan, M. Giarra, V. Reddy, S. W. Day, K. B. Manning, S. Deutsch, M. R. Berman, et al. Assessment of CFD performance in simulations of an idealized medical device: results of FDA's first compu-

tational interlaboratory study. *Cardiovascular Engineering and Technology*, 3(2):139–160, 2012.

[132] P. J. Dellar. Incompressible limits of lattice Boltzmann equations using multiple relaxation times. *Journal of Computational Physics*, 190(2):351–370, 2003.

[133] S. Ansumali and I. V. Karlin. Single relaxation time model for entropic lattice Boltzmann methods. *Physical Review E*, 65(5), 2002.

[134] D. d'Humieres, I. Ginzburg, M. Krafczyk, P. Lallemand, and L.-S. Luo. Multiple-relaxation-time lattice Boltzmann models in three dimensions. *Philosophical Transactions of the Royal Society A: Mathematical, Physical and Engineering Sciences*, 360(1792):437–451, 2002.

[135] M. Geier, M. Schönherr, A. Pasquali, and M. Krafczyk. The cumulant lattice Boltzmann equation in three dimensions: Theory and validation. *Computers & Mathematics with Applications*, 70(4):507–547, 2015.

[136] O. Malaspinas. Increasing stability and accuracy of the lattice Boltzmann scheme: Recursivity and regularization. *arXiv preprint arXiv:1505.06900*, 2015.

[137] M. Geier, A. Pasquali, and M. Schönherr. Parametrization of the cumulant lattice Boltzmann method for fourth order accurate diffusion part II: Application to flow around a sphere at drag crisis. *Journal of Computational Physics*, 348:889–898, 2017.

[138] M. Geier, S. Lenz, M. Schönherr, and M. Krafczyk. Under-resolved and large eddy simulations of a decaying Taylor–Green vortex with the cumulant lattice Boltzmann method. *Theoretical and Computational Fluid Dynamics*, 35(2):169–208, 2021.

[139] P. Hariharan, M. Giarra, V. Reddy, S. W. Day, K. B. Manning, S. Deutsch, S. F. C. Stewart, M. R. Myers, M. R. Berman, G. W. Burgreen, et al. Multilaboratory particle image velocimetry analysis of the FDA benchmark nozzle model to support validation of computational fluid dynamics simulations. *Journal of Biomechanical Engineering*, 133(4), 2011.

[140] A. W. Bergersen, M. Mortensen, and K. Valen-Sendstad. The FDA nozzle benchmark: "In theory there is no difference between theory and practice, but in practice there is". *International Journal for Numerical Methods in Biomedical Engineering*, 35(1):e3150, 2019.

[141] V. Chabannes, C. Prud'Homme, M. Szopos, and R. Tarabay. High order finite element simulations for fluid dynamics validated by experimental data from the FDA benchmark nozzle model. *arXiv preprint arXiv:1701.02179*, 2017.

[142] V. Zmijanovic, S. Mendez, V. Moureau, and F. Nicoud. About the numerical robustness of biomedical benchmark cases: Interlaboratory FDA's idealized medical device. *International Journal for Numerical Methods in Biomedical Engineering*, 33(1):e02789, 2017.

[143] G. Janiga. Large eddy simulation of the FDA benchmark nozzle for a Reynolds number of 6500. *Computers in Biology and Medicine*, 47:113–119, 2014.

[144] A. T. White and C. K. Chong. Rotational invariance in the three-dimensional lattice Boltzmann method is dependent on the choice of lattice. *Journal of Computational Physics*, 230(16):6367–6378, 2011.

[145] R. Pewowaruk, Y. Li, D. Rowinski, and A. Roldán-Alzate. Solution adaptive refinement of cut-cell Cartesian meshes can improve FDA nozzle computational fluid dynamics efficiency. *International Journal for Numerical Methods in Biomedical Engineering*, 37(4):e3432, 2021.

[146] S. Bhushan, D. K. Walters, and G. W. Burgreen. Laminar, turbulent, and transitional simulations in benchmark cases with cardiovascular device features. *Cardiovascular Engineering and Technology*, 4(4):408–426, 2013.

[147] E. L. Manchester and X. Y. Xu. The effect of turbulence on transitional flow in the FDA's benchmark nozzle model using large-eddy simulation. *International Journal for Numerical Methods in Biomedical Engineering*, 36(10):e3389, 2020.

[148] Y. T. Delorme, K. Anupindi, and S. H. Frankel. Large eddy simulation of FDA's idealized medical device. *Cardiovascular Engineering and Technology*, 4(4):392–407, 2013.

[149] N. Sánchez Abad, R. Vinuesa, P. Schlatter, M. Andersson, and M. Karlsson. Simulation strategies for the Food and Drug Administration nozzle using Nek5000. *AIP Advances*, 10(2):025033, 2020.

[150] N. Fehn, W. A. Wall, and M. Kronbichler. Modern discontinuous Galerkin methods for the simulation of transitional and turbulent flows in biomedical engineering: a comprehensive LES study of the FDA benchmark nozzle model. *International Journal for Numerical Methods in Biomedical Engineering*, 35(12):e3228, 2019.

[151] S. A. Hosseini, A. Abdelsamie, N. Darabiha, and D. Thévenin. Low-mach hybrid lattice Boltzmann-finite difference solver for combustion in complex flows. *Physics of Fluids*, 32(7):077105, 2020.

[152] Z.-L. Guo, C.-G. Zheng, and B.-C. Shi. Non-equilibrium extrapolation method for velocity and pressure boundary conditions in the lattice Boltzmann method. *Chinese Physics*, 11(4):366, 2002.

[153] H. Yu, S. Engel, G. Janiga, and D. Thévenin. A review of hemolysis prediction models for computational fluid dynamics. *Artificial Organs*, 41:603–621, 2017.

[154] W. R. Mower, W. J. Quiñones, and S. S. Gambhir. Effect of intraluminal thrombus on abdominal aortic aneurysm wall stress. *Journal of Vascular Surgery*, 26(4):602–608, 1997.

[155] Y. Hoi, H. Meng, S. H. Woodward, B. R. Bendok, R. A. Hanel, L. R. Guterman, and L. N. Hopkins. Effects of arterial geometry on aneurysm growth: three-dimensional computational fluid dynamics study. *Journal of Neurosurgery*, 101(4):676–681, 2004.

[156] B. Utter and J. S. Rossmann. Numerical simulation of saccular aneurysm hemodynamics: influence of morphology on rupture risk. *Journal of Biomechanics*, 40(12):2716–2722, 2007.

[157] J. R. Cebral, F. Mut, J. Weir, and C. Putman. Quantitative characterization of the hemodynamic environment in ruptured and unruptured brain aneurysms. *American Journal of Neuroradiology*, 32(1):145–151, 2011.

[158] Y. Miura, F. Ishida, Y. Umeda, H. Tanemura, H. Suzuki, S. Matsushima, S. Shimosaka, and W. Taki. Low wall shear stress is independently associated with the rupture status of middle cerebral artery aneurysms. *Stroke*, 44(2):519–521, 2013.

[159] L. Mountrakis, E. Lorenz, and A. G. Hoekstra. Where do the platelets go? a simulation study of fully resolved blood flow through aneurysmal vessels. *Interface Focus*, 3(2):20120089, 2013.

[160] G. Byrne, F. Mut, and J. Cebral. Quantifying the large-scale hemodynamics of intracranial aneurysms. *American Journal of Neuroradiology*, 35(2):333–338, 2014.

[161] R. Ouared, I. Larrabide, O. Brina, P. Bouillot, G. Erceg, H. Yilmaz, K.-O. Lovblad, and V. M. Pereira. Computational fluid dynamics analysis of flow reduction induced by flow-diverting stents in intracranial aneurysms: a patient-unspecific hemodynamics change perspective. *Journal of NeuroInterventional Surgery*, 8(12):1288–1293, 2016.

[162] S. A. Mahrous, N. A. C. Sidik, and K. M. Saqr. Newtonian and non-Newtonian CFD models of intracranial aneurysm: a review. *CFD Letters*, 12(1):62–86, 2020.

[163] A. Valencia, A. Zarate, M. Galvez, and L. Badilla. Non-Newtonian blood flow dynamics in a right internal carotid artery with a saccular aneurysm. *International Journal for Numerical Methods in Fluids*, 50(6):751–764, 2006.

[164] G. Carty, S. Chatpun, and D. M. Espino. Modeling blood flow through intracranial aneurysms: A comparison of Newtonian and non-Newtonian viscosity. *Journal of Medical and Biological Engineering*, 36(3):396–409, 2016.

[165] M. O. Khan, D. A. Steinman, and K. Valen-Sendstad. Non-Newtonian versus numerical rheology: Practical impact of shear-thinning on the prediction of stable and unstable flows in intracranial aneurysms. *International Journal for Numerical Methods in Biomedical Engineering*, 33(7):e2836, 2017.

[166] A. Arzani. Accounting for residence-time in blood rheology models: do we really need non-Newtonian blood flow modelling in large arteries? *Journal of the Royal Society Interface*, 15(146):20180486, 2018.

[167] J. Chen and X.-Y. Lu. Numerical investigation of the non-Newtonian blood flow in a bifurcation model with a non-planar branch. *Journal of Biomechanics*, 37(12):1899–1911, 2004.

[168] K. Perktold, M. Resch, and H. Florian. Pulsatile non-Newtonian flow characteristics in a three-dimensional human carotid bifurcation model. *Journal of Biomechanical Engineering*, 114(4):464–475, 1991.

[169] K. Fukazawa, F. Ishida, Y. Umeda, Y. Miura, S. Shimosaka, S. Matsushima, W. Taki, and H. Suzuki. Using computational fluid dynamics analysis to characterize local hemodynamic features of middle cerebral artery aneurysm rupture points. *World Neurosurgery*, 83(1):80–86, 2015.

[170] Y. I. Cho and K. R. Kensey. Effects of the non-Newtonian viscosity of blood on flows in a diseased arterial vessel. Part 1: Steady flows. *Biorheology*, 28(3-4):241–262, 1991.

[171] D. A. Steinman, J. S. Milner, C. J. Norley, S. P. Lownie, and D. W. Holdsworth. Image-based computational simulation of flow dynamics in a giant intracranial aneurysm. *American Journal of Neuroradiology*, 24(4):559–566, 2003.

[172] J. R. Cebral, F. Mut, J. Weir, and C. M. Putman. Association of hemodynamic characteristics and cerebral aneurysm rupture. *American Journal of Neuroradiology*, 32(2):264–270, 2011.

[173] D. Wang and J. Bernsdorf. Lattice Boltzmann simulation of steady non-Newtonian blood flow in a 3D generic stenosis case. *Computers & Mathematics with Applications*, 58(5):1030–1034, 2009.

[174] B. M. Hill and C. R. Leonardi. Lattice Boltzmann simulation of transient blood flow in arterial geometries using a regularised, viscoplastic and shear-thinning fluid. *International Journal for Numerical Methods in Biomedical Engineering*, 37(8):e3456, 2021.

[175] E. Aharonov and D. H. Rothman. Non-Newtonian flow (through porous media): A lattice-Boltzmann method. *Geophysical Research Letters*, 20(8):679–682, 1993.

[176] S. Gabbanelli, G. Drazer, and J. Koplik. Lattice Boltzmann method for non-Newtonian (power-law) fluids. *Physical Review E*, 72(4):046312, 2005.

[177] D. Kehrwald. Lattice Boltzmann simulation of shear-thinning fluids. *Journal of Statistical Physics*, 121(1):223–237, 2005.

[178] D. Conrad, A. Schneider, and M. Böhle. Accuracy of non-Newtonian lattice Boltzmann simulations. *Journal of Computational Physics*, 301:218–229, 2015.

[179] J. Boyd, J. Buick, and S. Green. A second-order accurate lattice Boltzmann non-Newtonian flow model. *Journal of Physics A: Mathematical and General*, 39(46):14241, 2006.

[180] E. S. Boek, J. Chin, and P. V. Coveney. Lattice Boltzmann simulation of the flow of non-Newtonian fluids in porous media. *International Journal of Modern Physics B*, 17(01n02):99–102, 2003.

[181] J. Boyd, J. M. Buick, and S. Green. Analysis of the Casson and Carreau-Yasuda non-Newtonian blood models in steady and oscillatory flows using the lattice Boltzmann method. *Physics of Fluids*, 19(9):093103, 2007.

[182] Z. Chen and C. Shu. Simplified lattice Boltzmann method for non-Newtonian power-law fluid flows. *International Journal for Numerical Methods in Fluids*, 92(1):38–54, 2020.

[183] S. Adam and K. N. Premnath. Numerical investigation of the cascaded central moment lattice Boltzmann method for non-Newtonian fluid flows. *Journal of Non-Newtonian Fluid Mechanics*, 274:104188, 2019.

[184] M. Bisht and D. V. Patil. Assessment of multiple relaxation time-lattice Boltzmann method framework for non-Newtonian fluid flow simulations. *European Journal of Mechanics-B/Fluids*, 85:322–334, 2021.

[185] S. A. Hosseini, B. Dorschner, and I. V. Karlin. Entropic multi-relaxation-time lattice Boltzmann model for large density ratio two-phase flows. *arXiv preprint arXiv:2201.12404*, 2022.

[186] J. I. Suarez, R. W. Tarr, and W. R. Selman. Aneurysmal subarachnoid hemorrhage. *New England Journal of Medicine*, 354(4):387–396, 2006.

[187] J. P. Greving, M. J. H. Wermer, R. D. Brown Jr, A. Morita, S. Juvela, M. Yonekura, T. Ishibashi, J. C. Torner, T. Nakayama, G. J. E. Rinkel, et al. Development of the PHASES score for prediction of risk of rupture of intracranial aneurysms: a pooled analysis of six prospective cohort studies. *The Lancet Neurology*, 13(1):59–66, 2014.

[188] K. Jain, S. Roller, and K.-A. Mardal. Transitional flow in intracranial aneurysms–a space and time refinement study below the Kolmogorov scales using lattice Boltzmann method. *Computers & Fluids*, 127:36–46, 2016.

[189] K. Kataoka, M. Taneda, T. Asai, A. Kinoshita, M. Ito, and R. Kuroda. Structural fragility and inflammatory response of ruptured cerebral aneurysms: a comparative study between ruptured and unruptured cerebral aneurysms. *Stroke*, 30(7):1396–1401, 1999.

[190] Ø. Evju, K. Valen-Sendstad, and K.-A. Mardal. A study of wall shear stress in 12 aneurysms with respect to different viscosity models and flow conditions. *Journal of Biomechanics*, 46(16):2802–2808, 2013.

[191] H. Baek, M. V. Jayaraman, and G. E. Karniadakis. Wall shear stress and pressure distribution on aneurysms and infundibulae in the posterior communicating artery bifurcation. *Annals of Biomedical Engineering*, 37:2469–2487, 2009.

[192] Y. Kurokawa, S. Abiko, and K. Watanabe. Noninvasive detection of intracranial vascular lesions by recording blood flow sounds. *Stroke*, 25(2):397–402, 1994.

[193] H. J. Steiger and H.-J. Reulen. Low frequency flow fluctuations in saccular aneurysms. *Acta Neurochirurgica*, 83(3):131–137, 1986.

[194] G. G. Ferguson. Turbulence in human intracranial saccular aneurysms. *Journal of Neurosurgery*, 33(5):485–497, 1970.

[195] T. E. Simkins, W. E. Stehbens, and D. Phil. Vibrations recorded from the adventitial surface of experimental aneurysms and arteriovenous fistulas. *Vascular Surgery*, 8(3), 1974.

[196] H. J. Steiger, A. Poll, D. Liepsch, and H.-J. Reulen. Basic flow structure in saccular aneurysms: a flow visualization study. *Heart and Vessels*, 3(2):55–65, 1987.

[197] L. N. Sekhar and J. F. Wasserman. Noninvasive detection of intracranial vascular lesions using an electronic stethoscope. *Journal of Neurosurgery*, 60(3):553–559, 1984.

[198] L. N. Sekhar, M. Sun, D. Bonaddio, and R. J. Sclabassi. Acoustic recordings from experimental saccular aneurysms in dogs. *Stroke*, 21(8):1215–1221, 1990.

[199] L. Antiga and D. A. Steinman. Rethinking turbulence in blood. *Biorheology*, 46(2):77–81, 2009.

[200] K. Jain. The effect of varying degrees of stenosis on transition to turbulence in oscillatory flows. *Biomechanics and Modeling in Mechanobiology*, 21(3):1029–1041, 2022.

[201] A. G. Straatman, R. E. Khayat, E. Haj-Qasem, and D. A. Steinman. On the hydrodynamic stability of pulsatile flow in a plane channel. *Physics of Fluids*, 14(6):1938–1944, 2002.

[202] H. M. Blackburn and S. J. Sherwin. Instability modes and transition of pulsatile stenotic flow: pulse-period dependence. *Journal of Fluid Mechanics*, 573:57–88, 2007.

[203] S. Einav and M. Sokolov. An experimental study of pulsatile pipe flow in the transition range. *Journal of Biomechanical Engineering*, 115:404–411, 1993.

[204] A. Balasso, M. Fritzsche, D. Liepsch, S. Prothmann, J. S. Kirschke, S. Sindeev, S. Frolov, and B. Friedrich. High-frequency wall vibrations in a cerebral patient-specific aneurysm model. *Biomedical Engineering/Biomedizinische Technik*, 64(3):275–284, 2019.

[205] K. Valen-Sendstad, K.-A. Mardal, and D. A. Steinman. High-resolution CFD detects high-frequency velocity fluctuations in bifurcation, but not sidewall, aneurysms. *Journal of Biomechanics*, 46(2):402–407, 2013.

[206] J. Xiang, S. K. Natarajan, M. Tremmel, D. Ma, J. Mocco, L. N. Hopkins, A. H. Siddiqui, E. I. Levy, and H. Meng. Hemodynamic-morphologic discriminants for intracranial aneurysm rupture. *Stroke*, 42(1):144–152, 2011.

[207] L. Xu, F. Liang, L. Gu, and H. Liu. Flow instability detected in ruptured versus unruptured cerebral aneurysms at the internal carotid artery. *Journal of Biomechanics*, 72:187–199, 2018.

[208] M. O. Khan, V. Toro Arana, M. Najafi, D. E. MacDonald, T. Natarajan, K. Valen-Sendstad, and D. A. Steinman. On the prevalence of flow instabilities from high-fidelity computational fluid dynamics of intracranial bifurcation aneurysms. *Journal of Biomechanics*, 127:110683, 2021.

[209] K. Valen-Sendstad, M. Piccinelli, and D. A. Steinman. High-resolution computational fluid dynamics detects flow instabilities in the carotid siphon: implications for aneurysm initiation and rupture? *Journal of Biomechanics*, 47(12):3210–3216, 2014.

[210] H. Baek, M. V. Jayaraman, P. D. Richardson, and G. E. Karniadakis. Flow instability and wall shear stress variation in intracranial aneurysms. *Journal of the Royal Society Interface*, 7(47):967–988, 2010.

[211] M. D. Ford and U. Piomelli. Exploring high frequency temporal fluctuations in the terminal aneurysm of the basilar bifurcation. *Journal of Biomechanical Engineering*, 134(10):091003, 2012.

[212] K. Valen-Sendstad, K.-A. Mardal, M. Mortensen, B. A. P. Reif, and H. P. Langtangen. Direct numerical simulation of transitional flow in a patient-specific intracranial aneurysm. *Journal of Biomechanics*, 44(16):2826–2832, 2011.

[213] K. Valen-Sendstad and D. A. Steinman. Mind the gap: impact of computational fluid dynamics solution strategy on prediction of intracranial aneurysm hemodynamics and rupture status indicators. *American Journal of Neuroradiology*, 35(3):536–543, 2014.

[214] M. O. Khan, K. Valen-Sendstad, and D. A. Steinman. Narrowing the expertise gap for predicting intracranial aneurysm hemodynamics: impact of solver numerics versus mesh and time-step resolution. *American Journal of Neuroradiology*, 36(7):1310–1316, 2015.

[215] B. Chung and J. R. Cebral. CFD for evaluation and treatment planning of aneurysms: review of proposed clinical uses and their challenges. *Annals of Biomedical Engineering*, 43:122–138, 2015.

[216] S. Voß, O. Beuing, G. Janiga, and P. Berg. Multiple aneurysms anatomy challenge 2018 (MATCH)—Phase Ib: Effect of morphology on hemodynamics. *PloS One*, 14(5):e0216813, 2019.

[217] G. Janiga, P. Berg, S. Sugiyama, K. Kono, and D. A. Steinman. The Computational Fluid Dynamics Rupture Challenge 2013—Phase I: prediction of rupture status in intracranial aneurysms. *American Journal of Neuroradiology*, 36(3):530–536, 2015.

[218] D. W. Ricker. *Echo signal processing*. Springer Science & Business Media, 2003.

[219] A. Abdelsamie, G. Janiga, and D. Thevenin. Spectral entropy as a flow state indicator. *International Journal of Heat and Fluid Flow*, 68:102–113, 2017.

[220] F. Huang, R. Noël, P. Berg, and S. A. Hosseini. Simulation of the FDA nozzle benchmark: A lattice Boltzmann study. *Computer Methods and Programs in Biomedicine*, 221:106863, 2022.

[221] T. B. Le. Dynamic modes of inflow jet in brain aneurysms. *Journal of Biomechanics*, 116:110238, 2021.

[222] L. H'ector Ju'arez and E. Ramos. Direct numerical simulation of transition to turbulence in an oscillatory channel flow. *Comptes Rendus Mecanique*, 331(1):55–60, 2003.

[223] L. Xu, L. Gu, and H. Liu. Exploring potential association between flow instability and rupture in patients with matched-pairs of ruptured–unruptured intracranial aneurysms. *Biomedical Engineering Online*, 15(2):461–477, 2016.

[224] D. M. Sforza, K. Kono, S. Tateshima, F. Viñuela, C. Putman, and J. R. Cebral. Hemodynamics in growing and stable cerebral aneurysms. *Journal of Neurointerventional Surgery*, 8(4):407–412, 2016.

[225] G. Janiga. Quantitative assessment of 4D hemodynamics in cerebral aneurysms using proper orthogonal decomposition. *Journal of Biomechanics*, 82:80–86, 2019.

[226] S. A. Hosseini, F. Huang, and D. Thévenin. Lattice Boltzmann model for simulation of flow in intracranial aneurysms considering non-Newtonian effects. *Physics of Fluids*, 34(7):073105, 2022.

[227] N. Varble, J. Xiang, N. Lin, E. Levy, and H. Meng. Flow instability detected by high-resolution computational fluid dynamics in fifty-six middle cerebral artery aneurysms. *Journal of Biomechanical Engineering*, 138(6), 2016.

[228] D. Behme, S. Voß, J. Korte, M. Thormann, A. Mpotsaris, S. Saalfeld, G. Janiga, and P. Berg. Discrimination between stable and unstable intracranial aneurysms using image-based blood flow simulations. *Journal of NeuroInterventional Surgery*, 13(Suppl 1):A101–A101, 2021.

[229] F. Gaidzik, M. Pravdivtseva, N. Larsen, O. Jansen, J.-B. Hövener, and P. Berg. Luminal enhancement in intracranial aneurysms: fact or feature?—A quantitative multimodal flow analysis. *International Journal of Computer Assisted Radiology and Surgery*, 16:1999–2008, 2021.

[230] S. Voß, S. Saalfeld, T. Hoffmann, O. Beuing, G. Janiga, and P. Berg. Fluid-structure interaction in intracranial vessel walls: the role of patient-specific wall thickness. *Current Directions in Biomedical Engineering*, 4(1):587–590, 2018.

[231] S. Voß, S. Glaßer, T. Hoffmann, O. Beuing, S. Weigand, K. Jachau, B. Preim, D. Thévenin, G. Janiga, and P. Berg. Fluid-structure simulations of a ruptured intracranial aneurysm: constant versus patient-specific wall thickness. *Computational and Mathematical Methods in Medicine*, 2016, 2016.

[232] P. Berg, S. Saalfeld, S. Voß, O. Beuing, and G. Janiga. A review on the reliability of hemodynamic modeling in intracranial aneurysms: why computational fluid dynamics alone cannot solve the equation. *Neurosurgical Focus*, 47(1):E15, 2019.

[233] P. Berg, S. Voß, G. Janiga, S. Saalfeld, A. W. Bergersen, K. Valen-Sendstad, J. Bruening, L. Goubergrits, A. Spuler, T. L. Chiu, et al. Multiple Aneurysms Anatomy Challenge 2018 (MATCH)—phase II: rupture risk assessment. *International Journal of Computer Assisted Radiology and Surgery*, 14:1795–1804, 2019.

[234] S. Zimny. *Hemodynamic Flow Simulation in Patient Specific Cerebral Aneurysms*. Verlag Dr. Hut, 2016.

[235] T. Skorczewski, L. C. Erickson, and A. L. Fogelson. Platelet motion near a vessel wall or thrombus surface in two-dimensional whole blood simulations. *Biophysical Journal*, 104(8):1764–1772, 2013.

[236] M. N. Ngoepe and Y. Ventikos. Computational modelling of clot development in patient-specific cerebral aneurysm cases. *Journal of Thrombosis and Haemostasis*, 14(2):262–272, 2016.

[237] V. Govindarajan, V. Rakesh, J. Reifman, and A. Y. Mitrophanov. Computational study of thrombus formation and clotting factor effects under venous flow conditions. *Biophysical Journal*, 110(8):1869–1885, 2016.

[238] D. A. Wolf-Gladrow. *Lattice-gas cellular automata and lattice Boltzmann models: an introduction*. Springer, 2004.

Appendix A

Discrete velocity sets

In order to obtain accurate solutions to the Boltzmann equations, it is crucial to have an appropriate discrete velocity set $\{\mathbf{c}_\alpha\}$ that is sufficiently well-resolved. However, it is also important to consider the numerical cost of the algorithm, which increases with the number of discrete velocities used. Therefore, finding a velocity set with a minimal number of discrete velocities while still capturing the desired physics is an important task. The detailed discussion can be found in the book by Wolf-Gladrow [238].
The discrete velocity set is commonly expressed by its number d of spatial dimensions and the number q of discrete velocities using the notation DdQq in the LBM terminology. The so-called stencil has to obey rotational symmetry and keeps the conservation of mass and momentum. The most popular sets for 2D are D2Q5 and D2Q9 while it is D3Q15, D3Q19 and D3Q27 in 3D computations.
The discrete velocities ($\boldsymbol{c_\alpha}$) and corresponding weights of those velocities (w_α) are summarized below in 2D and 3D simulations with different types of stencils.

A.1 2-D stencils

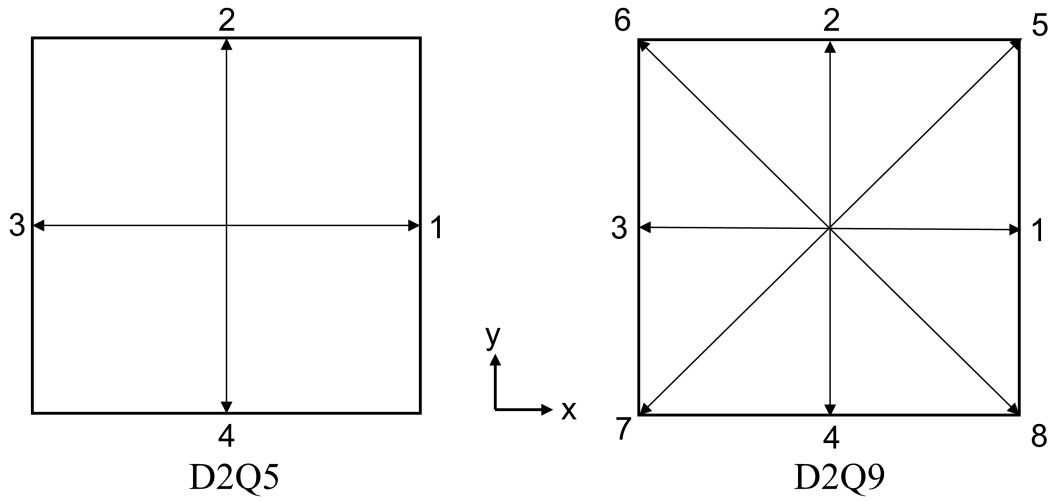

Figure A.1: D2Q5 and D2Q9 velocity sets commonly used in the 2D simulations.

- D2Q5 stencil

$$\boldsymbol{c_\alpha} = \begin{pmatrix} 0 & 1 & 0 & -1 & 0 \\ 0 & 0 & 1 & 0 & -1 \end{pmatrix} \tag{A.1}$$

$$w_\alpha = \begin{pmatrix} \frac{1}{3} & \frac{1}{6} & \frac{1}{6} & \frac{1}{6} & \frac{1}{6} \end{pmatrix} \tag{A.2}$$

  where $\alpha = 0, \ldots, 4$

- D2Q9 stencil

$$\boldsymbol{c_\alpha} = \begin{pmatrix} 0 & 1 & 0 & -1 & 0 & 1 & -1 & -1 & 1 \\ 0 & 0 & 1 & 0 & -1 & 1 & 1 & -1 & -1 \end{pmatrix} \tag{A.3}$$

$$w_\alpha = \begin{pmatrix} \frac{4}{9} & \frac{1}{9} & \frac{1}{9} & \frac{1}{9} & \frac{1}{9} & \frac{1}{36} & \frac{1}{36} & \frac{1}{36} & \frac{1}{36} \end{pmatrix} \tag{A.4}$$

  where $\alpha = 0, \ldots, 8$

A.2 3-D stencils

- D3Q15 stencil

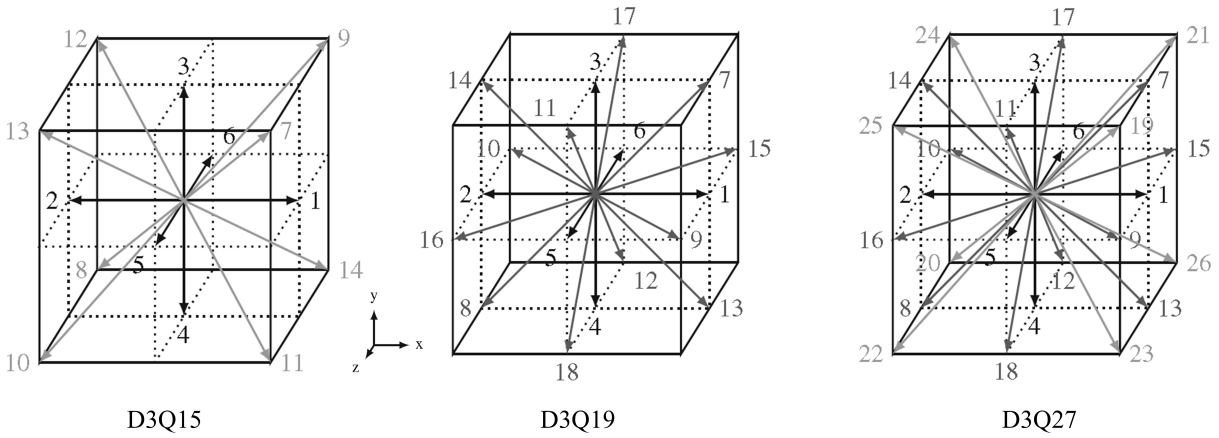

Figure A.2: The schematic of discrete velocity sets for D3Q15, D3Q19, D3Q27 commonly used in the 3D simulations.

$$\boldsymbol{c_\alpha} = \begin{pmatrix} 0 & 1 & -1 & 0 & 0 & 0 & 0 & 1 & -1 & 1 & -1 & 1 & -1 & -1 & 1 \\ 0 & 0 & 0 & 1 & -1 & 0 & 0 & 1 & -1 & 1 & -1 & -1 & 1 & 1 & -1 \\ 0 & 0 & 0 & 0 & 0 & 1 & -1 & 1 & -1 & -1 & 1 & 1 & -1 & 1 & -1 \end{pmatrix} \tag{A.5}$$

$$w_\alpha = \begin{pmatrix} \frac{2}{9} & \frac{1}{9} & \frac{1}{9} & \frac{1}{9} & \frac{1}{9} & \frac{1}{9} & \frac{1}{9} & \frac{1}{72} & \frac{1}{72} & \frac{1}{72} & \frac{1}{72} & \frac{1}{72} & \frac{1}{72} & \frac{1}{72} & \frac{1}{72} \end{pmatrix} \tag{A.6}$$

where $\alpha = 0, \ldots, 14$

- D3Q19 stencil

$$\boldsymbol{c_\alpha} = \begin{pmatrix} 0 & 1 & -1 & 0 & 0 & 0 & 0 & 1 & -1 & 1 & -1 & 0 & 0 & 1 & -1 & 1 & -1 & 0 & 0 \\ 0 & 0 & 0 & 1 & -1 & 0 & 0 & 1 & -1 & 0 & 0 & 1 & -1 & -1 & 1 & 0 & 0 & 1 & -1 \\ 0 & 0 & 0 & 0 & 0 & 1 & -1 & 0 & 0 & 1 & -1 & 1 & -1 & 0 & 0 & -1 & 1 & -1 & 1 \end{pmatrix} \tag{A.7}$$

$$w_\alpha = \begin{pmatrix} \frac{1}{3} & \frac{1}{18} & \frac{1}{18} & \frac{1}{18} & \frac{1}{18} & \frac{1}{18} & \frac{1}{18} & \frac{1}{36} & \frac{1}{36} & \frac{1}{36} & \frac{1}{36} & \frac{1}{36} & \frac{1}{36} & \frac{1}{36} & \frac{1}{36} & \frac{1}{36} & \frac{1}{36} & \frac{1}{36} & \frac{1}{36} \end{pmatrix} \tag{A.8}$$

where $\alpha = 0, \ldots, 18$

- D3Q27 stencil

$$\boldsymbol{c_\alpha} = \begin{pmatrix} 0 & 1 & -1 & 0 & 0 & 0 & 0 & 1 & -1 & 1 & -1 & 0 & 0 & 1 & -1 & 1 & -1 & 0 & 0 & 1 & -1 & 1 & -1 & 1 & -1 & -1 & 1 \\ 0 & 0 & 0 & 1 & -1 & 0 & 0 & 1 & -1 & 0 & 0 & 1 & -1 & -1 & 1 & 0 & 0 & 1 & -1 & 1 & -1 & 1 & -1 & -1 & 1 & 1 & -1 \\ 0 & 0 & 0 & 0 & 0 & 1 & -1 & 0 & 0 & 1 & -1 & 1 & -1 & 0 & 0 & -1 & 1 & -1 & 1 & 1 & -1 & -1 & 1 & 1 & -1 & 1 & -1 \end{pmatrix} \tag{A.9}$$

$$w_\alpha = \left(\tfrac{8}{27} \;\; \tfrac{2}{27} \;\; \tfrac{2}{27} \;\; \tfrac{2}{27} \;\; \tfrac{2}{27} \;\; \tfrac{2}{27} \;\; \tfrac{2}{27} \;\; \tfrac{1}{54} \;\; \tfrac{1}{54} \;\; \tfrac{1}{54} \;\; \tfrac{1}{54} \;\; \tfrac{1}{54} \;\; \tfrac{1}{54} \;\; \tfrac{1}{54} \;\; \tfrac{1}{54} \;\; \tfrac{1}{54} \;\; \tfrac{1}{54} \;\; \tfrac{1}{54} \;\; \tfrac{1}{54} \;\; \tfrac{1}{216} \;\; \tfrac{1}{216} \;\; \tfrac{1}{216} \;\; \tfrac{1}{216} \;\; \tfrac{1}{216} \;\; \tfrac{1}{216} \;\; \tfrac{1}{216} \;\; \tfrac{1}{216} \;\; \tfrac{1}{216}\right) \tag{A.10}$$

where $\alpha = 0, \ldots, 26$

Appendix B

MRT: Transformation matrices involving Hermite polynomials

We will focus on smaller stencils here for simplicity (D2Q9 and D3Q7 stencils). To compute the transformation matrices for both stencils, we need to determine the relationships between the moments in velocity space and the discrete velocity vectors. These transform matrices allow us to express the moments in terms of the discrete velocities, simplifying the computation of the collision and streaming steps. However, it is important to note that transforms for higher-order stencils and different moment spaces can be readily computed using the discrete velocity vectors and chosen sets of moments.

B.1 D2Q9 stencil

For the D2Q9 stencil, the transformation matrix $\boldsymbol{M}$ consisting of nine 2-D Hermite polynomials and its inverse $\boldsymbol{M^{-1}}$ are given as:

$$\boldsymbol{M} = \begin{pmatrix} \boldsymbol{H_0} \\ \boldsymbol{H_x} \\ \boldsymbol{H_y} \\ \boldsymbol{H_{xy}} \\ \boldsymbol{H_{x^2}} \\ \boldsymbol{H_{y^2}} \\ \boldsymbol{H_{x^2y}} \\ \boldsymbol{H_{xy^2}} \\ \boldsymbol{H_{x^2y^2}} \end{pmatrix} = \begin{pmatrix} 1 & 1 & 1 & 1 & 1 & 1 & 1 & 1 & 1 \\ 0 & 1 & 0 & -1 & 0 & 1 & -1 & -1 & 1 \\ 0 & 0 & 0 & 0 & 0 & 1 & -1 & 1 & -1 \\ 0 & 0 & 0 & 0 & 0 & 1 & -1 & 1 & -1 \\ -c_s^2 & 1-c_s^2 & -c_s^2 & 1-c_s^2 & -c_s^2 & 1-c_s^2 & 1-c_s^2 & 1-c_s^2 & 1-c_s^2 \\ -c_s^2 & -c_s^2 & 1-c_s^2 & -c_s^2 & 1-c_s^2 & 1-c_s^2 & 1-c_s^2 & 1-c_s^2 & 1-c_s^2 \\ 0 & 0 & -c_s^2 & 0 & c_s^2 & 1-c_s^2 & 1-c_s^2 & c_s^2-1 & c_s^2-1 \\ 0 & -c_s^2 & 0 & c_s^2 & 0 & 1-c_s^2 & c_s^2-1 & c_s^2-1 & 1-c_s^2 \\ c_s^4 & c_s^2(c_s^2-1) & c_s^2(c_s^2-1) & c_s^2(c_s^2-1) & c_s^2(c_s^2-1) & (c_s^2-1)^2 & (c_s^2-1)^2 & (c_s^2-1)^2 & (c_s^2-1)^2 \end{pmatrix} \tag{B.1}$$

$$\boldsymbol{M^{-1}} = \begin{pmatrix} (c_s^2-1)^2 & 0 & 0 & 0 & c_s^2-1 & c_s^2-1 & 0 & 0 & 1 \\ -\frac{c_s^2(c_s^2-1)}{2} & \frac{1-c_s^2}{2} & 0 & 0 & \frac{1-c_s^2}{2} & -\frac{c_s^2}{2} & 0 & -\frac{1}{2} & \frac{1}{2} \\ -\frac{c_s^2(c_s^2-1)}{2} & 0 & \frac{1-c_s^2}{2} & 0 & -\frac{c_s^2}{2} & \frac{1-c_s^2}{2} & -\frac{1}{2} & 0 & -\frac{1}{2} \\ -\frac{c_s^2(c_s^2-1)}{2} & \frac{c_s^2-1}{2} & 0 & 0 & \frac{1-c_s^2}{2} & -\frac{c_s^2}{2} & 0 & \frac{1}{2} & -\frac{1}{2} \\ -\frac{c_s^2(c_s^2-1)}{2} & 0 & \frac{c_s^2-1}{2} & 0 & -\frac{c_s^2}{2} & \frac{1-c_s^2}{2} & \frac{1}{2} & 0 & -\frac{1}{2} \\ \frac{c_s^4}{4} & \frac{c_s^4}{4} & \frac{c_s^4}{4} & \frac{1}{4} & \frac{c_s^4}{4} & \frac{c_s^4}{4} & \frac{1}{4} & \frac{1}{4} & \frac{1}{4} \\ \frac{c_s^4}{4} & -\frac{c_s^4}{4} & \frac{c_s^4}{4} & -\frac{1}{4} & \frac{c_s^4}{4} & \frac{c_s^4}{4} & \frac{1}{4} & -\frac{1}{4} & \frac{1}{4} \\ \frac{c_s^4}{4} & -\frac{c_s^4}{4} & -\frac{c_s^4}{4} & \frac{1}{4} & \frac{c_s^4}{4} & \frac{c_s^4}{4} & -\frac{1}{4} & -\frac{1}{4} & \frac{1}{4} \\ \frac{c_s^4}{4} & \frac{c_s^4}{4} & -\frac{c_s^4}{4} & -\frac{1}{4} & \frac{c_s^4}{4} & \frac{c_s^4}{4} & -\frac{1}{4} & \frac{1}{4} & \frac{1}{4} \end{pmatrix} \tag{B.2}$$

B.2 D3Q7 stencil

For this D3Q7 stencil, the transformation matrix is composed of seven Hermite polynomials, resulting in the following matrix:

$$\boldsymbol{M} = \begin{pmatrix} \boldsymbol{H_0} \\ \boldsymbol{H_x} \\ \boldsymbol{H_y} \\ \boldsymbol{H_z} \\ \boldsymbol{H_{x^2}} \\ \boldsymbol{H_{y^2}} \\ \boldsymbol{H_{z^2}} \end{pmatrix} = \begin{pmatrix} 1 & 1 & 1 & 1 & 1 & 1 & 1 \\ 0 & 1 & -1 & 0 & 0 & 0 & 0 \\ 0 & 0 & 0 & 0 & 0 & 1 & -1 \\ 0 & 0 & 0 & 0 & 0 & 1 & -1 \\ -c_s^2 & 1-c_s^2 & 1-c_s^2 & -c_s^2 & -c_s^2 & -c_s^2 & -c_s^2 \\ -c_s^2 & -c_s^2 & -c_s^2 & 1-c_s^2 & 1-c_s^2 & -c_s^2 & -c_s^2 \\ -c_s^2 & -c_s^2 & -c_s^2 & -c_s^2 & -c_s^2 & 1-c_s^2 & 1-c_s^2 \end{pmatrix} \tag{B.3}$$

$$\boldsymbol{M^{-1}} = \begin{pmatrix} 1-3c_s^2 & 0 & 0 & 0 & -1 & -1 & -1 \\ \frac{c_s^2}{2} & \frac{1}{2} & 0 & 0 & \frac{1}{2} & 0 & 0 \\ \frac{c_s^2}{2} & -\frac{1}{2} & 0 & 0 & \frac{1}{2} & 0 & 0 \\ \frac{c_s^2}{2} & 0 & \frac{1}{2} & 0 & 0 & \frac{1}{2} & 0 \\ \frac{c_s^2}{2} & 0 & -\frac{1}{2} & 0 & 0 & \frac{1}{2} & 0 \\ \frac{c_s^2}{2} & 0 & 0 & \frac{1}{2} & 0 & 0 & \frac{1}{2} \\ \frac{c_s^2}{2} & 0 & 0 & -\frac{1}{2} & 0 & 0 & \frac{1}{2} \end{pmatrix} \tag{B.4}$$

Appendix C

Journal publications of the candidate

- **Feng Huang**, Romain Noël, Philipp Berg, and Seyed Ali Hosseini. Simulation of the FDA nozzle benchmark: A lattice Boltzmann study. Computer Methods and Programs in Biomedicine, 221:106863, 2022.
- Seyed Ali Hosseini, **Feng Huang**, Dominique Thévenin. Lattice Boltzmann model for simulation of flow in intracranial aneurysms considering non-newtonian effects. Physics of Fluids, 34(7):073105, 2022.
- Seyed Ali Hosseini, Philipp Berg, **Feng Huang**, Christoph Roloff, Gábor Janiga, and Dominique Thévenin. Central moments multiple relaxation time LBM for hemodynamic simulations in intracranial aneurysms: an in-vitro validation study using PIV and PC-MRI. Computers in Biology and Medicine, 131:104251, 2021.